Università degli Studi di Firenze

Facoltà di Ingegneria - Dipartimento di Ingegneria Industriale

Thesis submitted in fulfillment of the requirements for the award of the degree of:

Doctor of Philosophy in

Energy Engineering and Innovative Industrial and Environmental Technologies

PhD School in Industrial Engineering - XXVI Cycle (2011-2013)

ING-IND/09

Characterization of vaneless diffuser rotating stall on centrifugal compressors for industrial applications

Tutor

Eng. Giovanni Ferrara

Candidate

Eng. Davide Biliotti

Industrial Tutor

Eng. Libero Tapinassi, *GE Oil & Gas.*

PhD Course Coordinator

Prof. Eng. Maurizio De Lucia

Florence, Italy, December 2013

To my family.

To my grandmother Carla.

To Valeria with all my love.

Declaration

I hereby declare that this submission is my own work and, to the best of my knowledge and belief, it contains no material previously published or written by another person, nor material which to a substantial extent has been accepted for the award of any other degree or diploma at University of Florence or any other educational institution, except where due references are provided in the thesis itself.

Furthermore, all data here reported are intellectual property of *GE Oil & Gas* – Nuovo Pignone and cannot be divulged to third parties.

Any contribution made to the research by others, with whom I have been working, is explicitly acknowledged in the thesis.

_____

Davide Biliotti

December 2013

Acknowledgements

It is a great pleasure to thank all the people who have supported me during these long three years.

First of all, I would like to thank Prof. Giovanni Ferrara with all my gratitude mostly for being a mentor, a friend and for giving me the possibility to grow up both from a human and a professional point of views.

Sincere thanks are due to Prof. Ennio Antonio Carnevale for giving the possibility to the entire group to be involved in many academic activities.

There are no words to explain what represented Eng. Lorenzo Ferrari throughout my PhD course. Not only for his incredible competence but also for his encouragement and his availability in giving me a “pat on the back” every moment I needed. Thank you my friend.

Special thanks also to the industrial partner of my research work for giving me the privilege to work in a prestigious company for first and then the opportunity to be part of them as a colleague. In particular, I would like to thank Eng. Libero Tapinassi for his priceless support during the entire activity and the whole Aero Team.

It is not possible to evaluate the contribute of my university colleagues who have become friends during these three years: Francesco Balduzzi, Giovanni Vichi, Alessandro Bianchini, Luca Romani, Isacco Stiaccini, Fabio Esposito, Riccardo Maleci, Fabio Tarani, Giulio Lenzi and Sandro Magnani. Thank you guys. I did not know how to do without you.

I wish to thank also the Friends of a lifetime for being always at my side and for providing me help whenever I needed. Thank you Juri, Virginia, Lavinia, Fabio, Lorenzo T., Niccolò, Duccio, Lorenzo B. and Beatrice.

I would like to thank my grandmother Carla for having seen the Engineer who was in me when I was only five. Thank you, you will be always in my heart.

Thanks to all my family and in particular to my mother and my father for giving me love every day of all my life and for giving me the possibility to follow my dreams. You will be always an example for me. Thanks to My “little” brother Damiano for being the playmate of my growth. Hope you’ll find your way. I’ll be always at your side.

Lastly, my greatest thanks are due to Valeria with all my love for being the engine and the power of every day of my life.

Davide

Publications

The papers listed below were published or submitted for publication during the candidature.

1. Bianchini, A., **Biliotti, D.**, Ferrara, G., Ferrari, L., Belardini, E., Giachi, M., Tapinassi, L. and Vannini, G., 2013, "A systematic approach to estimate the impact of the aerodynamic force induced by rotating stall in a vaneless diffuser on the rotordynamic behavior of centrifugal compressors," *Journal of Engineering for Gas Turbines and Power*, 135(11), pp. 1-9.

2. Bianchini, A., **Biliotti, D.**, Ferrara, G., Ferrari, L., Belardini, E., Giachi, M. and Tapinassi, L., 2014, "Some guidelines for the experimental characterization of vaneless diffuser rotating stall in stages of industrial centrifugal compressors," Paper published in *Proc. of the ASME Turbo Expo 2014, Düsseldorf, Germany*, June 16-20, 2014.

3. **Biliotti, D.**, Bianchini, A., Ferrara, G., Ferrari, L., Belardini, E., Giachi, M., Tapinassi, L. and Vannini, G., 2014, "Analysis of the rotordynamic response of a centrifugal compressor subject to aerodynamic loads due to rotating stall," Paper published in *Proc. of the ASME Turbo Expo 2014, Düsseldorf, Germany*, June 16-20, 2014, and recommended for Journal publication.

Other publications:

4. Ferrara, G., Ferrari, L., Vichi, G., Lenzi, G., **Biliotti, D.**, "Acoustic characterization of automotive mufflers. Part I: test rig design and evaluation of acoustic properties," SAE Technical Paper 12AC-0073, presented at SAE World Congress & Exhibition, USA, 2012.

5. Ferrara, G., Ferrari, L., Vichi, G., Lenzi, G., **Biliotti, D.**, "Acoustic characterization of automotive mufflers. Part II: validation of the numerical models by means of experimental data," *SAE Technical Paper 12AC-0074, presented at SAE World Congress & Exhibition, USA,* 2012.

Summary

List of Figures

List of Tables

List of symbols and abbreviations

1xREV		Rotational frequency
A		Generic Area
a	$=\sqrt{kRT}$	Speed of sound
A_{limit}		Maximum Allowable Total Vibration
b		Width
c		Absolute velocity
C		Correlation function
C_p		Recovery coefficient
c_p		Specific Heat
D		Diameter
D_{eq}		Hydraulic diameter
df		Sampling frequency
f		Frequency
f_{stall}		Stall frequency
F_{stall}		Stall force
g		Acceleration of gravity
h		Enthalpy

H		Prevalence
I		Rothalpy
k		Specific Heat Ratio
m		Mass Flow
M	=V/a	Local Mach Number
MAX		Maximum Bearings Stiffness Condition
MIN		Minimum Bearings Stiffness Condition
M_u	$= u_2/a_{00}$	Peripheral Mach Number
n		Speed
N		Number of lobes
p		Pressure
Q		Volumetric Flow
R, r		Radius
Re	$= \rho VD/\mu$	Reynolds
s		Entropy
T		Temperature
t		time
u		Peripheral speed
w		Relative velocity
W		Work
x,y		Generic phenomena/quantities
Z		Number of blades

Subscripts

des	Design point
l	Lobe
Sect	Analyzed section
00	Stage inlet
2	Impeller outlet
10	Impeller inlet
20	Diffuser inlet

40		Diffuser outlet
60		Stage outlet

Superscripts

*		Dimensionless value

Greeks

α		Flow angle
β		Blade metal angle
γ		
λ		Number of lobes
μ		Dynamic viscosity
ψ		Perturbation amplitude, Azimuthal angle
ρ		Density
σ		*Slip factor*
θ		Generic angle
τ	$=\frac{c_p \Delta T}{u_2^2}$	Work Coefficient, Time shift
ω		Revolution velocity
α_{2r}		Reverse flow angle
η_p		Polytrophic efficiency
Δr		Reverse flow range (Kobayashi *et al.* 1990)
$\Delta\alpha$		Geometrical shift between two sensors
$\Delta\vartheta$		Phase Shift Between Two Sensors
$\tau\eta_p$		Head Coefficient
χ		Dimensionless Force Coefficient
ϕ, φ	$=\frac{Q_{00}}{u_2 \cdot R_2^2 \cdot \pi}$	Flow Coefficient

Introduction

The most recent industrial tendencies for centrifugal compressors are mainly focused on finding solutions both to maximize the efficiency and to extend the limits of the operating curve in order to improve the flexibility of the machine. If, on one hand, the efficiency is reaching a technologic limit, the extension of the minimum flow limit has still room for improvement. Moreover, new compressor designs have to meet the customers' needs in terms of reduced time-to-market and low costs.

Within this scenario, efforts have been devoted by the research on analyzing the unsteady phenomena that precede the surge and determine the left limit of the curve both by decreasing the performance and by generating severe subsynchronous vibrations to the rotor.

Rotating stall represents one of the main unsteady phenomena which not only adversely affects the performance of the compressor, but also can generate severe subsynchronous vibrations to the rotor preventing the machine to operate beyond this limit.

In particular, an accurate characterization of rotating stall could play a key-role in high-pressure centrifugal compressor design.

Moreover, even if many research papers have been directed at investigating the physics of the phenomenon, the influence of the main parameters and the prediction of the stall inception, only few works focused the attention on the characterization of the rotating stall from an industrial point of view. In other words, an accurate procedure to analyze the pressure pattern due to rotating stall could lead to the

development of a systematic approach able to predict the real behavior of the compressor in these particular unsteady conditions.

With this in mind, a strong collaboration between the *Department of Industrial Engineering* of the University of Florence and *GE Oil & Gas – Nuovo Pignone* was started to develop a systematic approach both to characterize the industrial rotating stall and to predict the behavior of the machine in case of operation in stall conditions.

In this study, the attention is mainly focused on the vaneless diffuser rotating stall, which generally occurs as a result of a separation of boundary layer and consequently a reverse flow.

Before analyzing the rotating stall, a review both of the measurement techniques and of the stall investigation methodologies was needed in order to properly choose the most adequate for this work.

If on one hand the advanced techniques currently used in the academic field shows a wide scenario, on the other hand their direct and spread application to the industrial world is definitely difficult in many cases, due to either complexity or cost reasons. As a consequence, a consolidated technology with limited costs and able to be quite easily integrated with a conventional test set-up, as dynamic pressure probes, was preferred to investigate the rotating stall. In particular, this kind of sensors is mainly used to determine the stall onset and evaluate the amplitude of the subsynchronous frequency in order to define the stall margin by comparing the measurement with a limit value.

The purpose of the first part of this study was to develop a systematic approach based on the manipulation of the experimental data coming from dynamic probes which allowed to reconstruct the pressure unbalance in the vaneless diffuser during stall conditions.

In the second part of the study the procedure was then applied on a subset of experimental data related to more than 60 single stage model tests to characterize the vaneless rotating stall in terms of stall frequency, force and geometry parameters.

Some guidelines for a correct investigation in terms of sensors' number and relative positioning are introduced in order to detect more accurately the stall characteristics in terms of frequency and number of rotating cells.

The developed procedure also allows one to estimate the impact of the rotating stall on the rotordynamic behavior of a centrifugal compressor by calculating a rotating stall force due to the pressure unbalance during the unsteady functioning.

An accurate estimation of the resulting aerodynamic force could in fact provide useful information both to identify the actual operating conditions and to improve the operating compressor range by evaluating if rotating stall could represent a problem for the rotordynamic response of the compressor.

To reach this goal, a scaling criterion has been developed and verified by means of both experimental data, coming from model tests (a scaled single stage) and multistage compressors. Numerical simulations performed with a specific rotordynamic code confirmed the validity of the approach.

In particular, this can be considered the first systematic attempt to transfer the aerodynamic stall force calculated by means of dynamic pressure probes, installed in a model test, into a predicted vibration level of the whole compressor operating in similar conditions.

In the last part of the study, a rotordynamic analysis campaign has been carried out on different case studies in order to evaluate the actual impact of the rotating stall force by varying its amplitude, frequency and journal bearings characteristics. In particular, the attention has been focused on the safety margin theoretically available to let the machine operate safely beyond the stall onset.

In this study, the main outcomes of the research are presented.

In particular, Chapter 1 contains some information on the thermodynamics and mechanics of centrifugal compressors.

In the Chapter 2 the fundamentals of the rotating stall (with particular reference to the vaneless diffuser stall) are described; furthermore, the state of art of the current methodologies to investigate the stall are presented and discussed in order to give an overview on the objectives of the present work.

The procedure to analyze the vaneless diffuser rotating stall and derive the associated aerodynamic force is described in Chapter 3; before entering in the description of the approach, fundamentals of the measurement techniques used are introduced in order to optimize the results.

Chapter 4 is focused on the application of the procedure to several model test carried out at *GE Oil & Gas* test-rig. Once the vaneless diffuser rotating stall has been characterized in terms of frequency, number of lobes and rotating force, based both on the results and on open literature, a criterion to scale the force from model test conditions to real operating conditions is introduced and discussed.

In order to verify the scaling criterion and the prediction capability of the entire approach, a numerical rotordynamic campaign is presented in Chapter 5 coupled with experimental data coming both from model tests and multistage compressors.

1. The centrifugal compressor

1.1 Introduction

Centrifugal compressors have a wide range of applications that starts from the aviation field (high pressure ratio, up to 8:1) to arrive to the industrial use.

The high level of centrifugal compressors in term of performance reached in the last years is mainly due to the compactness, the low number of components and the use of new materials. The efficiency remains under that one obtained by an axial compressor, but it is possible to go beyond the 80%. However, the high interest in this machine is due to the robustness, the simplicity of construction and first of all to the possibility to reach a certain level of power with respect to the "small" dimensions.

In Figure 1-1 is reported a scheme of a single stage centrifugal compressor: the operating machine is characterized by an external case in which is collocated an impeller rigidly connected to a shaft. The impeller rotates thanks to a gas or a steam turbine or an electric motor. The stator downstream the impeller allows to recover the kinetic energy of the flow by decreasing its velocity.

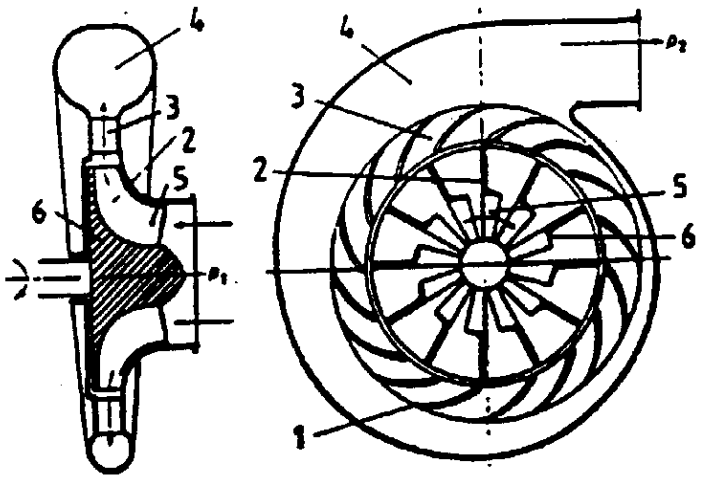

Figure 1-1. Scheme of a centrifugal compressor.

Generally, for industrial applications at high pressure, a multistage compressor represents a better solution than the single stage (Figure 1-2). In this case the machine is constituted by an external case (A) which contains both a part of the stator (B) and a rotor (C) and one or more impellers (D).

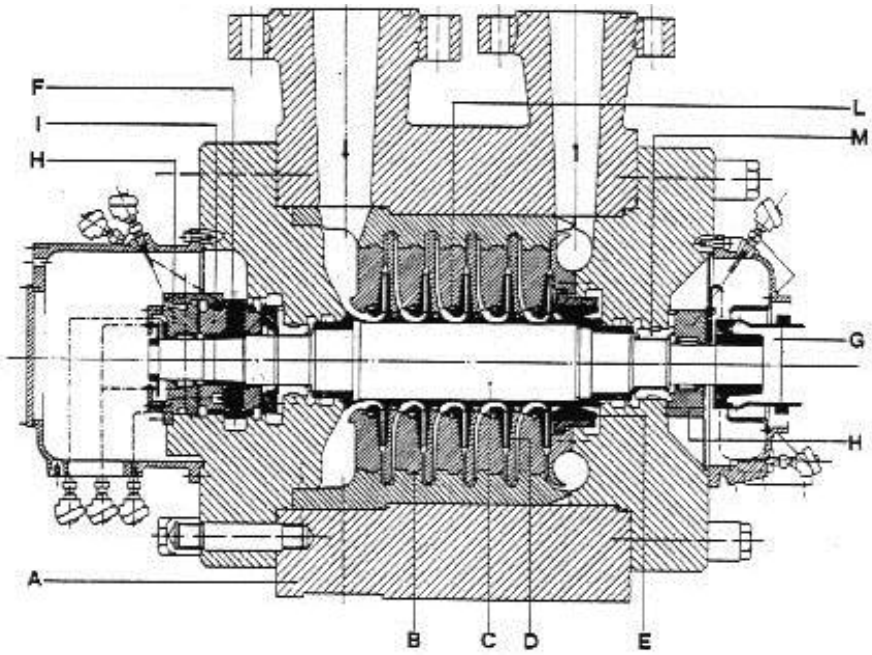

Figure 1-2. Scheme of a multistage centrifugal compressor.

Centrifugal compressors have different typologies of design depending on its particular function and working pressure. In the compressors in which a high performance is pursued, an *unshrouded* impeller is preferred: the moving blades move past the stationary shroud with a small clearance. The impeller has a predominant axial inlet which is named *inducer*. The impeller blades are inclined backwards at outlet and it is known as *backsweep*. In Figure 1-3 it is possible to see that some of the blades do not extend from outlet to inducer (*splitter*). This kind of blades are used because the additional number of blades is needed towards the outlet but this number of blades would, if continued to leading edge, produce sufficient blockage to cause chocking there at high speeds and flows.

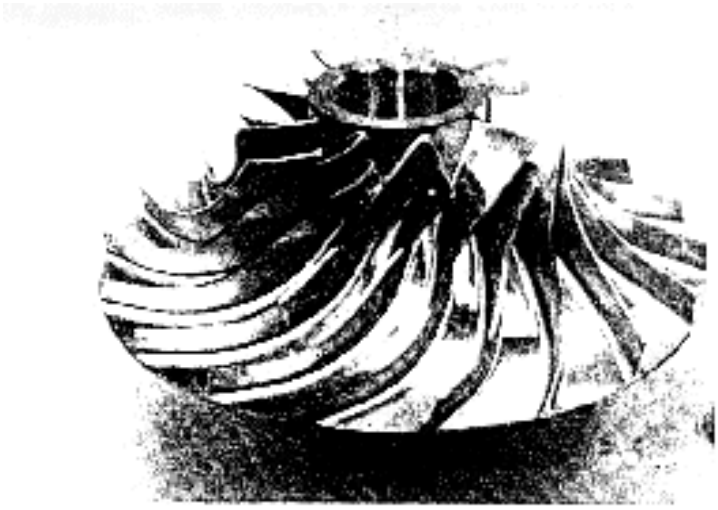

Figure 1-3. Impeller with *splitter* blades.

Machines for industrial use are not usually provided by *inducers*; they have a pure radial outlet and a rotating shroud fixed to the blades. Rotating shrouds avoid the need to maintain a small clearance between the moving and stationary parts, but at the same time this solution adds significant extra ass which can produce very high stresses at high speeds (Figure 1-4).

Whether high performance or low cost are pursued the attraction of the radial machine remains the same; the increasing of the enthalpy and of the static pressure is mainly due to centrifugal phenomena which depend only upon the impeller blade speed at inlet and outlet. Furthermore, the work input is almost independent of the

nature of the flow and it is not affected by discontinuity near the stall, unlike the axial machine.

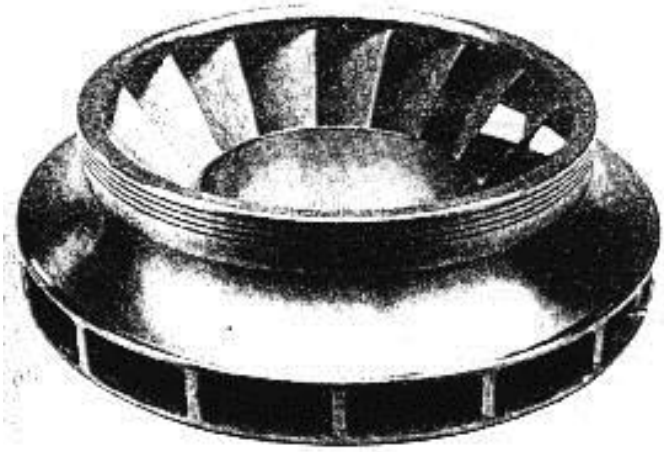

Figure 1-4. Industrial impeller

1.2 Monodimensional analysis of a single stage

Consider Figure 1-5, which represents a generic compression process in the Mollier plane (enthalpy-entropy) taking place in a single compressor stage.

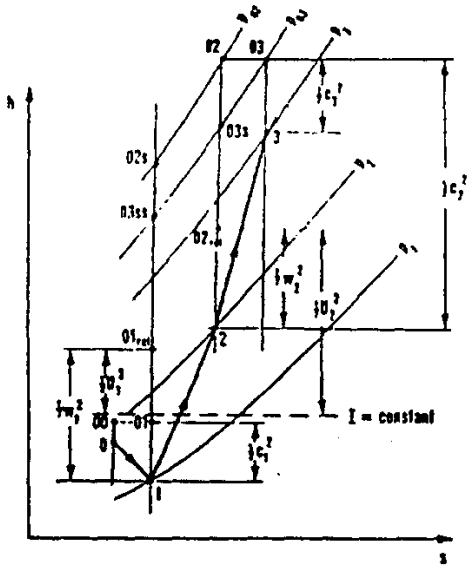

Figure 1-5. Entropy-Enthalpy digraph of a compression process.

The fluid, taken in determined conditions p_{00} and T_{00}, is subsequently accelerated up to the inlet to the stage where it reaches the conditions defined by thermodynamic state 1. Since the inlet zone is a stator, no energy transfer takes place; while the total enthalpy remains constant, the static and the total pressure decrease.

$$h_{t0} = h_0 + \frac{c_0^2}{2} = h_{t1} = h_1 + \frac{c_1^2}{2} \qquad \text{Eq. 1-1}$$

The acceleration process is accompanied by dissipation phenomena linked to the increase in speed of the fluid. In flowing along the impeller the fluid increases also the pressure and the enthalpy.

$$L_{1-2} = (h_2 - h_1) + \frac{c_2^2 - c_1^2}{2} \qquad \text{Eq. 1-2}$$

Then in the diffuser the kinetic energy of the fluid is converted into potential energy by increasing the static pressure. In this case the enthalpy remains constant since it is a stator part.

$$h_{t1} = h_1 + \frac{c_1^2}{2} = h_2 + \frac{c_2^2}{2} = h_{t2} \qquad \text{Eq. 1-3}$$

Finally, the fluid is gathered in the scroll where a further diffusion occurs; also in this case the enthalpy remains constant.

$$h_{t3} = h_3 + \frac{c_3^2}{2} = h_4 + \frac{c_4^2}{2} = h_{t4} \qquad \text{Eq. 1-4}$$

The losses are present in each component of the stage: they can be evaluated in the diagram h-s by considering the total pressure decreasing.

1.3 Work at the inlet of the compressor

In Figure 1-6 is reported a scheme of an ideal impeller in which the inlet flow has a radius r_1 and a tangential velocity $c_{\theta 1}$ and the exit flow has a radius r_2 and a

tangential velocity $c_{\theta 2}$. Utilizing the equation of balance of momentum for the stationary flow between two sections, it is possible to obtain:

$$T = m\left(r_2 C_{\theta 2} - r_1 C_{\theta 1}\right) \qquad \text{Eq. 1-5}$$

and the work per unit can be written in the Euler form as:

$$W = \omega\left(r_2 C_{\theta 2} - r_1 C_{\theta 1}\right) = U_2 C_{\theta 2} - U_1 C_{\theta 1} \qquad \text{Eq. 1-6}$$

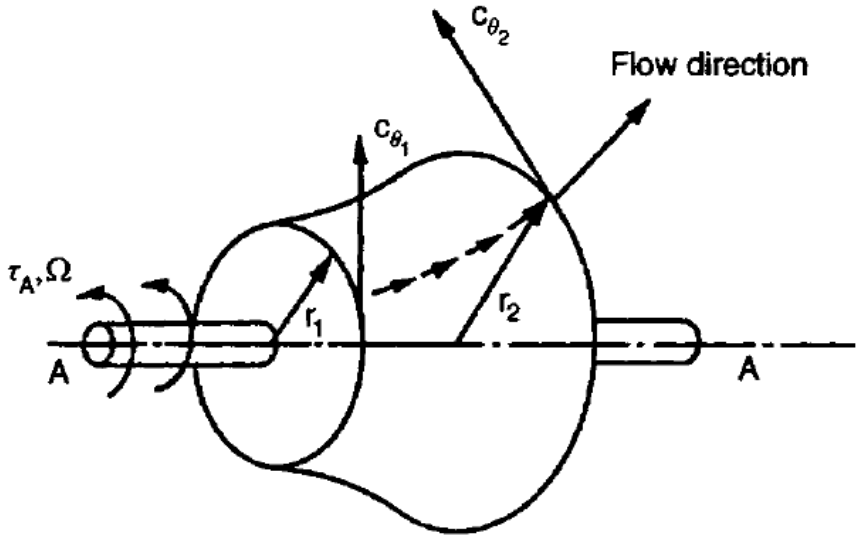

Figure 1-6. Ideal impeller

Now considering the energy equation:

$$Q + W = h_{02} - h_{01} \qquad \text{Eq. 1-7}$$

One can readily notice that in this equation the work W is positive since in the Euler equation Eq. 1-6, the work on the fluid is taken positive. Considering the compressor as adiabatic (Q = 0) and introducing the Eq. 1-6 in the Eq. 1-7:

$$h_2 + \frac{C_2^2}{2} - U_2 C_{\theta 2} = h_1 + \frac{C_1^2}{2} - U_1 C_{\theta 1} \qquad \text{Eq. 1-8}$$

According to Figure 1-7, the velocity can be written in the local coordinates as:

$$C_{\theta 2} = W_{\theta 2} + U_2 \qquad \text{Eq. 1-9}$$

After few passages the Eq. 1-8 become:

$$h_2 + \frac{W_2^2}{2} - \frac{U_2^2}{2} = h_1 + \frac{W_1^2}{2} - \frac{U_1^2}{2} \qquad \text{Eq. 1-10}$$

Or:

$$\left(h_{02}\right)_{rel} - \frac{U_2^2}{2} = \left(h_{01}\right)_{rel} - \frac{U_1^2}{2} \qquad \text{Eq. 1-11}$$

Where $\left(h_{02}\right)_{rel}$ represent the total enthalpy of the system in the local coordinates.

Defining the Rothalpy as:

$$I = h + \frac{W^2}{2} - \frac{U^2}{2} = \left(h_0\right)_{rel} - \frac{U^2}{2} \qquad \text{Eq. 1-12}$$

The Eq. 1-10 becomes:

$$I_1 = I_2 \qquad \text{Eq. 1-13}$$

In the rotor part the rothalpy has the same characteristics of the total enthalpy in the stator part; some assumptions, however, must be done:

- Steady flow in the relative system.
- W = 0 in the relative system.
- Q = 0.

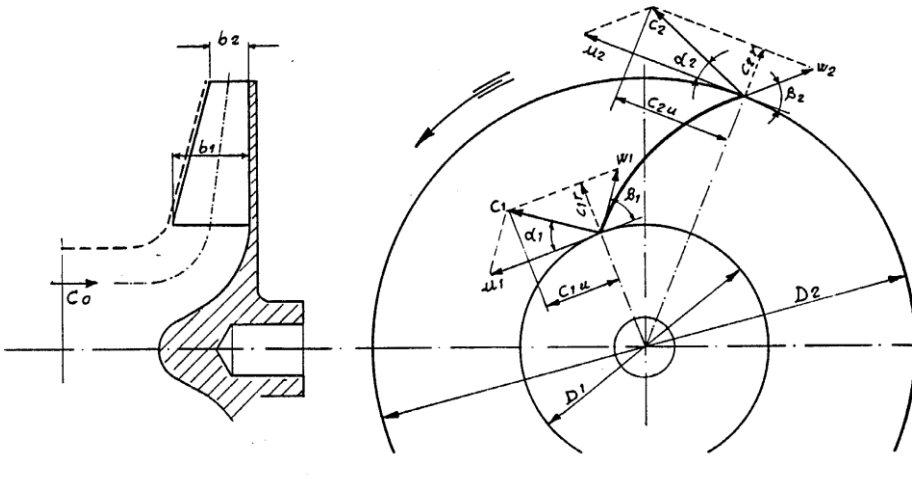

Figure 1-7. Velocity triangle at the inlet and the outlet of the impeller.

Moving this concept to the whole compressor, where the main goal is to increase the static pressure of the fluid (i.e. the static enthalpy), one can easily write.

$$h_2 - h_1 = \frac{1}{2}\left(W_1^2 - W_2^2\right) + \frac{1}{2}\left(U_2^2 - U_1^2\right) \qquad \text{Eq. 1-14}$$

So the increasing of the static pressure is given by two main contributes:

- The flow diffusion in the relative system.
- The centrifugal force due to the impeller rotation.

1.4 Physics of the impeller

1.4.1 Introduction: the role of the impeller

The impeller has a key role in a compressor stage. As described by Euler equation (Eq. 1-6), this component is responsible for the energy transfer to the fluid.

Following a fluid element toward the impeller, it is worth to remark that a fundamental function of the impeller is to decrease the static pressure at the inlet in order to flow towards the impeller and then into the impeller. In absence of preswirl and inlet recirculation (which is a precaution that can be used in case of stall onset or

surge) the flow will move axially towards the eye of the impeller. Then as soon as the flow approaches the leading edge of the impeller blades, it begins to follow a pseudo-helical pattern through the impeller domain.

Once the fluid is inside the impeller, it receives an important pressure rise that mainly depends to $\omega^2 r^2$. In other words, the pressure is proportional to the square of U^2 or $M_u{}^2$. Moreover, the flow has a certain relative kinetic energy which can assume a very high value, or a low value, according to the stage work input. Obviously, in case of a high value, the designer should focus on the flow diffusion to guarantee proper stage efficiency.

Each passage between two blades of a centrifugal compressor can considered as a rotating diffuser. Unlike a classic diffuser, this passage is a complex diffuser with all the influences of curvature and rotation.

At the outlet of the impeller a region of a low momentum fluid and a high energy core are present; these two conditions produce strong variations that generate an entropy increase, i.e. a total pressure loss. In such mixing processes there is also a static pressure rise, which is generally considered beneficial.

1.4.2 Impeller inlet flow

The design of the inducer is based on the inlet relative velocity, *W*, the level of incidence, $i = \beta_b - \beta$, the level of the preswirl, C_θ and the local acceleration effects due to the passage around the blade leading edge.

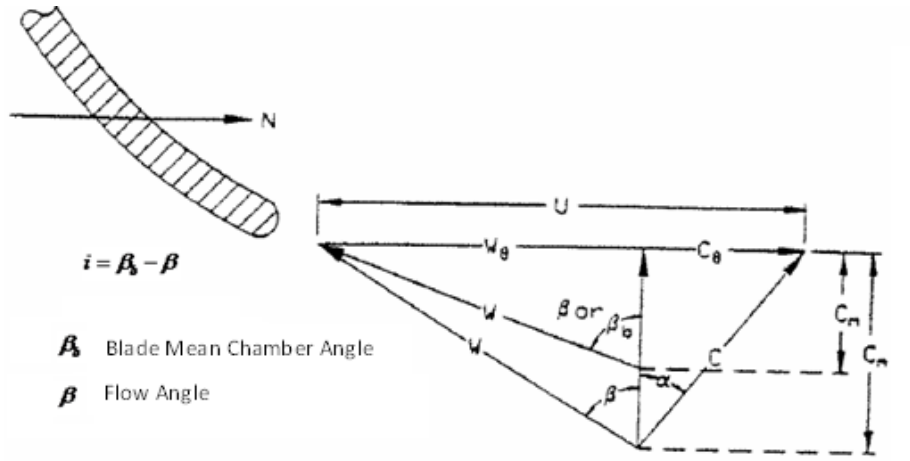

Figure 1-8. Inducer velocity triangle (Japikse D., 1996).

Each compressor needs to have the control of the level of incidence. Ideal incidence should be correspond to a value close to zero, although it may correspond to a positive value of several degrees or a negative value. It is worth to remark that it is not possible to have large degrees of incidence without an adverse effect.

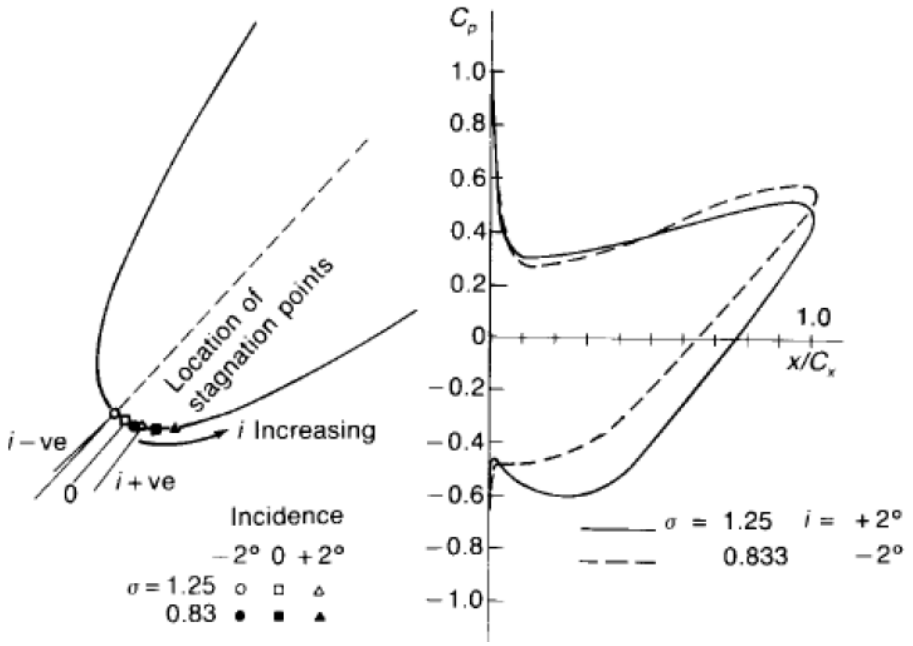

Figure 1-9. Incidence effect on the impeller blades (Cumpsty, 2004).

Experimental analyses highlighted that the optimum value of incidence is close to zero [1]. It is also recognized that there is a convenience in having the stagnation point near to the leading edge, in particular at high inlet Mach numbers.

In Figure 1-9 are shown the variations around the leading edge for small changes in incidence at an inlet Mach number equal to 0.7. The position of the stagnation point depends on various parameters, but the main ones are represented by the mean inlet flow direction, the thickness of the leading edge, the solidity and the camber.

Increasing the incidence brings the stagnation point around the pressure side of the blade. Similar results are obtained by reducing the solidity. In each case the effect of the stagnation point is to produce a negative peak in the pressure distribution on the suction side.

Thus, the range of stall-free functioning is a function of a Mach number (Figure 1-10).

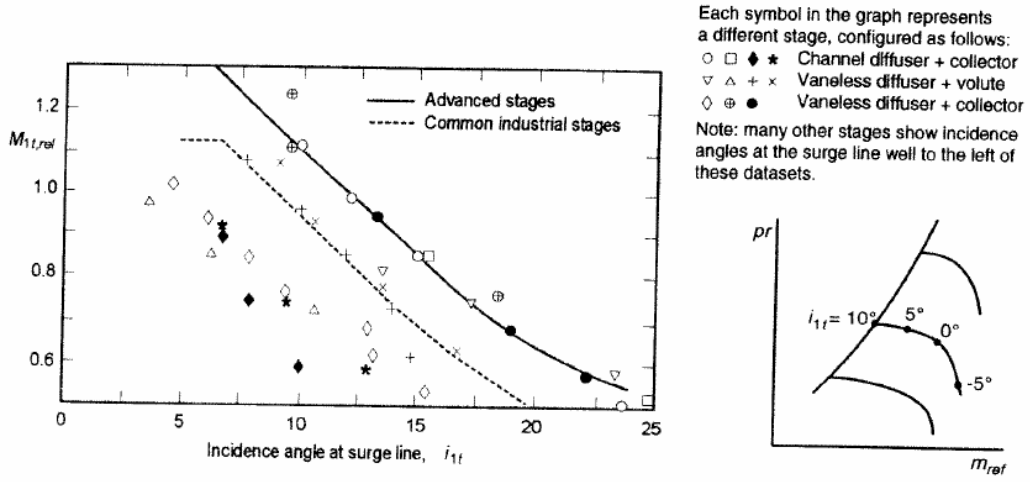

Figure 1-10. Surge line incidence comparison (Japikse, F., 1996).

Examples of inducer flow phenomena at various level of incidence are shown in Figure 1-11. After a limit value of the incidence the stall can occur and a consequent reduction in performance could appear due to the increase of the losses.

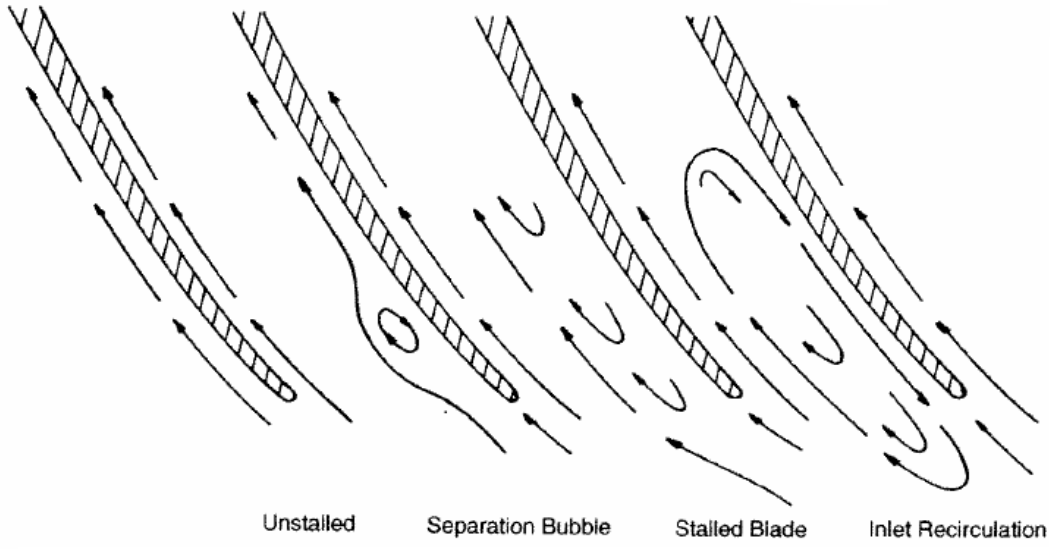

Figure 1-11. Effects of the level of incidence on the inducer. Incidence increases from left to right (Japikse, F., 1996).

The influence of compressibility is important in particular when the Mach number has a transonic value. High local Mach numbers can be reached with an inlet Mach number of only 0.7 or greater. The flow accelerates to pass around the leading edge of the inducer, reaching very high local Mach numbers. When this Mach number exceeds the unit locally, severe shock wave starting from the blade leading edge can be produced. Small shocks have not significance influence, but only a modest Mach number is needed to rise the pressure up to separate the boundary layer. If the boundary layer is separated by a shock, it may be quickly reenergized and the reattached, but, in case the blade has a strong curvature and strong passage diffusion, the boundary layer can remain stalled throughout the impeller.

Blade thickness plays a key role in the local acceleration and, therefore, in local Mach numbers and incidence sensitivity. In the design of high Mach numbers impeller, it is important to have thin leading edge and straight inducer blading. With thin blades it is possible to minimize the influence of blade blockage and consequently the flow acceleration (i.e. the entity of the shock).

The first step in the inducer design, both subsonic and transonic, is to optimize the velocity triangle at the inlet. The velocity triangle (Figure 1-8) is defined according to the following equations:

$$i = \beta_b - \beta$$ Eq. 1-15

$$U = 2\pi r N$$ Eq. 1-16

$$C_m = \frac{\dot{m}}{\rho A_f}$$ Eq. 1-17

Where: $A_f = C_D \pi \left(r_t^2 - r_h^2 \right)$ and $C_D = 1 - B_1$.

$$\frac{p_0}{p} = \left(1 + \frac{\gamma - 1}{\gamma} M^2 \right)^{\frac{\gamma}{\gamma - 1}}$$ Eq. 1-18

$$\frac{T_0}{T} = 1 + \frac{\gamma - 1}{\gamma} M^2$$ Eq. 1-19

$$C = \sqrt{C_m^2 + C_\theta^2}$$ Eq. 1-20

$$W = \sqrt{\left(C_\theta - U \right)^2 + C_m^2}$$ Eq. 1-21

$$M_{rel} = \frac{W}{\sqrt{\gamma R T}}$$ Eq. 1-22

In the centrifugal compressors design, the level of local Mach number at each stage inlet would be limited in order to minimize the loss of the impeller in the inducer. At the outlet of the impeller, there must be an adequate number of blades if the loading is to be kept within certain limits. If this number were to be continued to the inlet of the inducer their blockage would be a great constraint on the mass flow in high pressure ratio machines. The solution usually adopted is the use of *splitter* blades which end somewhere downstream of the inducer.

1.4.3 Impeller internal flow

As the flow enters the impeller passage, boundary layers begin to develop on all blade surfaces (*hub* and *shroud*). The core flow tends to follow the blade passage assuming a uniform flow condition at the inlet of the impeller. If there is a distortion at the inlet, then the core flow will be marked with a passage vortex from the beginning. However, both the core and the boundary layers are affected by a very strong force field, in particular the Coriolis force field. This force is selective basing on the flow velocity and it acts by separating the high velocity and low velocity elements. A secondary flow around the core flow is developed: a low momentum fluid portion moves near the shroud suction surface and the high momentum fluid portion near the hub pressure area. One can readily notice the development of this flow pattern by considering the flow measurements at various stations collected by Eckardt (1980) and reported in Figure 1-12. It is worth noticing that a strong secondary flow appears through the passage and moves to the shroud suction surface corner. The velocity station marked as I, highlights a classical pattern of flow with a core flow at high momentum and thin boundary layers along the wall. The slightly inclination is due to the aerodynamic loading of the blades on the flow.

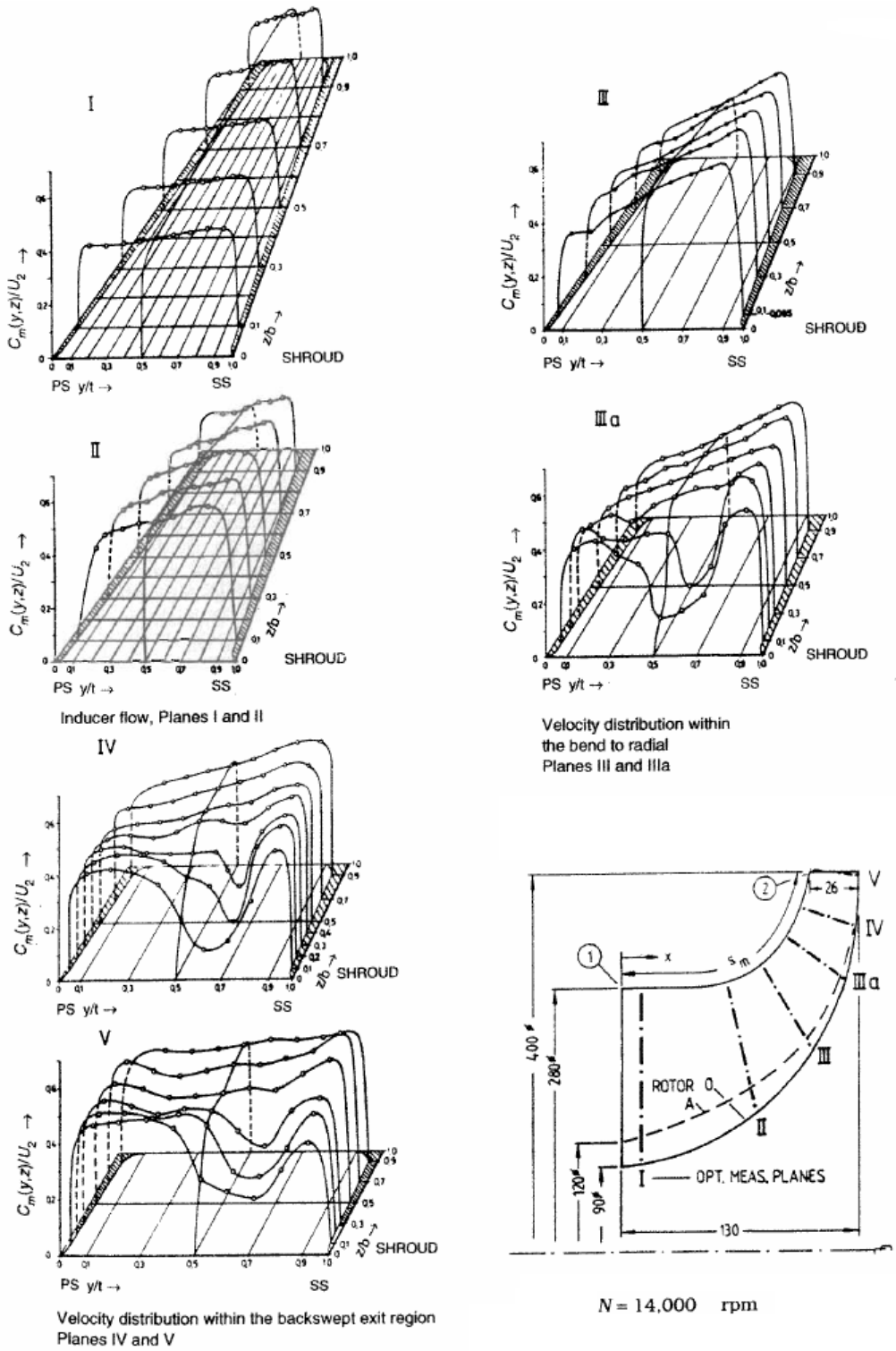

Figure 1-12. Flow measurements inside a centrifugal impeller at various stations (Eckardt 1980).

The velocities at the second plane (II) are similar to the previous: the main difference consists in the strength of the velocity distribution that in this case is stronger. The same considerations can be made for the locations III and III_a.

At section III_a can be observed a new phenomenon along the shroud and near the suction side of the blade. In this zone a huge momentum deficit appears. Eckardt considered this zone as the development of a separated flow and described it as a "*wake*" region. However, the velocity in this zone is not equal to zero so it cannot be considered a true *wake*, but a low momentum fluid better described as a secondary flow. This effect continues at section IV and V and the flow that leaves the impeller has a significant momentum deficit in the shroud suction side.

Making a time average from hub to shroud at section V, one can readily notice that the momentum will be significant deficient in the shroud region and will be strongly energized near the hub. Due to this, also the angle distribution from hub to shroud results affected and the flow at the outlet of the impeller will be nearly tangential near the shroud and more radial near the hub (*jet*). This represents the typical problem in diffusers design.

The velocity triangles result quite different for the primary flow (*jet*) and the secondary flow (*wake*) as shown in Figure 1-13. It is worth noticing that the secondary flow with a low momentum, as described in the relative system, can have a higher energy or momentum level in the absolute system.

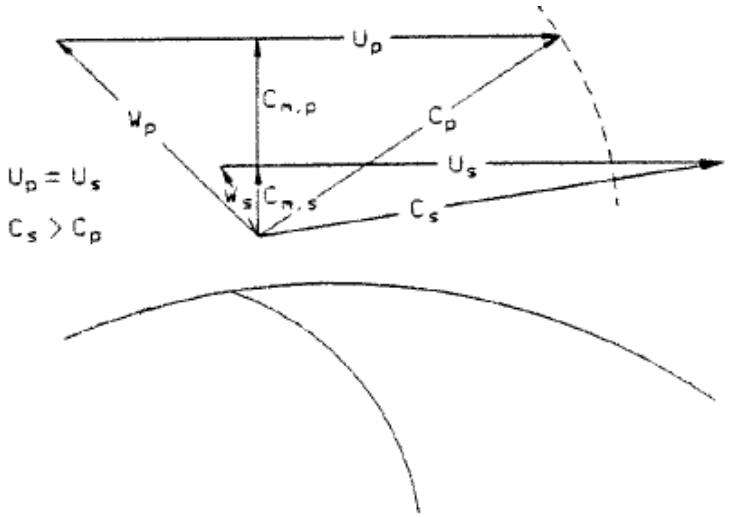

Figure 1-13. Velocity triangles for the "*jet*" and "*wake*" zones.

1.4.4 Mixed flow at the exit of the impeller

The flow leaves the exit of the impeller in a strong tridimensional condition and enters in the diffuser. In details it has a high absolute velocity, generally inclined at a large angel with respect to the radial direction. In order to guarantee a high pressure ratio and a high efficiency, a deceleration of the flow is needed. For these reasons, a diffuser, which can be *vaneless* or *vaned*, is generally collocated downstream of the impeller. Only in a few applications at low velocity, the scroll is directly linked to the impeller exit.

The design of the diffuser results a crucial point to obtain high performance. The flow diffusion should be carried out by minimizing the losses.

With this goal in mind, Dean and Senoo (1960) proposed a theory in which the flow at the exit of the impeller was modeled as two-dimensional with the *jet* and *wake* dividing the passage in the circumferential direction (Figure 1-14).

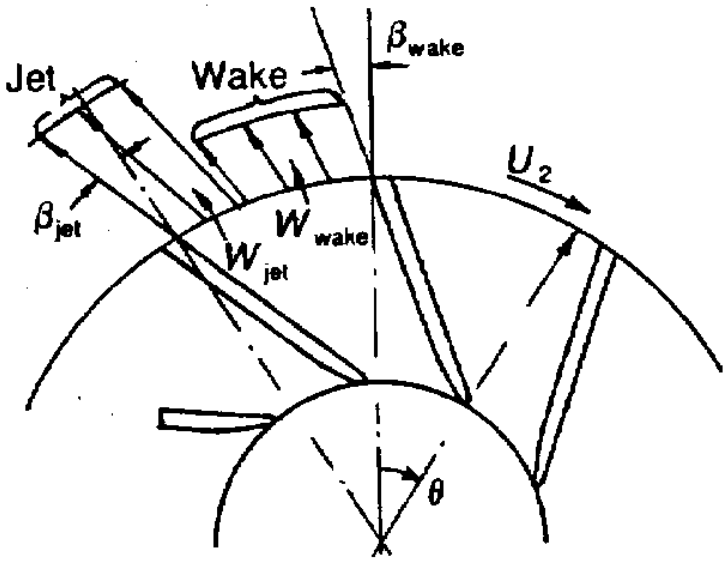

Figure 1-14. The *jet* and *wake* model.

In their analysis they considered the fluid as incompressible and the flow direction (not the magnitude) was assumed uniform in the circumferential direction. Applying the equations of mass continuity and conservation of radial and tangential momentum separately to the wake and the jet regions, they obtained a differential equation in the

radial direction. By integrating this, they described the flow development to the uniform condition. The model took into account also the skin friction at the wall of the vaneless diffuser and the shear stress between the jet and the wake. This model allowed to evaluate the losses and to predict the increasing of the static pressure in a good agreement with the experimental data.

Johnston and Dean (1966) considered the mixing of the non-uniform impeller flow as a sudden expansion of the jet and wake to create a uniform flow. This assumption was in agreement with the Dean and Senoo theory and allowed a simplification of that method. Furthermore, this approach could be applied both to different geometries and various compressible values.

Eckardt (1975) carried out experimental tests to measure the flow in the discharge of a centrifugal compressor. In the Figure 1-15, taken from Eckardt (1979), some measurements of the radial velocity distortion across the vaneless diffuser passage at four radius ratio for the flow coefficient in which the highest efficiency was reached is shown. It is important to notice that the previous theories, which predicted a uniform flow for a radii ratio over 1.2, seem to be able to correctly estimate the losses related with the mixing flow process. This implies a high unsteady flow in vaned diffusers and a possible cause of the stall onset in vaneless diffusers.

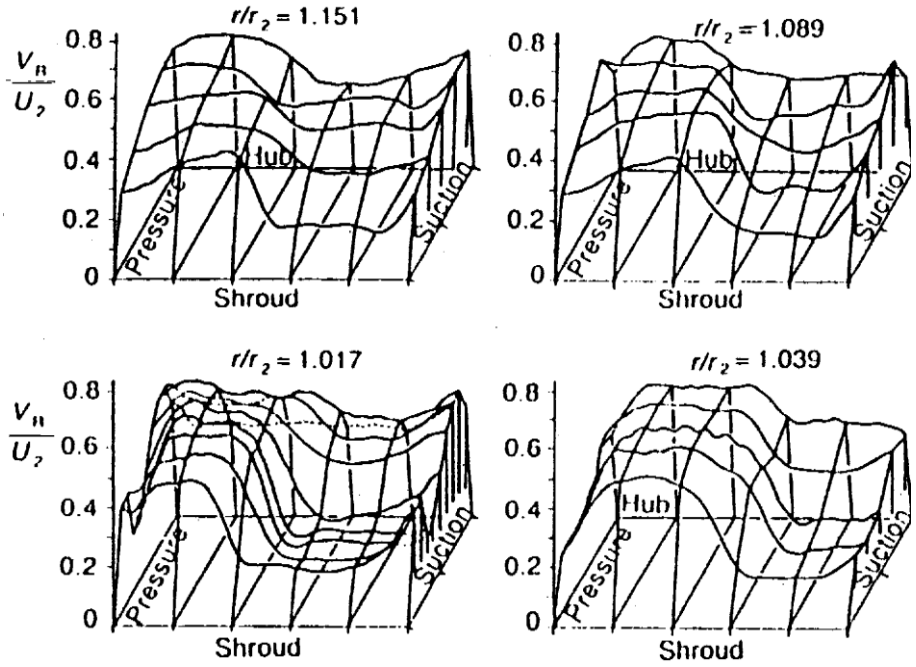

Figure 1-15. Flow non-uniformity at the exit of the impeller.

1.4.5 The vaneless diffuser

The kinetic energy of the flow that leaves the impeller of a centrifugal compressor stage is equal to about 30-40 % of the total work on the fluid. In a well-designed diffuser, this kinetic energy must be recovered efficiently. Compressor diffusers convert kinetic energy into static pressure by using two main techniques (Figure 1-16):

- A flow passage increasing which brings a reduction in the average velocity, i.e. a static pressure increasing.
- A change in the mean radial flow path which brings to a tangential velocity recovery, in agreement with the momentum conservation, $rC_\theta \approx$constant.

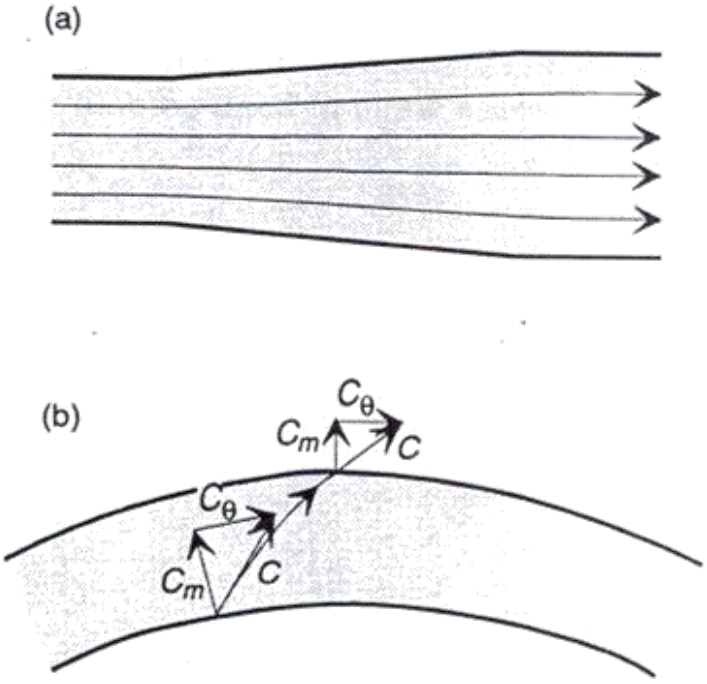

Figure 1-16. Scheme of the contributes in the recovery pressure.

Since the pressure recovery by means of diffusion can lead to stability problems, it is important in diffusers design to take into account these aspects. Some of the main effects involve modes where separation or stall can be encountered.

The vaneless diffuser is usually used in process compressors, refrigeration compressors and turbocharger compressors since they guarantee a good level of pressure recovery and low costs. For these reasons they are often preferred to those vaned which allow a high pressure recovery but a limited range of functioning.

Basically, it is composed by two parallel walls that form an open radial annular passage from impeller *tip* to some limiting outer radius (return channel, volute). In Figure 1-17 are presented some examples of vaneless diffusers coupled with the impeller exit. The most common configuration is the *pinched* one; in this case the vaneless diffuser has an area reduction which provides a proper stabilization of the flow.

A characteristic of the vaneless diffuser is the impossibility to reach the *choke* condition; this allows a wide range of functioning. Moreover, the lack of diffuser

vanes implies that no vibrations due to the blades interaction (impeller and diffuser) are observed.

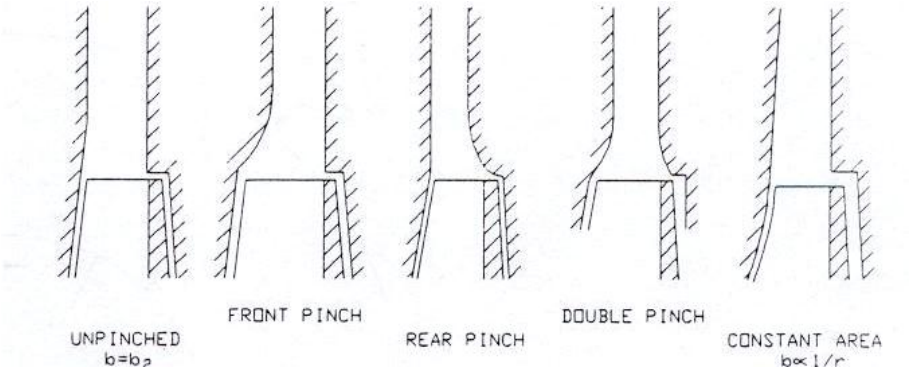

Figure 1-17. Common vaneless configurations.

An easy description of vaneless diffuser performance is shown in Figure 1-18 and in the following equations:

$$rc_u \approx costante$$
$$\rho c_m 2\pi \cdot rb = m \qquad \text{Eq. 1-23}$$
$$tan\alpha = \frac{c_u}{c_m} \approx costante \times \frac{\rho b}{m}$$

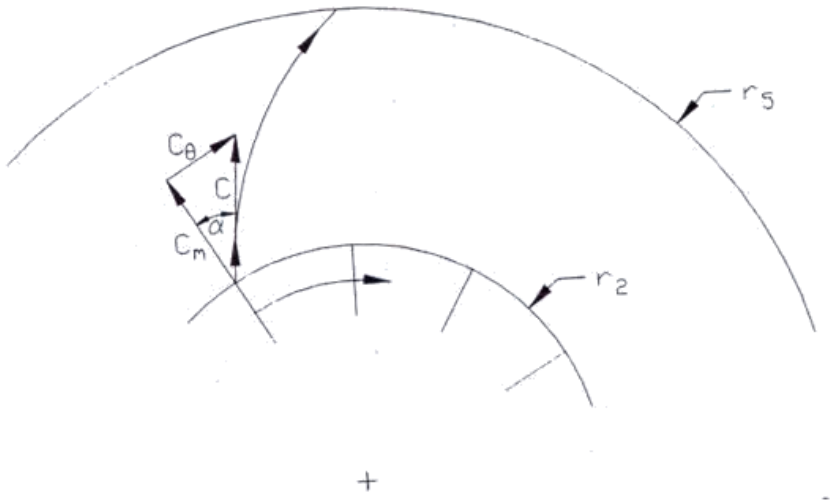

Figure 1-18. Velocity triangles in vaneless diffuser.

These equations represent the conservation of mass and angular momentum and show that the flow angle in the vaneless diffuser mainly depends on density and passage width. In this case a constant width will be considered.

For a constant density fluid, the flow angle is constant along the diffuser and it forms a logarithmic spiral flow path. However, the flow is really affected by viscous effects that deflect the flow direction with respect to the logarithmic spiral.

A more in depth knowledge of the vaneless diffuser can be achieved by integrating the conservation equations along the vaneless diffuser. The full set of equations take into account the wall friction effects in both the linear and angular momentum equations (Stanitz, 1952):

$$c_m \frac{dc_m}{dr} - \frac{c_\vartheta^2}{r} + C_f \frac{c^2 \cos\beta}{h \sin\phi} + \frac{dp}{\rho dr} = 0 \qquad \text{Eq. 1-24}$$

$$c_\vartheta \frac{dc_\vartheta}{dr} + \frac{c_m c_\vartheta}{r} + C_f \frac{c^2 \sin\beta}{h \sin\phi} = 0 \qquad \text{Eq. 1-25}$$

$$\frac{dp}{\rho dr} + \frac{dc_m}{c_m dr} + \frac{dh}{h dr} + \frac{1}{r} = 0 \qquad \text{Eq. 1-26}$$

$$\rho = p / RT \qquad \text{Eq. 1-27}$$

$$T_0 = T + c^2 / 2C_p \qquad \text{Eq. 1-28}$$

where ϕ is the diffuser inclination with respect to the axial direction.

This set of equations can be solved by using the Runge-Kutta method, but an appropriate friction coefficient C_f to get reasonable prediction is needed. Furthermore, since the flow in the diffuser has a complex development, the skin friction coefficient must be adjusted depending on the specific industrial application. Values of C_f can be used as average for the entire diffuser or as a function of geometry and flow coefficient.

$$C_f = k\left(\frac{1.8\cdot 10^5}{\mathrm{Re}}\right)^{0.2} \qquad \text{Eq. 1-29}$$

where k is constant that usually have the value equal to 0.010 (Japikse, 1982).

The solution of constant diffuser width is quite simple and commonly used, although other solutions with a decreasing of the width in the radial direction can be adopted. This configuration has the direct effect on the mean radial velocity by means of the equation of continuity, but only a marginal effect on the tangential one. This implies that both the mean streamline from the inlet to the outlet and the losses are reduced. Moreover, the flow angles with respect to the tangential direction are higher than the diffuser with constant width providing the effect to delay the stall onset at low flow coefficient.

A further key-role in the diffuser performance is represented by the compressibility. By assuming that the density increases in line with the rise in pressure, the radial velocity must decrease more quickly with radius than in the incompressible case to satisfy the conservation of the mass flow. The tangential velocity is not instead directly influenced by density and the flow tends to have a trajectory more curved than before and hence a decreasing of the flow angle with respect to the tangential direction. The decreasing of this angle due to the compressibility is one of the most reason why the performance of the diffuser falls off as Mach number reaches high value.

For air, the density changes with the pressure and the temperature in such a way that the flow angel increases with the radius and the flow follows a trajectory closer

than the logarithmic spiral. Conversely, certain Freon decreases this angle. The flow angle can also be modified by varying the passage width, by pinching or enlarging.

By comparison with a vaned diffuser of similar performance, the vaneless diffuser has greater losses due to the longer fluid path than would be encountered in a channel or cascade diffuser.

To analyze the diffuser performance one can refer to the pressure recovery coefficient:

$$C_p = \frac{p_3 - p_2}{p_{t2} - p_2} \qquad \text{Eq. 1-30}$$

where with the subscript 3 represents the section at the outlet of the diffuser.

Rodgers (1982) carried out some tests and showed results based on 15 configurations of vaneless diffuser. These tests were carried out at different peripheral Mach number at the exit of the impeller; in details, $M_u=u_2/a_{10t}$ in the range of 0.6-1.2, where a_{10t} is the total speed of sound at the inlet of the impeller. The diffuser width was constant and the ratio D_2/D_1 was equal to 1.7.

Figure 1-19 reports the results of this experimental campaign in terms of pressure recovery coefficient and the ratio of average inlet radial velocity to tangential velocity; each curve represent a different b/D_2 ratio.

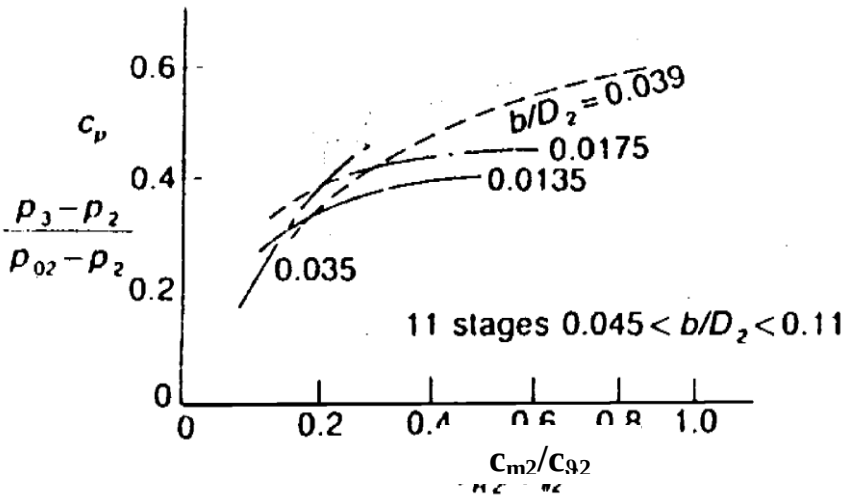

Figure 1-19. Static pressure recovery measured in vaneless diffuser versus $c_{m2}/c_{\vartheta 2}$

After these results two remarks can be done:

- The major part of the diffuser produces almost the same pressure coefficient for the same inlet flow angle, i.e. the same value of $c_{m2}/c_{\vartheta 2}$. One can readily notice that for b/D_2 lower than 0.045 the difference between C_p values is small. For b/D_2 higher than 0.045, not showed, the performance is strongly increased.
- The C_p coefficient increases with the increasing of the ratio $c_{m2}/c_{\vartheta 2}$; in detail the diffuser becomes less effective as the flow becomes more tangential. This effect can be traced back to the higher losses due to the longer flow path.

Another parameter to take into account is the ratio between inlet and outlet diameter D_5/D_2.

Experiments have shown that static pressure continues to increase as the diameter ratio of the vaneless increases, but at a progressively slower rate. At the same time, the total pressure clearly continues to decrease. Since in the external part of the diffuser the velocities are low, the possible recovery of kinetic energy in pressure energy is often limited in order to compensate the increasing of the external diameters.

For this reason the diameters ratio is usually lower than about two and a volute is collocated to achieve the additional pressure rise.

2. Stall in centrifugal compressors

2.1 Introduction

In this chapter the topics of this study will be illustrated together with its collocation in the current literature and state of art. An overview of the stall in centrifugal compressors will be presented through a description of both the characteristics and the methods commonly used to predict or analyze this phenomenon. At the end of the chapter the purposes of this study will be introduced and motivated.

2.2 Rotating stall in vaneless diffusers

Centrifugal compressors show different typologies of unsteadiness when the mass flow rate starts to reduce its value at constant rotational speed. The point in which the flow inside the compressor begins to be unsteady depends both on the compressor type and on the entire circuit linked.

The first type of unsteadiness presented is called surge and it consists of strong pressure and mass oscillations. This unsteady phenomenon is a self-induced oscillation in which the compressor behavior is similar to a resonator. The mean mass flow through the cross section changes with time. The inception and the frequencies of these oscillations depend on the curve of the pressure rise, on the inlet and outlet ducts, on the volumes and on the throttling valve. The surge usually occurs when the

performance curve reaches the zero or the positive slope. If one could operate in the surge zone, it would imply both great losses in terms of efficiency and performance and dangerous subsynchronous vibrations on the blades, the case and the entire circuit.

The second type of unsteadiness, called *rotating stall*, consists of periodic pressure and flow oscillations in one or more different components of the compressor. The steady axisymmetric flow is replaced by rotating cells with high and low pressure. They consist in a phenomenon which rotates at subsynchronous frequency (20-80% with respect to the rotating frequency of the impeller [2]) in the circumferential direction of both the impeller and the diffuser. In the rotating stall, the mean flow rate on a cross section of the compressor remains constant in time with respect to the surge. Moreover, the inception of this phenomenon is not observed only in the region of positive or zero slope of the compressor curve, but also on the negative slope side.

Rotating stall not only adversely affects the performance of the compressor, but also can generate severe subsynchronous vibrations to the rotor, actually preventing the machine from operating beyond this limit [3] [4] [5] [6] [7]. In particular this can be critical at high working pressure because of the high density of the working fluid.

The rotating stall is a non-reversible phenomenon: a significant increasing in the mass flow rate is needed in order to leave the unsteady condition. A slight opening of the throttling valve could not be enough.

Since the rotating stall in vaneless diffusers seems to be caused by a flow inversion inside the boundary layer of the diffuser or by an unsteady interaction between impeller and the diffuser, several studies were devoted to investigate this complex phenomenon. It is worth noticing that the boundary layer in the diffuser is strongly three dimensional. To make the free stream follow a curved path, a pressure gradient parallel to the surface but normal to the streamline is necessary. The value of this pressure gradient is sufficient to produce the centripetal acceleration of the freestream.

$$\frac{1}{\rho}\frac{\partial P}{\partial n} = \frac{V^2}{R} \qquad \text{Eq. 2-1}$$

where *R* is the radius of curvature of freestream, *n* is the normal direction with respect to the has lower velocity with respect to the center of the flow; this implies that the radius of curvature in the boundary layer is smaller than the center and the boundary layer assumes a strong three dimensional shape.

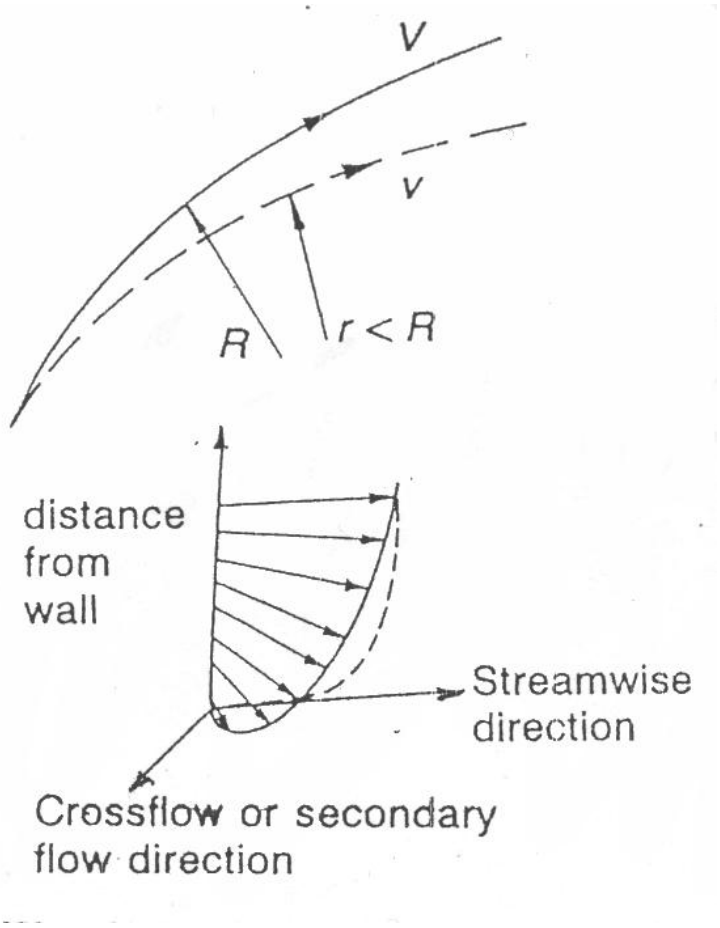

Figure 2-1. Path of the fluid particle and boundary layer in a vaneless diffuser.

Several authors link the onset of the rotating stall with the reverse flow. Conversely, Abdelhamid et al. [8] claimed that pressure oscillations extend into the whole diffuser and that they are not only due to the rotating zones of boundary layer separation. Further studies by Abdelhamid [9] [10] assessed that rotating stall can occur also in absence of reverse flow and that a stable flow condition can coexist with reverse flow zones in the diffuser.

Nowadays, it is not yet completely clear the mechanism of the onset of the stall, but the theory of the reverse flow as necessary condition seems to be the most widely used.

2.3 Literature correlations

Rotating stall in vaneless diffuser has been investigated by Jansen [11] (1964) from both a numerical and experimental point of view. Jansen was the first to demonstrate that the phenomenon can be originated by a local inversion of the radial velocity component in the vaneless diffuser.

The theoretical approach is based on the continuity and momentum equations in the radial and tangential directions in case of unsteady, inviscid and incompressible flow. Starting from the assumption that the unsteady flow field is composed by a steady free vortex on which an unsteady perturbation is superposed, Jansen obtained the linear form of governing equations. The simplest solution of this equation gives the perturbation as a periodic wave:

$$\phi = \psi(r) \cdot e^{i(\sigma \cdot t - \lambda \vartheta)} \qquad \text{Eq. 2-2}$$

where the real part of $i\sigma$ is the logarithmic decrement of the amplitude and the imaginary part is its angular velocity ω_σ. The number of stalled cells is λ and ψ(r) is the amplitude as a function of the radius.

For large values of α (near tangential flow), Jansen proposed a uniform atmospheric pressure at the diffuser outlet as a boundary condition:

$$\frac{\partial \hat{p}}{\partial \vartheta} = 0 \qquad \text{and} \qquad \frac{\partial \hat{p}}{\partial r} = 0 \qquad \text{Eq. 2-3}$$

where $\hat{p}$ is the pressure perturbation.

If one assumed two stalled cells (a typical case), the solution for $i\sigma$ is the following:

$$i\sigma = i\left[1 - A\cot\alpha + iB\cot\alpha\right]\frac{2\omega}{r_5^2} \qquad \text{Eq. 2-4}$$

The perturbation increases if the real part of $i\sigma$ is positive and decreases if negative. This analysis links the onset of the unsteadiness with the flow inversion in the diffuser, i.e. $\cot\alpha<0$. The rotating velocity is given, as mentioned, by the imaginary part of $i\sigma$:

$$\frac{\omega_\sigma\left(r_5/r_2\right)}{\omega\lambda}=f\left(\cot\alpha_2\right) \qquad \text{Eq. 2-5}$$

which indicates that the rotating speed ω_σ depends on the number of cells λ, radius ratio between inlet and outlet of the diffuser $\left(r_5/r_2\right)$ and diffuser inlet flow angle α_2. Basically, the main conclusions of this theory are:

- Rotating stall is caused by a local flow inversion in the diffuser;
- It can exist with uniform inlet and outlet flow;
- The rotating speed is in the range of 5-22% of ω.

Probably, perturbations start in the boundary layer, where the streamlines are curved more than the in middle diffuser passage (reverse flow), and then, once they are damped out in the midstream region, waves of limited amplitude are generated.

This destabilizing mechanism was then further confirmed by Frigne and Van den Braembussche (1985), who verified the theory with a *time-evolving* calculation of the interaction between the inviscid flow core in the center of the diffuser and the unsteady boundary layer near the wall; this self-excited oscillations lead to a local acceleration or deceleration of the core flow. Also Watcher and Rieder (1985) confirmed these results by measuring simultaneously the static pressure and the velocity variations during diffuser rotating stall and finding a phase shift of 180° between the two measurements. This indicates that the static pressure decreases when the local velocity increases due to the blockage.

The theory of Jansen leads to practical criterion to predict the return flow in the boundary layer, i.e. the determination of the instability (Figure 2-2). This calculation used an inviscid flow core in the center and three dimensional boundary layers near the walls. However, an unfortunate choice of boundary layer profiles could lead to critical conditions as the two boundary layers filled the entire channel width. The

stability conditions, as a function of α_2 and b_2/r_2, were too restrictive for narrow diffuser.

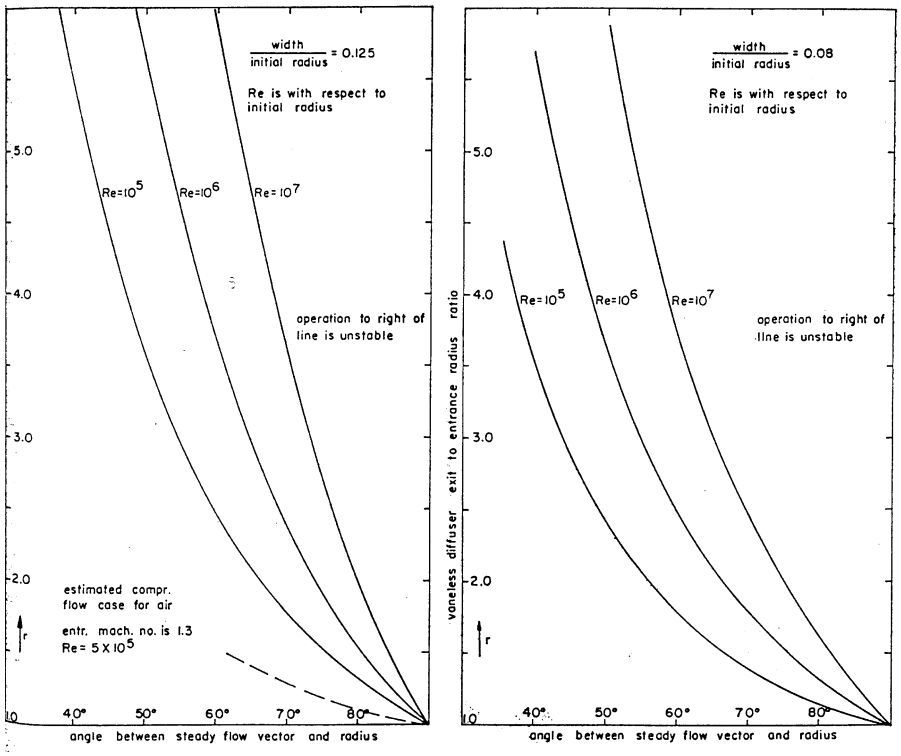

Figure 2-2. Jansen's criterion to determine the instability zone.

Senoo *et al.* (1977a) [12] repeated this calculation with the following modifications:

- The flow is no assumed to be symmetric with respect to the center of the diffuser;
- The inlet conditions take into account for the distortion both of the radial and tangential velocity field along the diffuser width;
- The boundary layer profile is modified in such a way that the contact between the two boundary layers does not lead to the flow inversion.

The results of this calculation indicate that the freestream angle α_∞ continuously decreases with radius, while the angle of the wall streamline $\alpha_{\infty+\gamma}$, first increase and

then decreases once the two boundary layers fill the entire diffuser width. As shown in Figure 2-3 the flow inversion occurs when $\alpha_{\infty+\gamma}$ is greater than 90°.

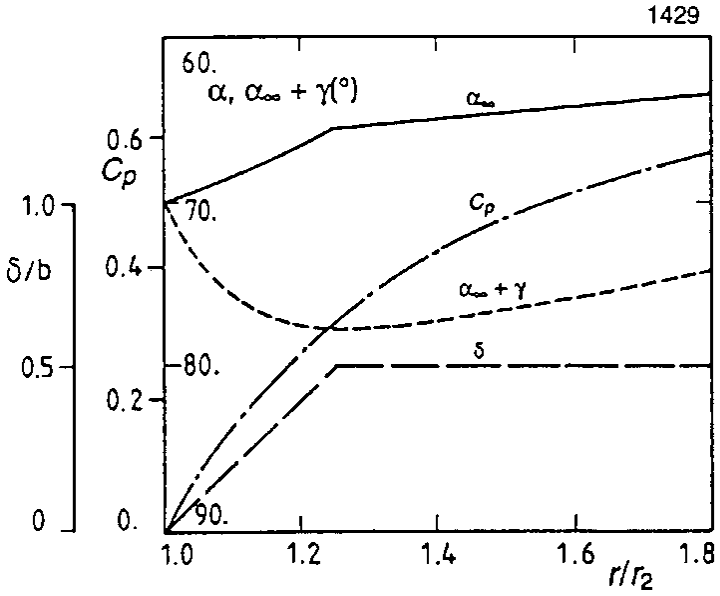

Figure 2-3. Vaneless diffuser flow.

This calculation allows one to take into account the influence of the geometric and aerodynamic parameters on the return flow in the vaneless diffuser. A critical flow angle α_{2r} at the inlet of the diffuser beyond which return flow occurs can be hence defined. In Figure 2-4 is reported the variation of α_{2r} as a function both of Reynolds number at the inlet and of b_2/r_2 for r_5/r_2=1.2.

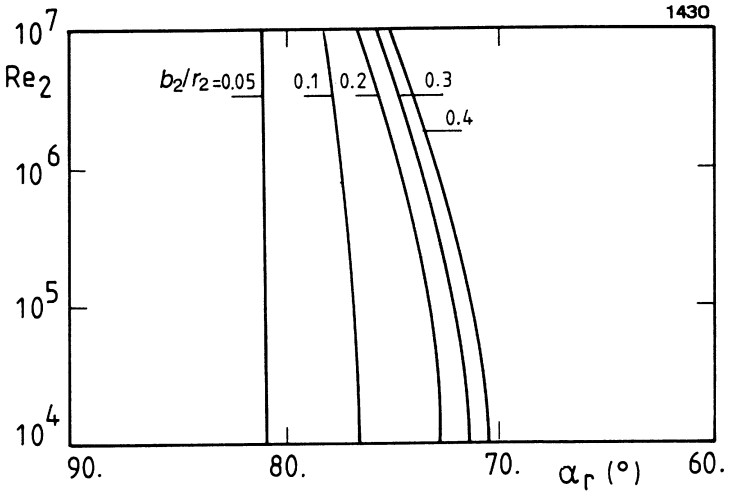

Figure 2-4. Variation of α_{2r} as a function of Reynolds number.

It is worth noticing that narrow diffusers are more stable than the wide diffusers and they are not influenced by the variation of Reynolds number. On the other hand, wide diffusers are more stable for high Reynolds number. In Figure 2-5 is shown the variation of α_{2r} as a function both of inlet Mach number and of b_2/r_2 for r_5/r_2=1.2 and $r_5/r_2 \to \infty$. One can readily notice that α_{2r} decreases with increasing of Mach number for both narrow and wide diffusers and as it is independent of diffuser length for narrow diffusers, it strongly depends on it for wide diffusers.

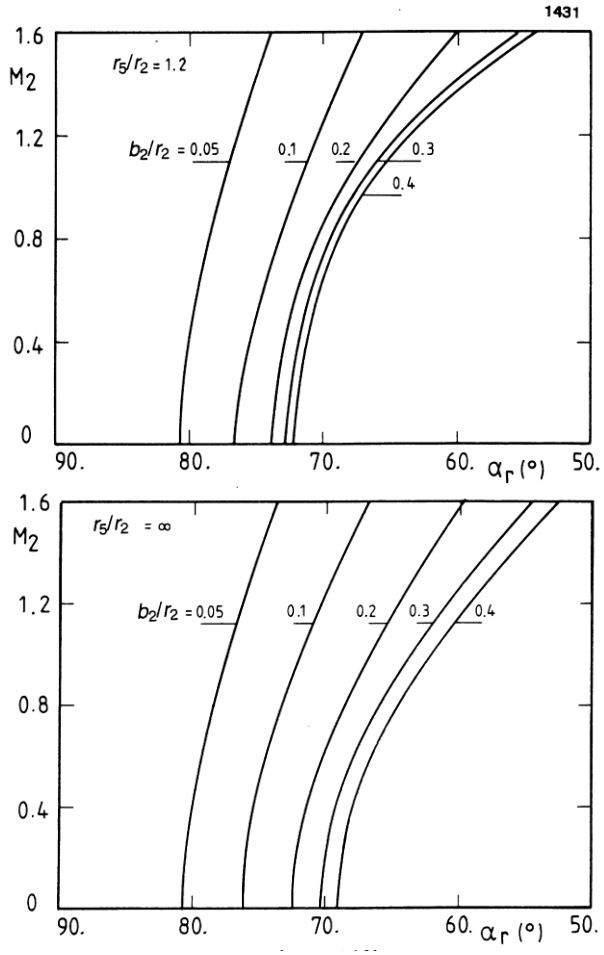

Figure 2-5. Variation of α_{2r} as a function of inlet Much number and b_2/r_2 for r_5/r_2=1.2 and $r_5/r_2 \rightarrow \infty$.

Furthermore, it was evaluated by Senoo *et al.* (1977b) [13] the influence of inlet distortion on diffuser stability for an infinitely long diffuser (Figure 2-6). While the distortion on the radial velocity has a strong influence on both the narrow and the wide diffuser, the distortion on the tangential one has a small influence, especially for narrow diffusers. However, it is worth to remark that the estimation of the velocity distortion at the inlet is difficult.

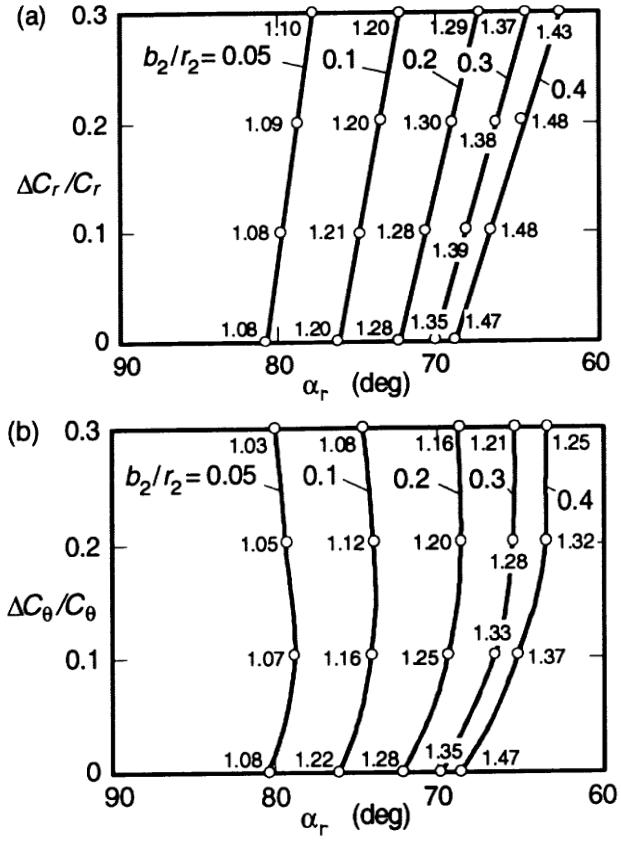

Figure 2-6. Influence of the flow distortion at the inlet on return flow for infinitely long diffusers.

By taking into account the incompressible flow with a uniform velocity distribution at the inlet, the influence of b_2/r_2 and r_5/r_2 on the inception of return flow can be highlighted in Figure 2-7. For each b_2/r_2 value it is possible to estimate a critical flow angle, α_{2r}, for which a vertical line can be determined. For flow angle values higher than this limit, return flow occurs. The dashed line allows to determine the extension of the reverse flow with the variation of the b_2/r_2 ratio and the inlet flow angle.

It is worth noticing that for narrow diffusers, the reverse flow starts close to the diffuser inlet but disappears after a short period. For wide diffusers, the reverse flow starts at higher radius than narrow ones and if the radius ratio is small enough, no return flow will be observed. Senoo *et al.* (1978) [14], basing on experimental data,

showed that the rotating stall occurs when the inlet flow angle exceeds α_{2c} in agreement with the following rule:

$$\frac{(90° - \alpha_{2c})}{(90° - \alpha_{2r})} = 0.88 \qquad \text{Eq. 2-6}$$

where α_{2r} is the angle previous defined and α_{2c} is the diffuser critical inlet flow angle.

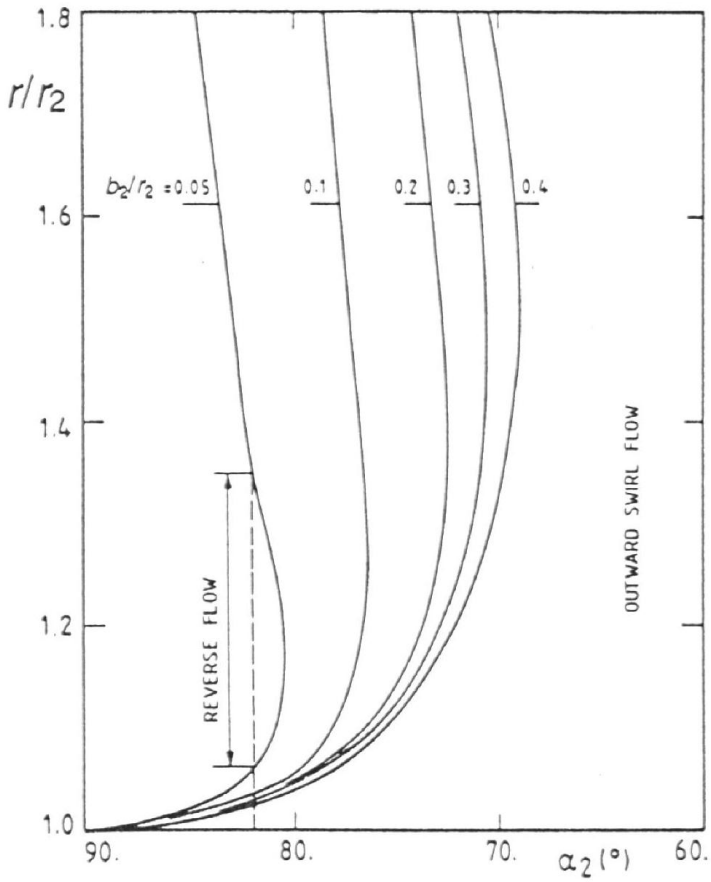

Figure 2-7. Influence of diffuser width on return flow.

The problems start in comparing the theoretical results with the experimental ones.

First, one must be able to distinguish if the measured unsteadiness consists in a rotating stall of a vaneless diffuser or of an impeller. A significant difference is that

the rotating stall in vaneless diffusers usually occurs on the negative slope side of the compressor pressure rise curve.

A second problem appears when the evaluation of the average diffuser inlet flow angle is needed. Generally, this parameter is not directly measurable in an unsteady (non-uniform) flow; however, it can be evaluated by using a slip factor correlation (Wiesner, 1967) or by measuring the temperature rise by the impeller. Only in a few cases the flow angle is calculated by mass averaging measured values.

By analyzing the collected experimental data, some remarks can be done:

- Low Reynolds number (10^3) can have negative influence on the stability also in case of narrow diffusers. Low Reynolds number lead to flow inlet distortion that can affect the stability; this occurs also in case of higher loading of the impellers.
- The zone between the impeller outlet and the diffuser inlet can affect the stability limit, especially for narrow diffusers in which the critical region is located at the diffuser inlet.
- The presence of vanes at the diffuser outlet or in the return channel can have favorable or unfavorable effects.
- For wide diffusers, a decreasing if the radius ratio has a good influence on the stability.
- The Mach number has a negligible influence on the diffuser stability, as predicted by the calculation.

In conclusion, it is possible to claim that the theoretical curves allow one to correctly predict the critical inlet flow angle only if the limitations of the calculations are respected (even if it is not always possible to know a priori the flow inlet distortions). Discrepancies between measured and predicted critical angle are often due to the discontinuity between the impeller outlet and the diffuser inlet width. Senoo's formulation did not take into account this variation [15].

This problem was experimentally solved by Nishida *et al.* (1988, 1991) [16] [17] and Kobayashi *et al.* (1990) [18].

They studied the influence of the *pinch* and the ratio b_3/b_2 (diffuser width and impeller exit width) on the diffuser stability by testing three different impellers with six different diffusers mounted as reported in Figure 2-8. It is worth noticing that the

stage was constituted by an inlet, a two-dimensional impeller, a vaneless diffuser and a return channel.

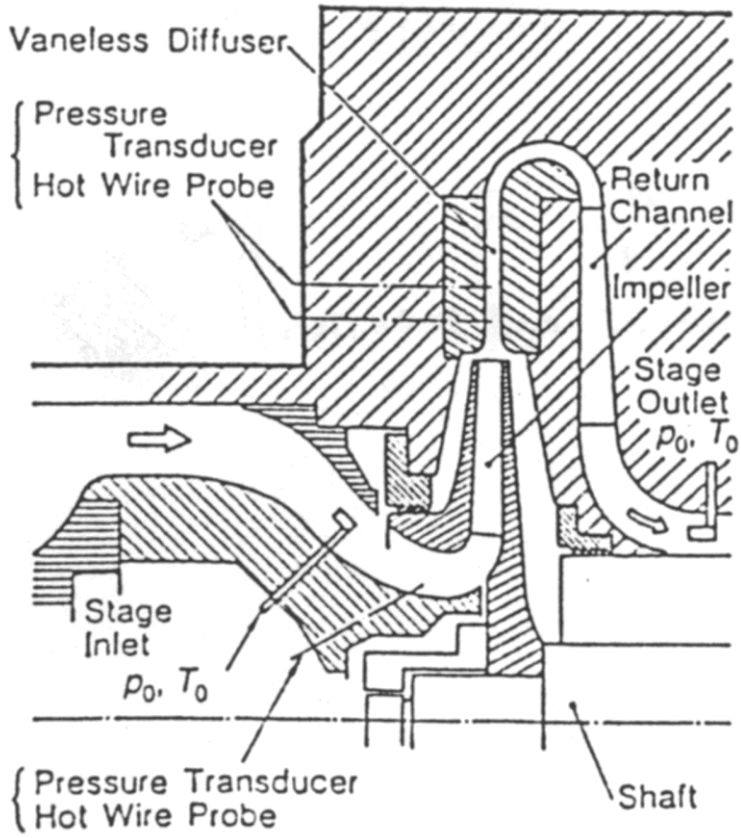

Figure 2-8. Cross section of the test compressor.

The effect of the diffuser width on the onset of rotating stall is presented in Figure 2-9. In all cases, as the diffuser increases its width, the onset of the stall occurred earlier, while the performances remained the same.

Furthermore, it was note that as the flow angle increases, both the head and the rotating speed ratio of the stall cell increase. The stall cell number for impeller A was 1-2 and for impeller B was 3-4.

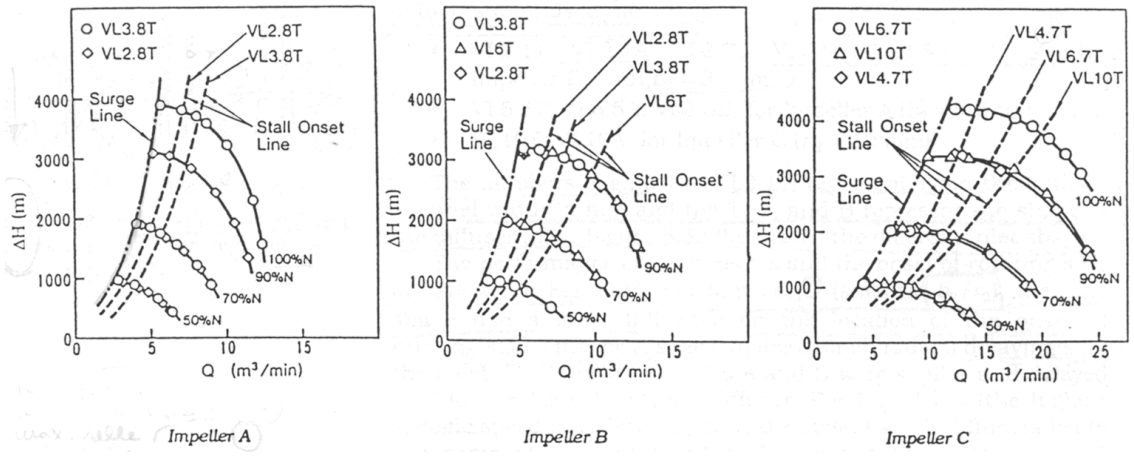

Figure 2-9. Effect of the diffuser width on the performance curve.

The results of this study were then compared with the Senoo method to predict the stall onset (Figure 2-10); one can readily notice that as the ratio b_3/b_2 decreases, the critical angle in which the stall starts is much smaller than that one predicted by Senoo. Moreover, a good agreement with Senoo's prediction is observed only in case the ratio b_3/b_2 is equal to 1. This led to the conclusion that the ratio b_3/b_2 influences the value of the critical stall angle and it must be considered in the calculation.

From these results the authors extrapolated the following correlation to predict the critical angle starting from that one predicted by Senoo and introducing the ratio b_3/b_2.

$$(90° - \alpha_{crit}) = (90° - \alpha_{crit,.Senoo}) + \left(14.1 - 143.4 \cdot \frac{b_3}{r_2}\right) \cdot \left(1 - \frac{b_3}{b_2}\right) \qquad \text{Eq. 2-7}$$

This means that if one reduces the diffuser width obtains the onset of the stall for lower values of flow rate.

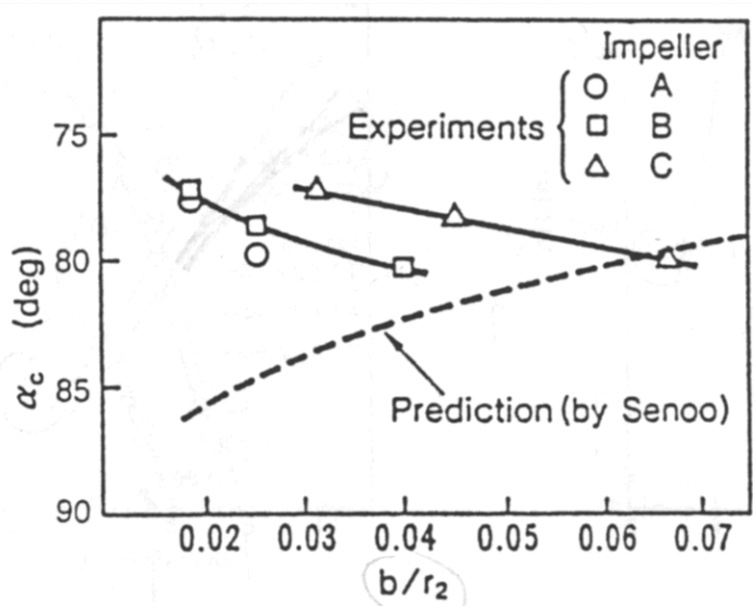

Figure 2-10. Experimental and calculated values of the critical angle.

In the following study, Kobayashi *et al.* (1990) [18] modified the previous correlation by considering further experimental results.

The authors tested again the impeller A and B and added another D with a lower ratio b_2/r_2. They tested several vaneless diffusers with different width and different *pinch* as shown in Figure 2-11.

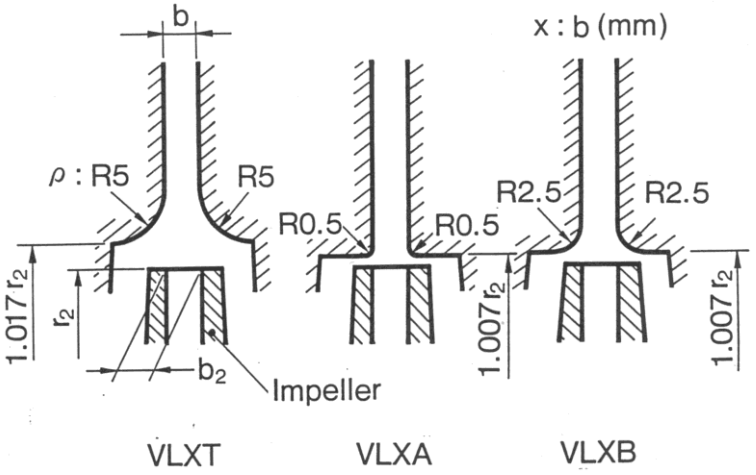

Figure 2-11. Scheme of the tested *pinch*.

The results showed a good agreement with the previous study. In particular, if the variation of the diffuser width did not affect the performance curve, the onset of the stall moved to lower flow rate by decreasing the diffuser width. Moreover, for large diffusers, the pinch shape had no great influence on the onset of the stall.

The experimental data were again compared with the Senoo prediction (Figure 2-12); once again it is possible to note that a good agreement was found only for the case with $b_3/b_2=1$.

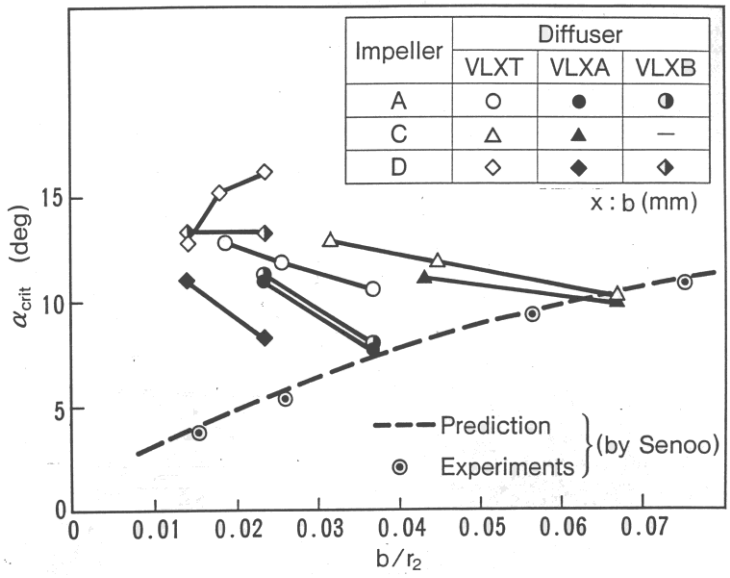

Figure 2-12. Experimental and calculated values of the critical angle as a function of the ratio b_3/r_2.

In order to explain these results, the authors proposed that the decreasing of the diffuser width induced a reduction of the radius at which the return flow occurs. This implies an increasing of the reverse flow zone in the diffuser and the possibility that the stall onset occurs before.

The shape of the pinch had not influence on the prediction of the critical stall angle (with respect the Senoo prediction) when the ratio b_3/b_2 is equal to 1. This aspect seemed to have influence only in case of high b_2/r_2.

The authors highlighted that some configurations presented an anomalous behavior in term of critical flow angle. They analyzed the difference between the measured and the predicted (by Senoo) critical flow angle as a function of $\Delta r/r_2$ where

Δr represents the difference between the radius of the onset of the reverse flow and the parallel walls of the diffuser.

The analysis pointed out that the Senoo's correlation shows a good agreement with the experimental results only in case of $\Delta r/r_2>0.1$.

After these considerations the authors decided to discard the curves with anomalous behavior and modified the previous correlation:

$$(90° - \alpha_{crit}) = (90° - \alpha_{crit,\,Senoo}) + \left(17.02 - 74.2 \cdot \frac{b_2}{r_2}\right) \cdot \left(1 - \frac{b_3}{b_2}\right) \text{ with } \frac{\Delta r}{r_2} > 0.1 \qquad \text{Eq. 2-8}$$

where α_{crit} is the inlet flow angle (at the radius with parallel walls) and $\alpha_{crit,Senoo}$ is the predicted critical angle by Senoo.

A validity limit on $\Delta r/r_2$ corresponds to a limit on the ratio b_2/r_2 at which the correlation can be applied. It is worth noticing that lower is the b_2/r_2, lower is the radius of the reverse flow.

The previous correlation can be re-written in the following form:

$$(90° - \alpha_{crit}) = 37.5\sqrt{\frac{b_2}{r_2}} + \left(17.02 - 74.2 \cdot \frac{b_2}{r_2}\right) \cdot \left(1 - \frac{b_3}{r_2}\right) \text{ with } \frac{\Delta r}{r_2} > 0.1 \qquad \text{Eq. 2-9}$$

This correlation is commonly named as "modified Kobayashi".

The main problem of these correlations is that the *pinch* geometry is not included in the calculation of the critical angle.

As final considerations, the authors analyzed the possible solutions to prevent the rotating stall in vaneless diffusers and they highlighted three different methods:

- Reducing the width of the vaneless diffuser;
- Removing the vaneless diffuser;
- Using a low solidity vaned diffuser [19].

2.4 Current methodologies to study the rotating stall

In the previous section the main characteristics of the rotating stall in vaneless diffuser have been presented. As aforementioned, the first studies on this field were

devoted in understanding the physics of the phenomenon and giving some instruments to predict the onset of the stall and they represent the bases of the current methodologies. In particular, several efforts were made in developing a correlation able to predict the critical angle in which the stall inception occurs.

After these works several studies have been carried out over the years to understand the characteristics, the causes and the effects of the unsteady phenomena developing in different types of centrifugal compressors. These studies that will be presented later on this chapter represent the recent state of art; the authors developed both experimental and numerical approaches to investigate the rotating stall starting from the considerations presented before.

2.4.1 Experimental approaches

The majority of the studies carried out in the last few years made use, however, of purposefully developed experimental layouts and advanced measurement systems.

In particular, the use of dynamic pressure probes located at different sections and radii of the diffuser represents one of the investigation methodology widely used in analyzing the vaneless diffusers rotating stall [20] [8] [21] [22].

Ferrara et al. [23] [24] [25] [26] carried out many experimental tests by means of this technique to investigate the influence on stall behavior of different geometrical configurations. The stage was constituted by a backward channel upstream, a two-dimensional impeller, a vaneless diffuser and a constant cross-section volute downstream.

By analyzing signals from dynamic pressure sensors of each section, it was possible to carry out an accurate study of stall typology. For a complete analysis of the phenomenon, and to obtain as much information as possible, the signals were analyzed both in time and frequency domain.

The authors proposed an analysis of the signals of the dynamic pressure sensors in which the circuit throttle valve was slowly closed with continuity from the overflow to the surge (Figure 2-13).

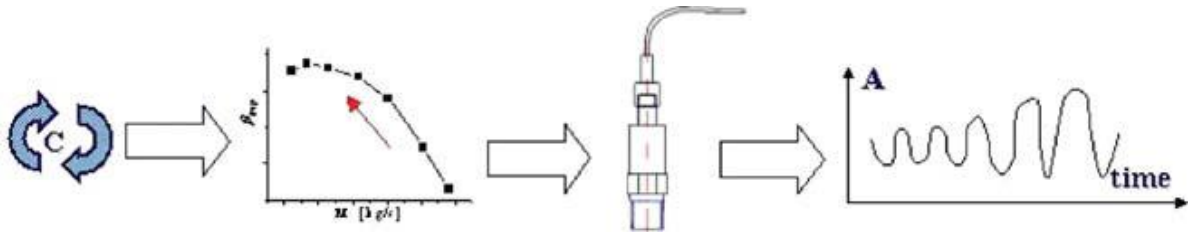

Figure 2-13. Scheme of the streaming procedure.

The proposed approach allowed one to determine the stall inception flow coefficient during the closing of the throttle valve but provide good results only if the assumption that the stall has a rigid behavior is considered. When sub-synchronous pressure fluctuation amplitudes were comparable with synchronous values (due to the blade passing), the condition was considered as stall inception point. Normally, when rotating stall appears, several sub-synchronous frequencies are present: the lowest one represents the fundamental frequency (called stall frequency) while the others are usually multiple of this fundamental component. By applying this technique to all the dynamic pressure sensors (i.e. by comparing the signals at the same section), the authors developed a formulation to estimate the number of lobes:

$$Lobes'\,Number = \frac{\Delta\varphi}{\Delta\vartheta} \qquad \text{Eq. 2-10}$$

where $\Delta\varphi$ is the phase shift between sensors signal and $\Delta\vartheta$ is their geometrical angular distance.

Other experimental methodologies can be found in literature. In particular, recent studies present advanced measurement systems to investigate the unsteady phenomena that occur in vaneless diffusers of centrifugal compressors [27] [28] [29].

In these works, the authors focused on the unsteady phenomena not connected with blade passing frequency. Dazin *et al.* [27] [28] carried out experimental investigation in which the aim was to catch the space-temporal evolution of the phenomenon using a measurement technique resolved both in time and space. To reach this goal, they obtained interesting experimental results by means of high repetition rate PIV coupled with unsteady pressure transducers. By doing so, the

technique allowed one to explore the three-dimensional behavior of the phenomenon as three components PIV maps obtained at three different heights within the diffuser.

In order to characterize and confirm the rotating nature of the unsteady phenomenon a spectral analysis was applied to the signals. Then, a dedicated phase-averaging applied on the PIV flow fields allowed to identify a three cell rotating structure (Figure 2-14). Furthermore, the analysis showed the possibility of having a blockage near the entrance of the diffuser on the hub side.

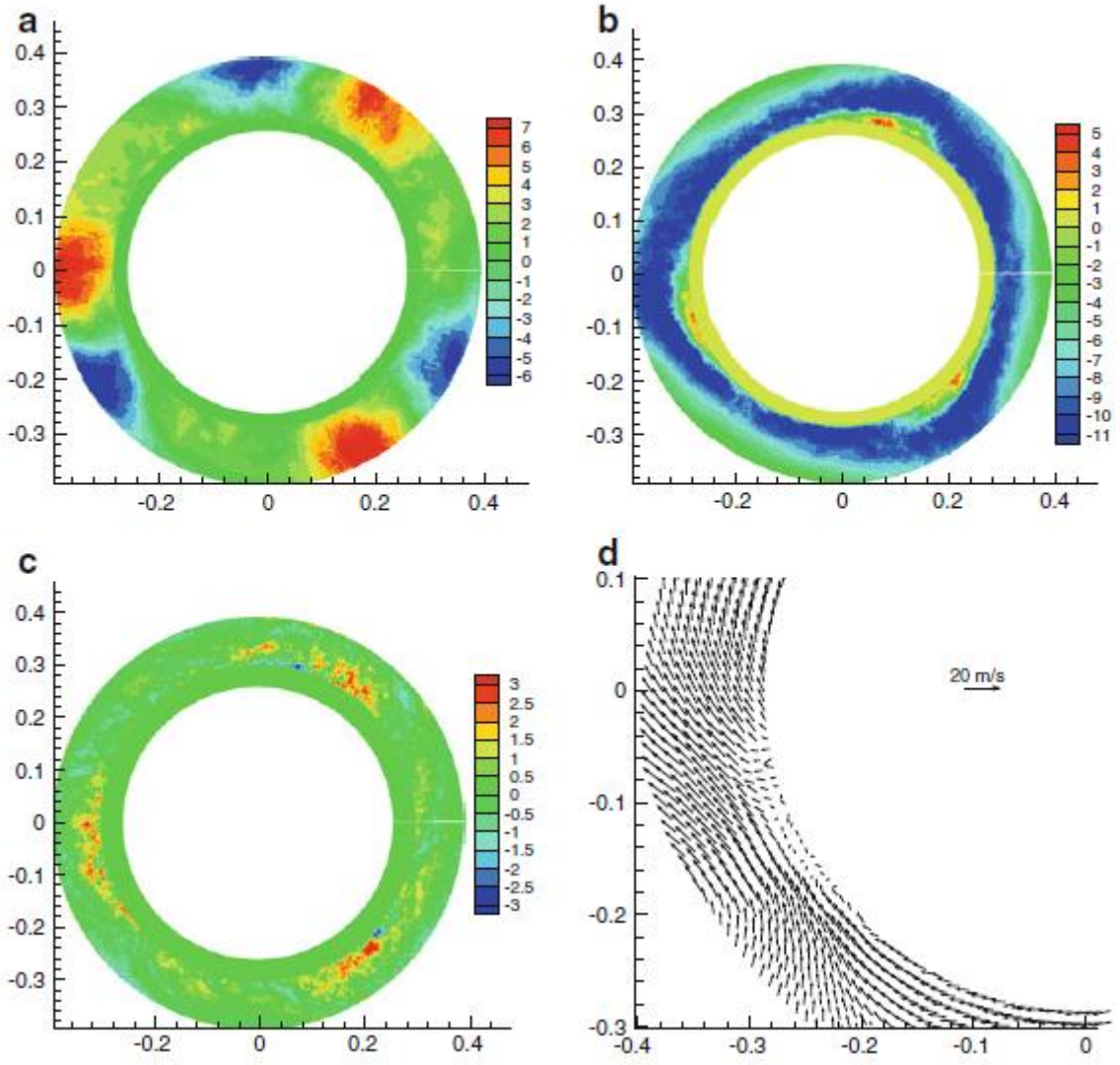

Figure 2-14. Three cell rotating structure in the diffuser (Dazin *et al.)*.

Towards the outlet of the diffuser, the authors highlighted a homogenization of the previous developed cores of inward and outward radial velocity along the diffuser. They demonstrated that this development determined the decreasing of the diffuser performance.

Toni *et al.* [29] carried out phase-resolved measurements during the unsteady functioning of a single stage centrifugal compressor using a cylindrical single sensor fast response aerodynamic pressure probe (FRAPP) traversing and rotating from the impeller hub up to the shroud.

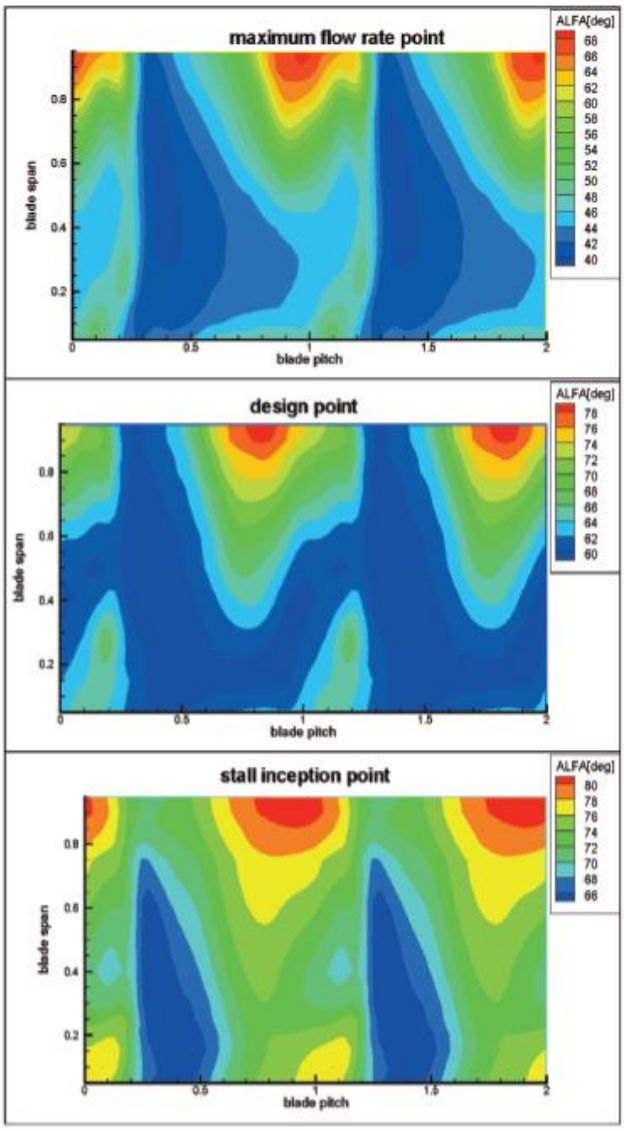

Figure 2-15. Blade-to-blade flow angle (Toni *et al.*).

These measurements allowed one to reconstruct the unsteady flow field of total and static pressure and flow angle with a higher precision than that one obtained with a common five-hole probe. FRAPP measurements showed flow phenomena in agreement with the concepts found in literature in term of vortex structures (Figure 2-15). Moreover, it is worth to remark that this technique does not need optical access to be performed while for optical techniques is necessary. FRAPP measurements provide useful and detailed information on the flow field and would allow one to improve the efficiency of the component during the design process. However, currently this sensor represents a measurement technique with a certain level of complexity that especially requires a high level of miniaturization of the device in order to not affect the measure.

2.4.2 Numerical approaches

In literature, two typologies of analytical models for rotating stall in vaneless diffusers can be individuated.

The first one uses momentum integral equation of boundary layer and links the unsteadiness due to the rotating stall to the existence of radially inward flow within boundary layers as previous described [11] [12]. However, several subsequent studies pointed out that it is also possible to have rotating stall without reversed flow or have reversed flow without flow instabilities [14] [8].

The second method to study the stall combines the above by analyzing the instability of inviscid core flow or the interaction core with the boundaries [30] [31]. Dou and Mizuki [32] and Abdelhamid and Bertrand [9] concluded in their studies that the stall mechanism were different for narrow diffuser and wide diffuser.

As shown in Figure 2-16, the stall seems to have two different mechanism of inception: narrow diffusers shows a strong influence of the walls in the evolution of the boundary layers while for wide diffusers are assumed to have two-dimensional core flow, which separates the wall boundary layers from each other.

Taking into account these considerations, Tsujimoto *et al.* [31] performed a two-dimensional flow inviscid analysis subjected to the boundary conditions of vanishing fluctuation at the diffuser inlet and vanishing pressure fluctuation at the diffuser outlet. By doing so, they obtained the onset conditions and the disturbance field in

agreement with experimental results. Moreover, they concluded that upstream impeller had no influence on rotating stall.

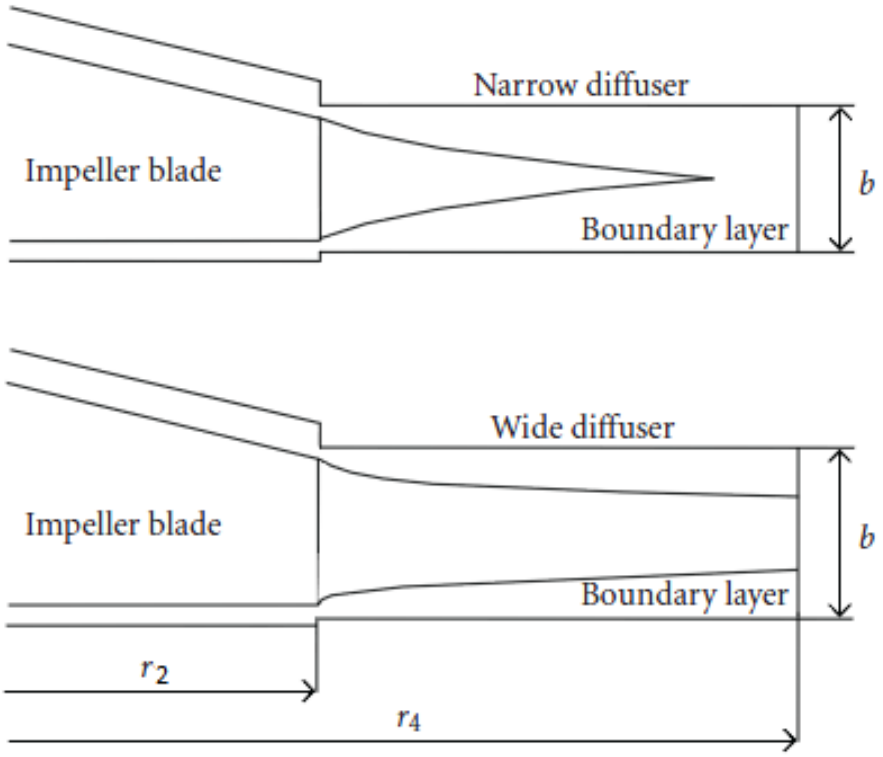

Figure 2-16. Scheme of the flow in narrow and wide diffusers.

Gao *et al.* [33] used a Wave Neural Network (WNN) to study geometry factors on stall inception of vaneless diffusers. Their research was carried out by collecting measured data from literature; once WNN was trained, each input parameter was varied while others were kept constant to study the influence of the variable on critical angle and cell speed at the stall inception. They mainly concluded that the stall has two different mechanism of inception depending on the diffuser width. Moreover, the authors investigated the effects of changing the impeller blade number, the impeller speed and the diffuser ratio. By summarizing, each parameter investigated has a different influence on the critical angle if the analysis is performed on wide or narrow diffusers.

Due to the difficulties of experimental analyses another investigation approach is represented by Computational Fluid Dynamic (CFD) which is thought to be a key

technology to improve the knowledge of the pressure field inside the compressor during unstable operation.

Generally, CFD could represent a useful tool for turbomachinery designer mainly thanks to the increase in computational power and resource. Conversely, some problems can hamper the application of computational fluid dynamics, especially concerning the enormous amount of data to be stored in fully unsteady simulations of an entire machine; for this reason, traditional CFD studies are very often focused on specific parts of the machine or scaled geometries.

Starting from the previous assumption on the possibility to have two different stall inception mechanisms (wide and narrow diffusers), Ljevar *et al.* [34] [35] [36] [37] [38] proposed in their studies an uncommon and simplified CFD analysis.

They focused their analyses only to the wide vaneless diffusers with parallel diffuser walls in which they assumed that the core flow between the diffuser plates has mainly a two-dimensional nature. They led the instability analysis by performing a two-dimensional CFD model of the vaneless diffuser core flow (Figure 2-17). In particular, the authors used an incompressible and laminar flow model in which the influence of the wall boundary layers is not taken into account. Since the turbulence models capture the diffusion-like character of turbulent mixing associated with many small eddy structures, laminar viscous model was chosen for this analysis.

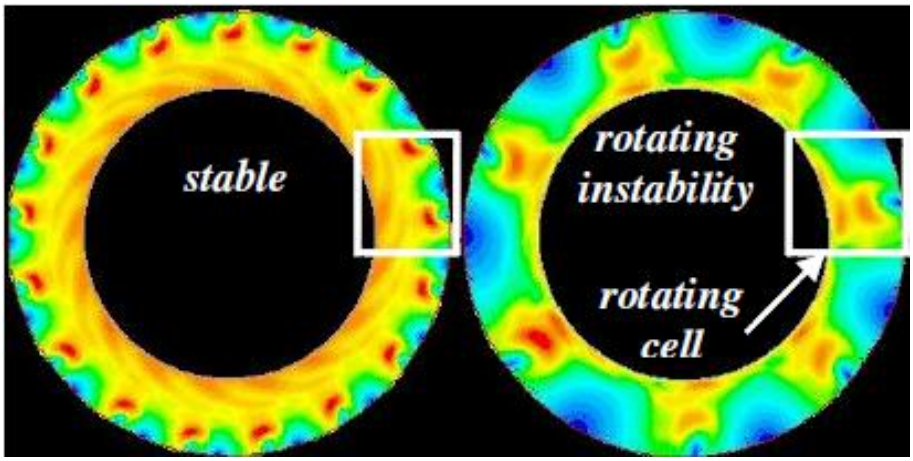

Figure 2-17. Two-dimensional vaneless diffuser core flow model.

The model allowed one to obtain the rotating instability by using a water model of the wide vaneless diffusers properly scaled by an existing air compressor. As previous reported, several studies were devoted by the authors to investigate the influence of the diffuser geometry, the diffuser radius ratio, the number of impeller blade and the shape and the intensity of the jet-and-wake at the diffuser inlet.

By imposing the inlet conditions, the interaction with the impeller was not taken into account in this model in agreement with Tsujimoto *et al.* [31] but in disagreement with Abdelhamid [10] who showed that stall pattern depends on the coupled effect both of impeller and diffuser. It is worth to note that this analysis did not explain the flow mechanism of rotating stall, but it highlighted the physical phenomena that could contribute to the stall inception in wide centrifugal compressor diffusers.

As aforementioned, the work presented by Ljevar *et al.* represents an uncommon and simplified CFD two-dimensional model and it does not require high computational performance (the calculation domain has limited dimensions). However, several levels of CFD analysis with increasing complexity exist in open literature; as they were usually carried out to predict the performance and operating range [39] [40], only few works focused the attention on the unsteady phenomena before the surge by including in the domain the whole stage [41] [42].

Sorokes *et al.* [42] proposed an interesting work in which an unsteady CFD analysis was performed on the full 360° model in order to highlight both the difference in the flow structure with respect to the steady CFD performed on a sector model and the mechanism of stall inception in terms of lobes' number and pressure pattern along the whole machine. Due to the size of the domain of the full 360° geometry (see Figure 2-18), it was computationally impractical to conserve the grid density of the steady state CFD analysis performed on the sector model, but, however, this kind of simulation required a huge amount of elements (about 52 millions) and consequently a lot of computational resource.

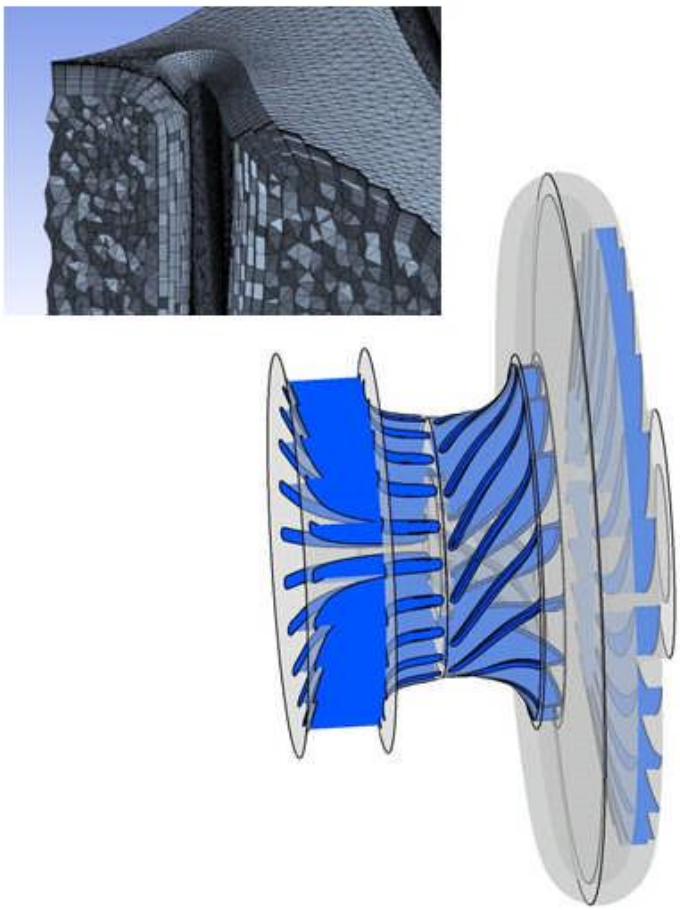

Figure 2-18. Computational domain of the full 360° geometry.

The unsteady analysis highlighted that, as the flow rate was reduced to reach the zone where the unsteady phenomena take place, a low momentum zone along the shroud wall of the diffuser extended from the inlet to the outlet of the diffuser appeared. Furthermore, they claimed that the stall cells formed near the shroud wall of the diffuser where the radial velocity was close to zero and that the impeller influenced the formation of these stall cells (Figure 2-19).

The authors also observed the propagation of the two stall cells detected in the diffuser into the return channel. The stall cells rotated clockwise, but the method to calculate the rotation frequency did not fully clarify how they calculated 1.8 Hz; in addition this value seems to be very low with respect to that one expected from the experimental results and also to what is reported in literature.

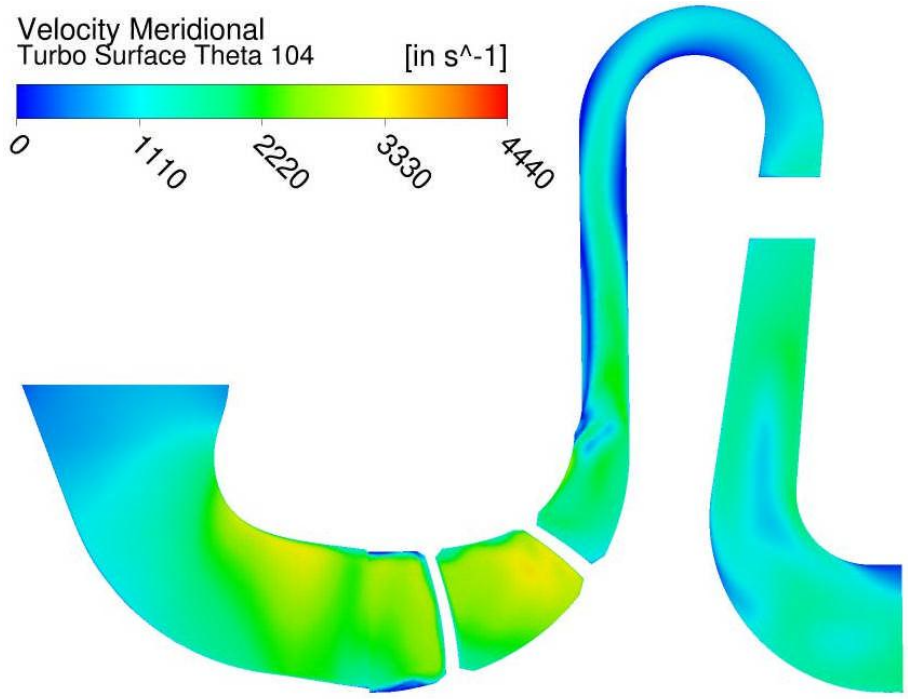

Figure 2-19. Meridional velocity contour in unsteady conditions.

2.5 Objectives of the work

All these approaches did not completely clarify the aspects related with the stall onset and in general with the stall mechanism: disagreements and contradictions still exist towards how many factors and which factors should be taken into account to correctly predict the critical angle and the unsteady stall pattern; moreover, these methodologies are validated under specific assumptions which does not allow one to give to the approach a general validity.

As shown, published literature and ongoing researchers focused their efforts in developing methodologies of investigation and prediction, but one of the most widely used in the industrial world remain the Senoo and Kobayashi correlations.

If on one hand the advanced techniques showed before represent the only way for an effective development of the knowledge in this field, on the other hand their direct and spread application to the industrial world is definitely difficult in many cases, due to either complexity or cost reasons. As a consequence, the industrial world generally

prefers to approach the study of the left margin of the operating curves by means of a limited number of dynamic pressure probes, which represent a consolidated technology, with limited cost and quite easily integrable with a conventional test set-up [25].

In general, these sensors are only exploited to detect the stall onset and evaluate the intensity of the subsynchronous pressure pulsation, e.g. to define a stall margin if compared to a limit value. In only few cases [25], the analysis has been extended to a spatial analysis of the induced pressure field, particularly focusing on the lobes' number.

In order to definitely characterize the vaneless diffuser rotating stall, GE Oil & Gas started a collaboration with the Department of Industrial Engineering of the University of Florence. Starting from the huge amount of data collected during several years of tests by the industrial partner, a systematic procedure to analyze the rotating stall that occurred on their machine was first developed.

The procedure used the dynamic pressure measurements and it allowed one to acquire several information on the stall characteristics in terms of stall frequency, number of lobes and stall pressure amplitude by transposing pressure measurements into spatial pressure distribution. The available data consisted of experimental data coming from 15 different stages tested in different conditions of peripheral Mach number, working pressure and configuration. This extensive investigation allowed one to have a general viewpoint of the vaneless rotating stall: within this context, the main guidelines of the procedure are presented and discussed, with particular reference to signals analysis and manipulation as well as sensors positioning.

Moreover, the prospects of a real-time analysis made by using a higher number of sensors is analyzed and compared to the standard solution using a limited probes number.

Under proper assumptions that will be discussed later on in this work, the developed approach allowed also to reconstruct the stall pattern in term of pressure field induced by the rotating stall in the vaneless diffuser. During the stall, the unbalancing of the pressure field generates a rotating force which rotates at the stall frequency (i.e. at a subsynchronous frequency) and which acts directly on the rotor shaft by inducing severe vibrations.

As shown before, even if there were not given exhaustive and univocal explanations, several works have been devoted at investigating the physics of the phenomenon, the influence of the main design parameters and the prediction of the stall inception; only few, however, focused on the prediction of the aerodynamic force related to the rotating stall [25] [3] [43] [44] [45] [46] and their effects on the compressor behavior.

With this goal in mind, a rotordynamic model of the test rig was hence performed in order to investigate on the effects of the rotating force: an accurate estimation of the resultant of the pressure distortion during the stall could in fact provide a valuable contribution to both the identification of the actual operating conditions and the enhancement of the compressor operating range by a suitable choice of the control strategy and the bearings' characteristics.

After the rotating force has been also characterized in the model test configuration, the further purpose of this research work was to predict the rotordynamic behavior during the rotating stall of a real machine operating in on-site conditions. To reach this goal, a criterion to scale the rotating force from model test conditions to real operating conditions was developed and then applied to some multistage compressors tested in a dedicated test rig of *GE Oil & Gas*.

Moving from these results, rotordynamic analyses have been carried out on different case studies to assess the final impact of these aerodynamic excitations and to find out possible ways to mitigate them by means of proper journal bearings.

3. Stall investigation: approach/methodology

3.1 Introduction

In this chapter a systematic procedure to analyze the vaneless diffuser rotating stall will be described. As aforementioned, since this work was performed in collaboration with *GE Oil & Gas*, the post processing procedure was applied to the measurements obtained with dynamic pressure probes located at different sections of the diffuser: this kind of sensors represents a consolidated technology in the industrial field, thanks in particular to the limited cost and to the possibility to be integrated with a conventional set-up.

Before entering in the description of the advanced analysis procedure developed in this work, some considerations based on the author and the industrial's experience in the stall investigation field can be done. In particular, some details of this measurement technique will be presented to give an overview on the potentiality of this approach.

3.2 Time or space domain?

Dynamic pressure probes can be used to measure the total unbalance generated on the diffuser; nevertheless in order to define the stall shape in term of pressure pattern, a reconstruction of the pressure distribution must be provided.

This measurement typology allows one to use two different theoretical approaches which benefits and drawbacks will be discussed later on this section.

The first approach consists in a "real-time" analysis of the evolution of the unsteady phenomenon in the diffuser: a proper number of "snapshots" of the pressure field, acquired simultaneously in a sufficient number of points at different diffuser sections is needed. Since this "real-time" analysis would provide the real signal in each frame of the analysis, the highest degree of accuracy by using dynamic pressure probes would be guaranteed. Conversely, if one requires a good spatial resolution, a significant number of probes is necessary. Moreover, if the pressure pattern is not well defined due to a noisy signal, the pressure reconstruction could be affected by a systematic error which can lead the analysis to a wrong result.

Generally, this "time-domain" approach represents a difficult solution in term of management of a high number of sensors; furthermore, in the industrial field, it become more difficult due to the mechanical and cost issues connected the high number of probes and the relative access to be provided in the case of each machine should be tested in this condition.

As a consequence, the most common choice in industrial application is to make use of a limited number of dynamic pressure probes (at least two sensors), flush mounted angularly in different diffuser section of particular interest (e.g. the diffuser inlet and outlet).

This second approach consists in a signal acquisition of probes that referred always to the same spatial position in the space; one can readily notice that an accurate post processing of the data is required to shift between the two domain (i.e. from the time into the space domain) and to reconstruct the pressure path (i.e. the shape and the number of lobes). Usually, in the common practice, the time signals are manipulated by means of an ensemble average approach locked at the frequency of the phenomenon which is studied (i.e. the rotating stall frequency).

The difficult related to this type of approach is placed in the use of only few sensors: this implies some important precautions in correctly manipulating experimental data. One of the most crucial points is the identification of the correct frequency of the phenomenon which should be applied to the averaging process to reconstruct the stall pattern.

As will be presented in the following section together with several examples, the second approach was used and improved during this work. However, since it was considered an interesting methodology (especially in the research field), the "real-time" approach will be analyzed and discussed later on in this study from a theoretical point of view.

3.3 Background of stall characterization

In open literature, one can easily found that the vaneless diffuser rotating stall consists of a pressure fluctuation which rotates at a subsynchronous frequency in the range between 10-40% [2] [7] [47]. Other authors preferred to restrict this range between 20-40%.

By an internal convention, it can be assumed that the machine is in stall condition when the fluctuation due to the rotating stall becomes the highest component of the signal, even higher than the Blade Passing Frequency (BPF). Moreover, since different impellers may exhibit different BPF amplitudes, this approach may lead to inconsistencies in the associated vibration response.

In order to highlight the background of the current stall characterization with the limited-probes approach, in Figure 3-1 a Fast Fourier Transform (FFT) of a recorded signal of a dynamic pressure probe at the diffuser inlet is presented as an example: in particular, it refers to a case with a real diffuser stall rotating at a subsynchronous frequency.

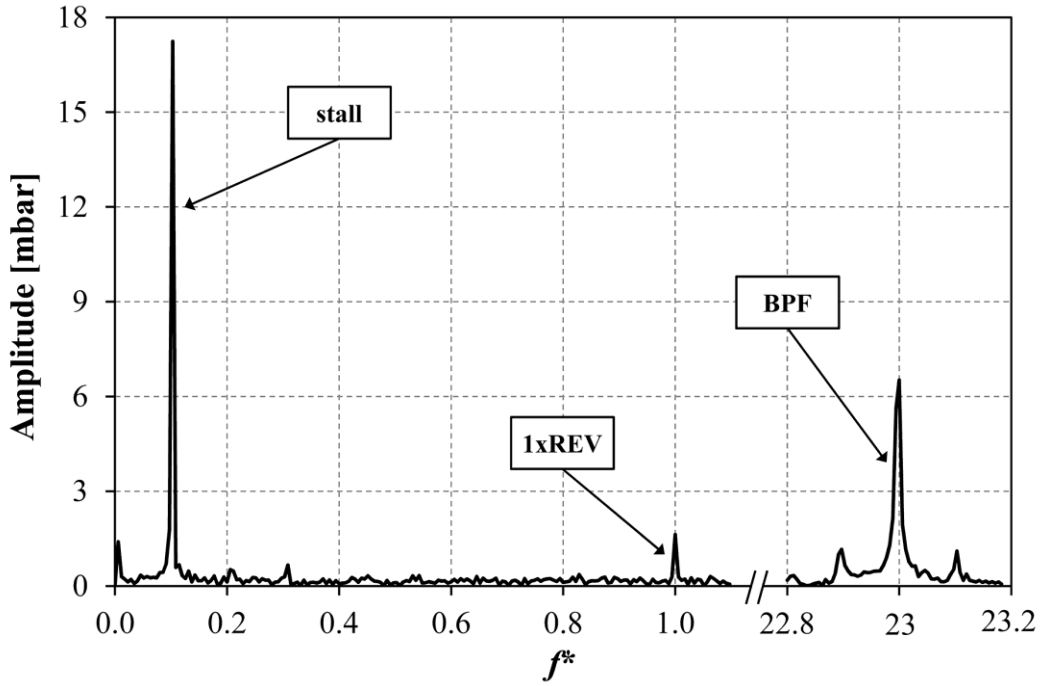

Figure 3-1. FFT Analysis of a real vaneless diffuser stall.

One can readily notice that where no other phenomena take place, the time signal recorded in stall condition is mainly composed by three different contributions at three different frequencies:

- Stall (and eventual harmonics)
- Impeller revolution (and eventual harmonics)
- Blade passing

All the frequencies are presented in a dimensionless form, i.e. the frequency divided by the impeller rotational frequency (1xREV).

This particular case refers to a rotating stall which rotates at a subsynchronous frequency of 10.5% of 1xREV. The impeller had 23 blades as confirmed by the BPF frequency 23 times higher than the rotational frequency.

As a confirmation of that, in Figure 3-2 the recorded time signal equal to the stall pattern revolution is compared to the reconstruction based on the three aforementioned contributions and their first two harmonics (1xStall + 2xStall and 3xStall): very good agreement can be appreciated between theory and experiments.

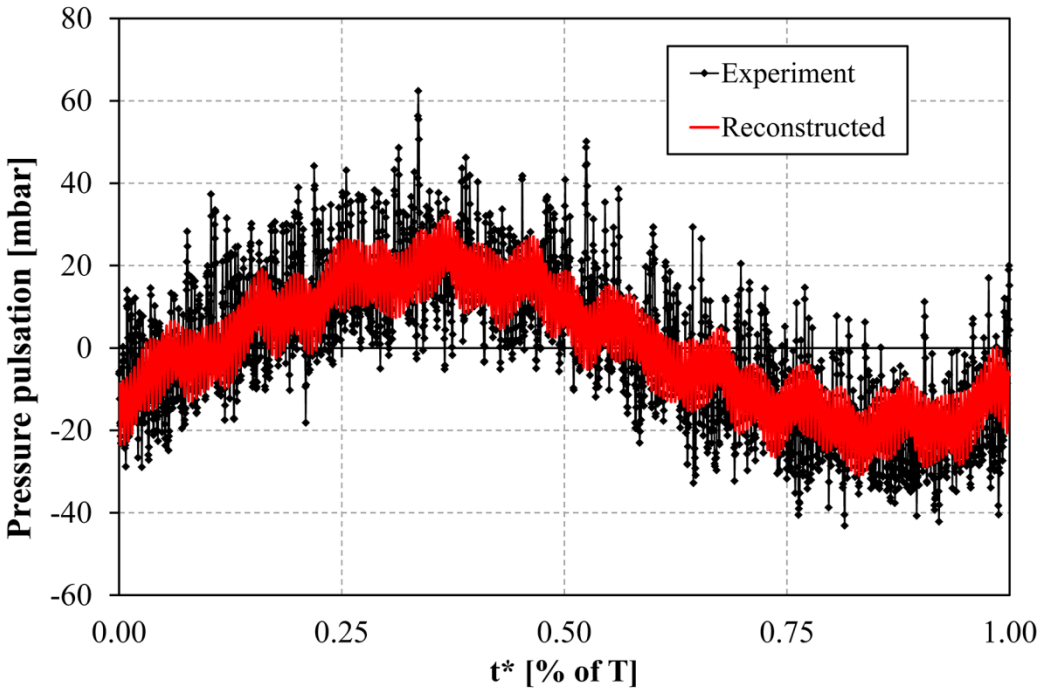

Figure 3-2. Comparison between a real measured signal and a reconstruction based on the stall, the 1xREV and the BPF.

As reported in literature [25], once the frequency of the phenomenon has been identified, before to proceed with the ensemble average, some important assumptions must be done:

- The stall pattern is supposed to rotate as a rigid body at a certain subsynchronous frequency.
- The stall pattern is supposed to be uniform between the hub and the shroud.

In order to perform the ensemble average approach of the time signal in a specific interval, the previous assumptions must be satisfied; if the frequency of the rotating stall has been correctly detected, the averaging process provides the average quantity of that specific period.

By exploiting the hypothesis on the rigid body rotation, is now possible to relate the time domain to the spatial domain; in other words, one can correlate the time interval in which the averaging process has been performed to a spatial angular sector [25].

The result of the averaging process (for more details on the ensemble average process please refers to Section (3.4.4)) of the same signal aforementioned is shown in Figure 3-3 and compared with the real signal recorded at the diffuser inlet.

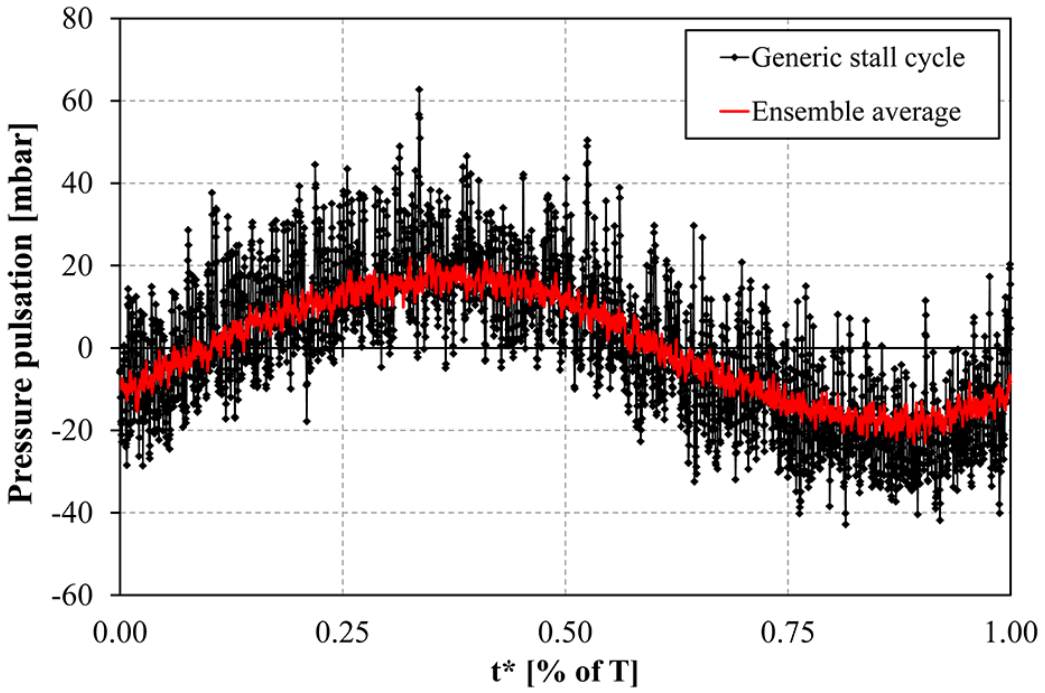

Figure 3-3. Comparison between a real measured signal and the ensemble average.

Upon examination of Figure 3-3, one can readily notice that the ensemble average approach acts as a low passing filter that cut all the frequencies above that one of interest, i.e. the stall frequency. Moreover, it is worth noticing that the pressure pattern is no more composed by three different contributions (as shown in Figure 3-2) but is mainly due the stall, since after the ensemble average, part of the information about the other contributions has been lost (e.g. the BPF).

Concerning the stall shape for this example case, Figure 3-3 shows only one fluctuation during the stall rotation highlighting a single-lobe pressure pattern.

The lobes' number (N) can be also calculated through the phase difference between the signals of two different probes ($\Delta\vartheta$) at a fixed spatial spacing ($\Delta\alpha$), as reported in Eq. 3-1.

$$N = \frac{\Delta\varphi}{\Delta\vartheta} \qquad \text{Eq. 3-1}$$

This approach represents the basis of the method that will be presented later on in this study; if the signals recorded by dynamic pressure probes in the diffuser shows clear frequency in its power spectrum and the stall shape consists in a single-lobe, a base approach as the presented could be applied. However, in case of noisy signal (quite frequent in the industrial field) or a multi-lobes pattern, the analysis of the time signal becomes more complex and a more sophisticated methodology is required to correctly analyze the experimental data. In particular, the identification of a multi-lobe stall could be very difficult in the event that the intensity of the unbalance between the lobes is not pronounced.

3.4 Developed stall analysis

In this study, a systematic procedure to fully characterize the rotating stall phenomenon with the ensemble average approach is proposed.

As discussed, in order to perform a correct averaging process, i.e. to average time data really connected to the same interval, a correct estimation of the period of the phenomenon is of capital relevance.

In order to introduce the whole procedure of the advanced approach developed in this study, an example based on a real test case analyzed will be previous provided starting from the test rig set up and measurement.

The procedure of data manipulation was realized by developing a proper routine in MATLAB ambient.

3.4.1 Test rig experimental measurements, procedure and results

Several experimental tests were carried out and analyzed in this study. Here below the layout, the instrumentation and the test procedure for one of the model test are described. All this aspects can be considered as general validity for all the model tests

carried out during this work except for the boundary conditions and the stage characteristics which were varied case by case.

Layout and Instrumentation

The test rig was operated in a closed-loop configuration with ambient pressure and temperature. In the presented case the working gas was CO2 (ρ_{gas} = 2.15 kg/m3 during the test) and the impeller's rotational speed was kept constant during the acquisition by means of a 2.5 MW variable-speed electric motor coupled with a gearbox.

The model test used to set up the advanced stall analysis approach reproduced an intermediate stage configuration of an industrial centrifugal compressor for high-pressure applications; in particular, in this way, a multistage compressor was simulated by a "pseudo-stage" in the flow path upstream of the impeller, which provided flow conditions at the inlet typical of those expected in a multistage compressor. For this purpose, the tested configuration was composed by a preswirler, an upstream deswirler, a 2-D impeller and a return channel as shown in Figure 3-4

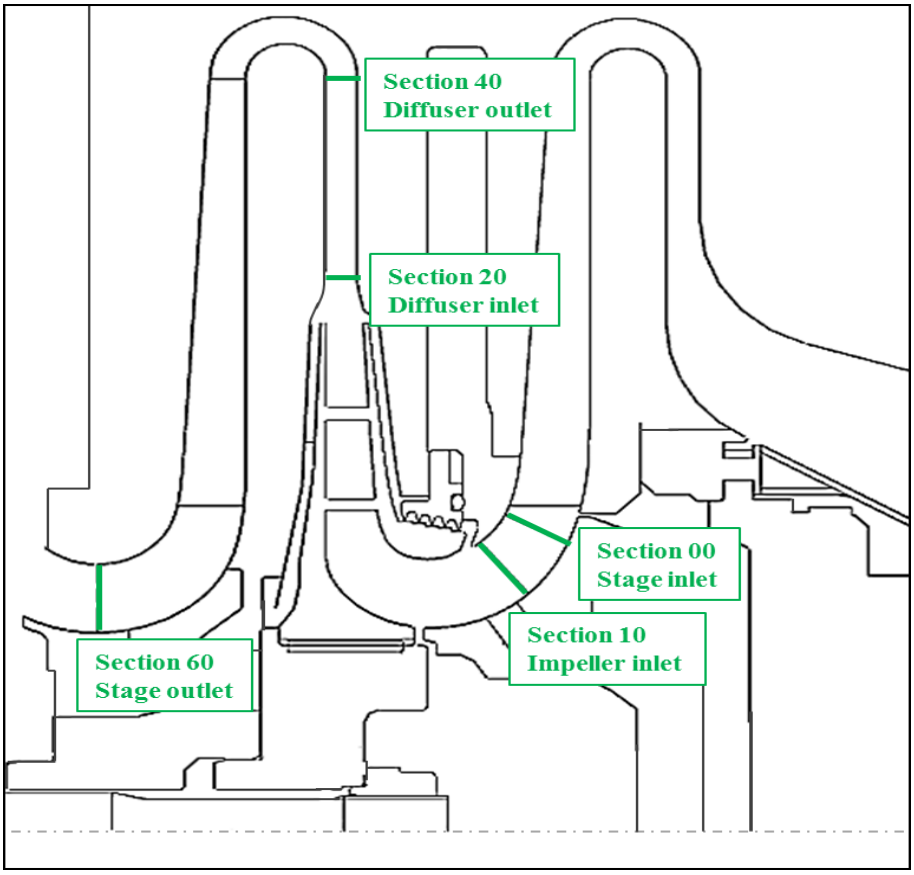

Figure 3-4. Scheme of the tested configuration.

The impeller was operated at its design peripheral Mach number (Mu) of 0.85. It had 23 two-dimensional blades and was characterized by a small value of the ratio between the blade outlet width and the impeller outlet radius $b_2/R_2 = 0.0353$.

Generally, during the tests, five measurements sections were equipped with different sensors (see Figure 3-4). In all sections, conventional measurements of pressure and temperature were performed; for further details on the standard instrumentation used in a similar test rig, please refer to Refs. [23] [24] [25] [29]. In addition, in order to investigate the pressure fluctuations in aerodynamically unsteady regime, dynamic pressure measurements were also provided in Section 20 and 40 of the all tested configurations; in few cases also an intermediate section (Section 30) at a half of the diffuser was provided.

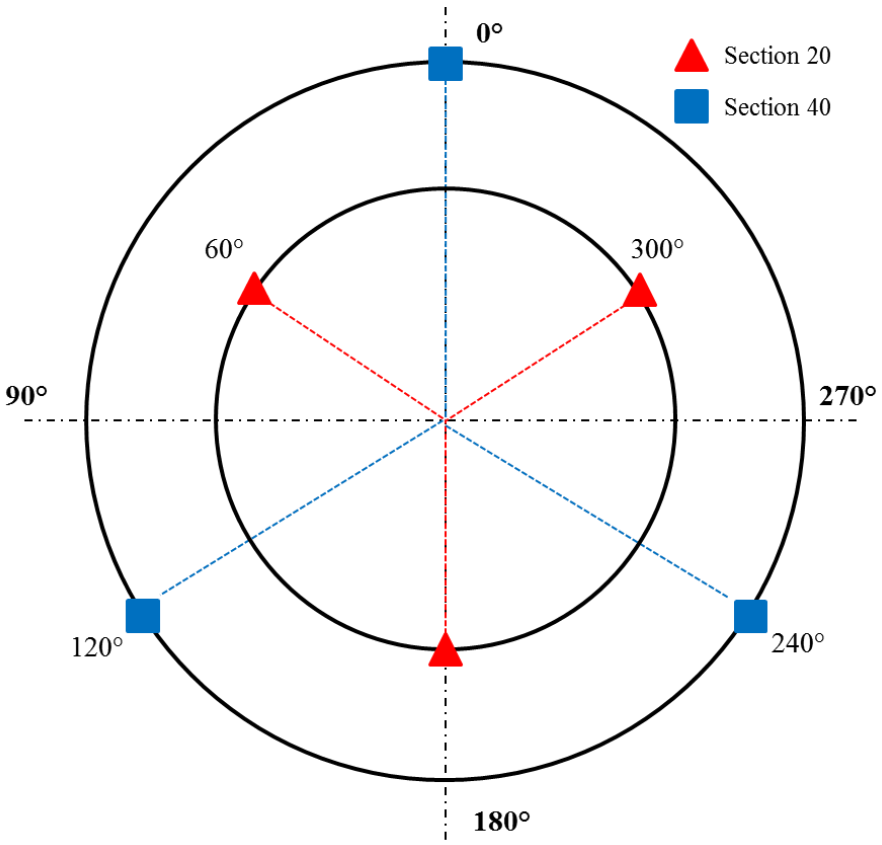

Figure 3-5. Circumferential positioning of the dynamic pressure probes.

Before this study, the pressure probes were equally spaced around the circumference of the diffuser and flush-mounted at both sections on the shroud side (see Figure 3-5). As it will be discussed later on in this work, this geometrical collocation did not represent the best solution to reconstruct the pressure pattern in the diffuser (especially in case of a three-lobes stall). The pressure pulsation were measured by means of commercial high-sensitivity piezoelectric sensors (PCB® piezoelectric sensors with a natural frequency of about 350 kHz) specifically designed for high-frequency measurements. In addition, the bearings of the impeller were instrumented with high-frequency (10 kHz) displacement sensors in order to monitor rotor vibrations.

All of the dynamic signals (pressure pulsations and vibrations) were continuously recorded with a bandwidth of 20 kHz. Both real-time and off-line analyses were performed by means of proprietary pieces of software.

Test Procedure

The acquisition of the data for all the model test analyzed were carried out by keeping constant both the rotational speed and the inlet pressure (in this case 1 bar). Dynamic pressure data were continuously recorded and stored in a personal computer.

As regard the test procedure, it starts from the overflow condition and then a regulation throttle valve is closed step by step towards the surge conditions. After each regulation step, a few seconds of acquisition time (sufficient to guarantee a steady-state condition) is always provided. Once the surge is reached, the throttle valve is gradually re-opened; by doing so, the dynamic pressure transition due to the stall and the surge can be both analyzed.

Once the time data coming from the streaming analysis are stored, the test results are first examined in order to identify the main characteristics of the detected phenomenon in the frequency domain.

In detail, the frequency components of the signals are extracted in consecutive analysis windows in time by means of the power spectrum analysis [25].

The power spectra are then collected in a joint time-frequency graph characterized by a 3-D visualization in which the axes correspond to the frequency, time, and amplitude of the signals.

For sake of clarity, in Figure 3-6 the amplitude values are highlighted with a color scale. Frequencies are reported in the ordinate axis, while the acquisition number is reported in the abscissa axis (i.e. it corresponds to different mass flow rates). As regard the amplitude, the color intensity represents in each point the amplitude of the specific frequency component at that instant.

Moreover, a vertical section of the graph represents the signal power spectrum analysis of one sensor at that specific time. As one can readily notice, the stall inception frequency and its evolution during the stall can be clearly distinguished, together with its two harmonics. At a specific time, after a certain closing step of the throttling valve, a strong perturbation that involves the entire frequencies domain is clearly marked: this phenomenon can be traced back to the surge.

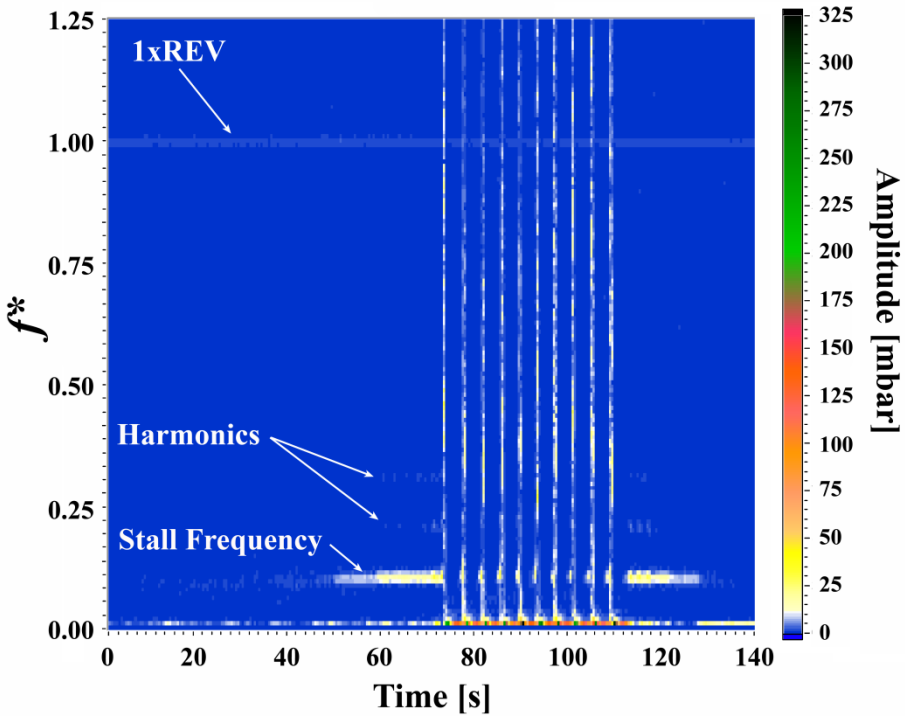

Figure 3-6. Joint time-frequency graph of the test.

Results

The analysis of the results started from the examination of the joint time-frequency graph which reported the stall analysis for one pressure sensor at Section 20, where the frequency is presented in a dimensionless form, i.e. divided by the revolution frequency (1xREV).

In the graph, a well-marked subsynchronous frequency can be note before surge running forward at a very low frequency (approximately 10% of the impeller revolution frequency), as a result of a rotating stall induced in a static component of the stage. In this case, based on previous experience on this type of machine and on the literature, a vaneless diffuser stall was hypothesized. Moreover, two very low-intensity harmonics were detected.

Before proceeding with the stall analysis two different checks were needed, in order to verify the development history of the subsynchronous frequency detected.

The power spectra of the signals in the range between 0 Hz and the 1xREV were first investigated every second, starting from the inception of the stall, collocated at

t=52 [s], up to reach the surge. It is worth noticing that no other frequency than the stall one appeared in the spectrum, suggesting that no other phenomena took place during the stall.

The second check consisted in a streaming data manipulation in order to monitor the integral of the frequency spectrum of the dynamic pressure sensors in an interval of 2**df* (where *df* is the sampling frequency) centered in the observed stall frequency.

Figure 3-7 shows the measured trend for one of the pressure probes at Section 20 as a function of time, together with dimensionless flow coefficient φ^*, i.e. the actual flow coefficient divided by the design one.

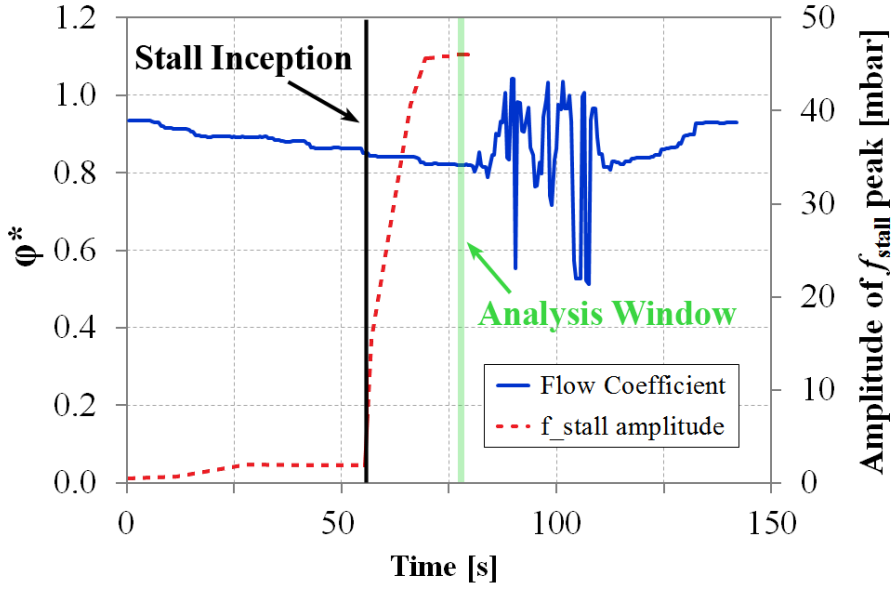

Figure 3-7. Development history of the subsynchronous frequency.

In Figure 3-7 one can also notice that the stall inception started at a certain closing step of the throttling valve ($\varphi^* < 0.85$), but the final value of the amplitude of the subsynchronous frequency was reached only after another closing step of the valve; above this step, no further increment of the amplitude of the pressure pulsation was noticed.

After these considerations, a suitable choice of the window to perform the advanced stall analysis was then possible; in detail, a 2 s interval was selected as highlighted in Figure 3-7 with a green-shadowed line in order to guarantee an

adequate distance from the surge zone but in the fully-developed-zone of the unsteady phenomenon. Furthermore, in this case, the window's length allowed to ensure an accurate time-averaging process by including approximately 40 passages of the stall cells comprehended.

As a last step of this first part of the stall analysis, the power spectrum of the three pressure sensors in the selected window analysis was monitored to verify the agreement between the sensors themselves in term of measured amplitude. In Figure 3-8 a frame corresponding to t = 71 s is reported: excellent correspondence can be noticed.

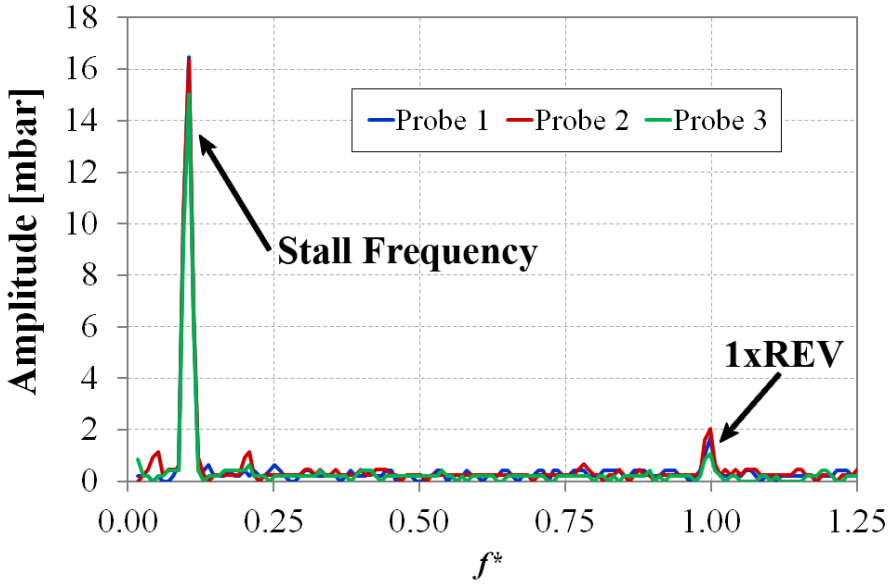

Figure 3-8. Power spectrum of the three pressure probes at Section 20.

After these preliminary checks, a correct estimation of the period of the phenomenon is needed in order to perform a correct averaging process (i.e. to average the time data really connected to the same interval).

Although an estimation of the stall frequency was already provided by the previous time-frequency analysis, due to the low frequency resolution of the power spectrum obtained with the industrial tool and to some other factors that will be discussed later on in this study, a more accurate method to evaluate the stall frequency was needed.

3.4.2 Signal's selection and filtering

Starting from this section, the MATLAB routine to reconstruct the pressure pattern and calculate the resulting force will be introduced through the various steps.

In the first step two dynamic pressure sensors were selected; by doing so, if, as in this case, the sensors for each section are three, one is at the moment discarded.

The first signal was used to provide the time data for the reconstruction of the pressure field, whereas the second one represented the comparison signal to calculate the phase shift. However, the whole analysis was, indeed, performed on each pair of signals in order to verify correctness of the approach and to confirm the agreement between the three probes.

As regard the filtering process, the mean value of each signal was subtracted from the signal's value, due to the nature of the piezoelectric sensors used (all the frequencies are superimposed on each other). Then, each signal of the two data sets was filtered with a low-pass digital filter in the time domain [48], which allowed one to cut out the frequency contributions higher than the 1xREV. After this process the signal is clean and almost ready both to be averaged by the ensemble average process and to be used in the next steps of the procedure, i.e. the stall frequency and the lobes' number determination.

3.4.3 Determination of the stall frequency and the lobes' number

In order to determine the stall frequency and consequently the lobes' number with more accuracy than the previous time-frequency analysis presented, as a second step of the routine, the auto-correlation and cross-correlation functions were applied [48]. The auto-correlation of a generic signal x is defined in Eq. 3-2. In particular, by analyzing the equation, the auto-correlation of a signal allows one to verify if a signal contains a component that is related with itself in a sufficiently long time of the analysis T.

$$C_{xx}(\tau) = \sum_{t=-\infty}^{+\infty} x(t)x(t+\tau) \qquad \text{Eq. 3-2}$$

By moving this concept into the analysis of the pressure streaming data, if one identifies the time shift which maximizes the auto-correlation function, is able to identify also the period of the most relevant frequency contained in the signal. The stall frequency can be hence calculated by the reciprocal of the time delay between two peaks of the function. The results of these two steps are shown in Figure 3-9; upon examination of the figure, it is possible to note the pressure signal of Probe 1 at section 20 during the analysis window, the filtered signal and the calculated auto-correlation function, which in this case allowed to identify a stall frequency of 10.5% of 1xREV.

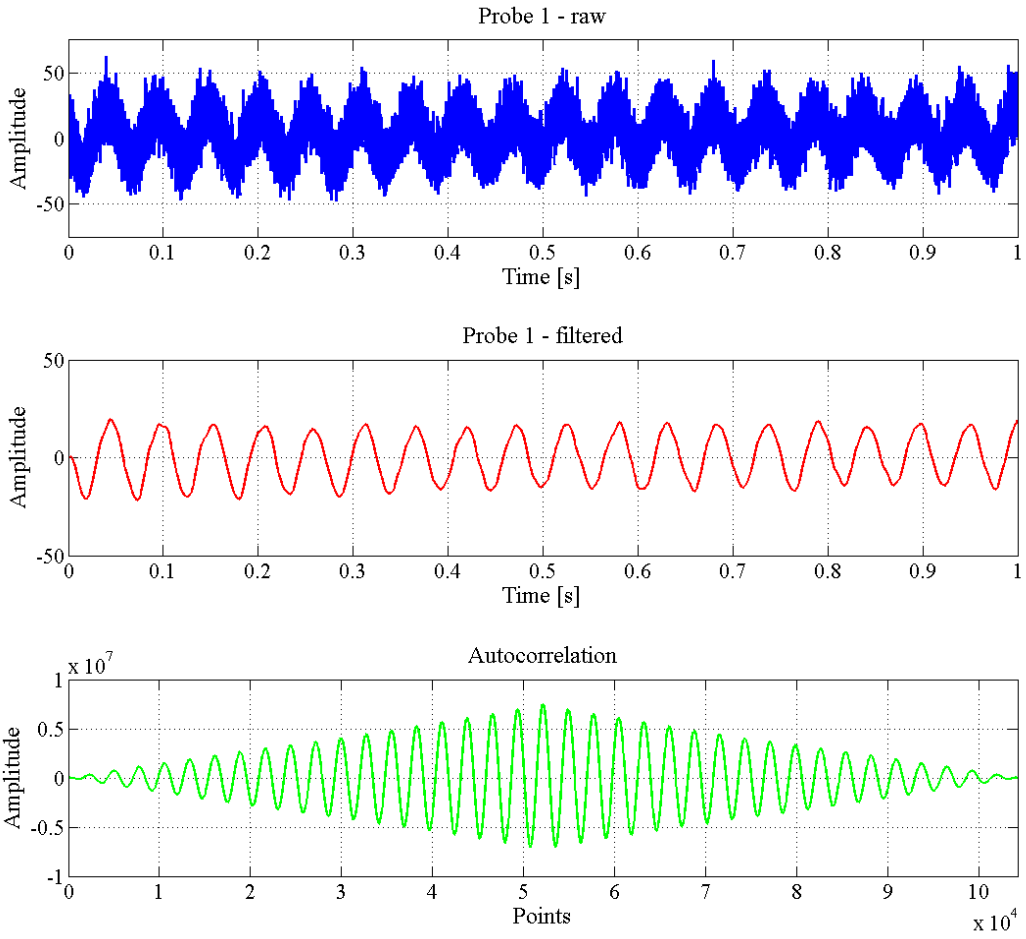

Figure 3-9. Pressure signal of Probe 1 at Section 20 and its auto-correlation.

After the auto-correlation has been performed, the cross-correlation function was used to define the phase shift between two signals (in this case the result of Probes 1 and 2 is shown, but the analysis was performed on each couple of signals), according with Eq. 3-3.

$$C_{xy}(\tau) = \sum_{t=-\infty}^{+\infty} x(t)y(t+\tau) \qquad \text{Eq. 3-3}$$

The time shift between zero and the peak of the cross-correlation can be multiplied by the stall revolution velocity to give the phase difference between the two signals ($\Delta\vartheta$). The result of the cross-correlation is shown in Figure 3-10 and it highlighted a shift between the two signals at the stall frequency detected of approximately 120 deg, hence revealing a stall pattern with a single lobe (by using Eq. 3-1).

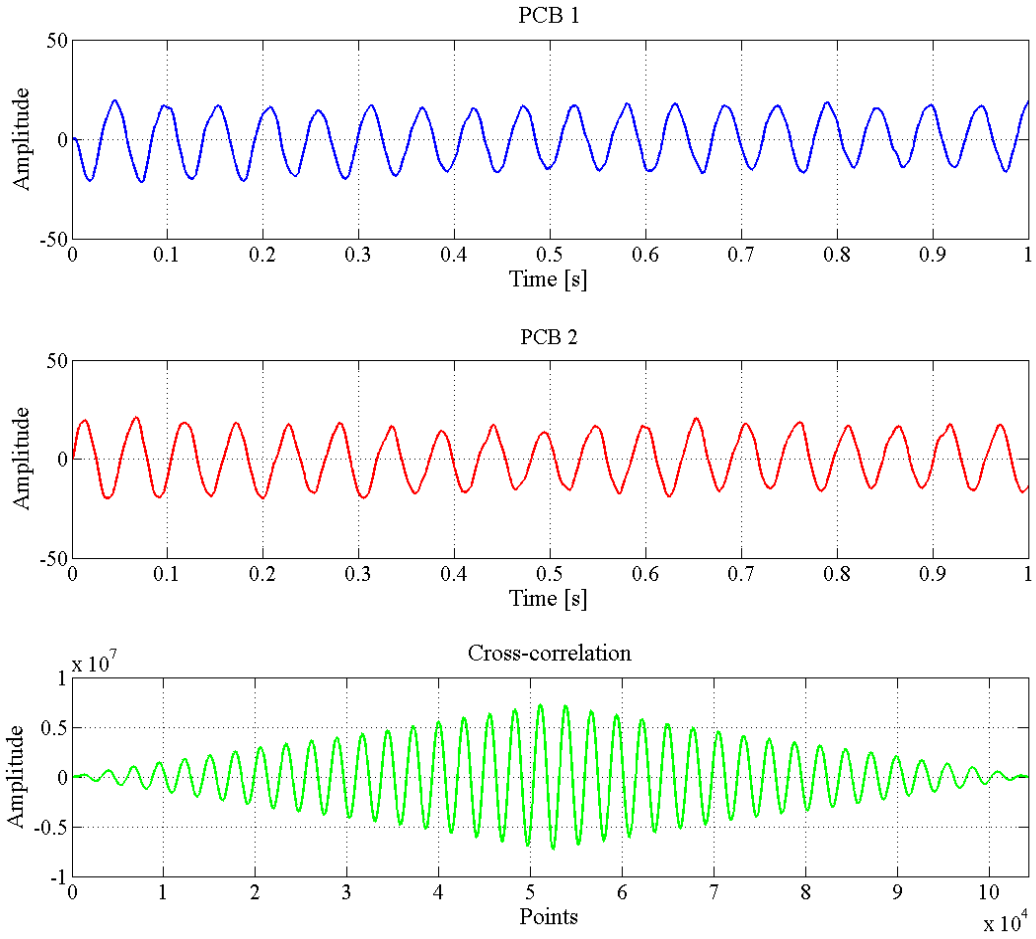

Figure 3-10. Pressure signal of Probes 1 and 2 at Section 20 and their cross-correlation.

3.4.4 Stall pattern reconstruction

Before reconstructing the diffuser stall pattern, the ensemble average approach was first applied to the pressure signal of Probe 1.

Furthermore, in order to reach the final goal of describing the rotating stall in terms of intensity and frequency, some basic assumption must be done. In particular, the reconstruction of the force is based on the transposition of a signal in the time domain (i.e. the dynamic pressure measurements) into information in the space domain (i.e. the circumferential distribution at a specific section).

As aforementioned, in order to enable this domain shift, the hypothesis that the stall rotates like a rigid body must be assumed. Then, if this assumption is accepted, it is possible to perform the ensemble averaging process [49] [50] on the time data. By doing so, the information in the time domain can be transfer into the space domain and the average pressure distribution cab be reconstructed in the circumferential direction.

In detail, once the period during which the phenomenon *x* is taking place, has been detected, the ensemble average approach allows one to average the time signal in a specific interval *t* to obtain the average of the quantity on it, as shown in Eq. 3-4.

$$\langle x(t) \rangle = \lim_{N \to \infty} \frac{1}{N} \sum_{i=1}^{N} x_i(t) \qquad \text{Eq. 3-4}$$

Based on the assumption of a rigid rotation of the stall, is then possible to relate the time interval in which the average has been performed to a spatial angular sector.

In Figure 3-11 is shown the reconstruction of the pressure pattern after the ensemble average process.

Furthermore, the polar plot of Figure 3-12, in which the pressure distribution was superimposed on a reference pressure level to highlight the stall pattern, clearly shows the single lobe nature of this case study.

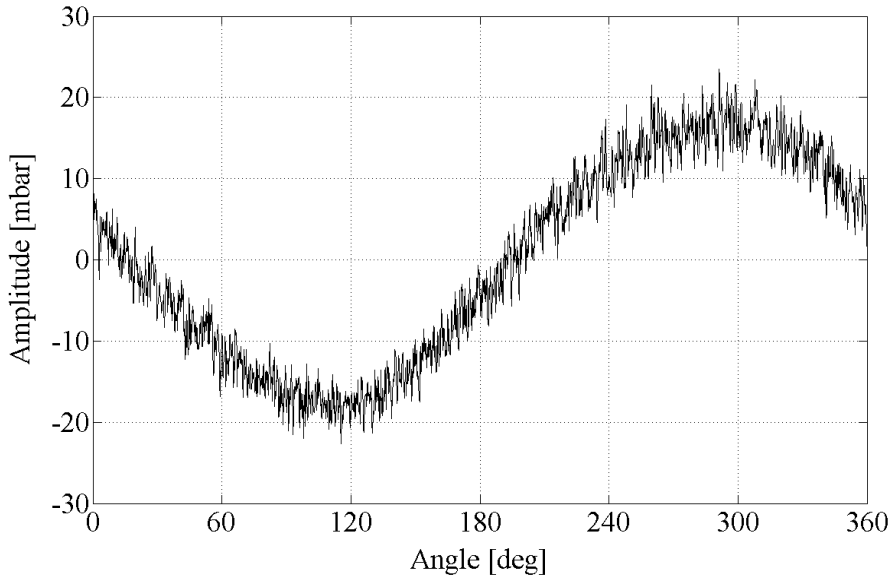

Figure 3-11. Calculated circumferential distribution due to the rotating stall at Section 20 (with standard deviation).

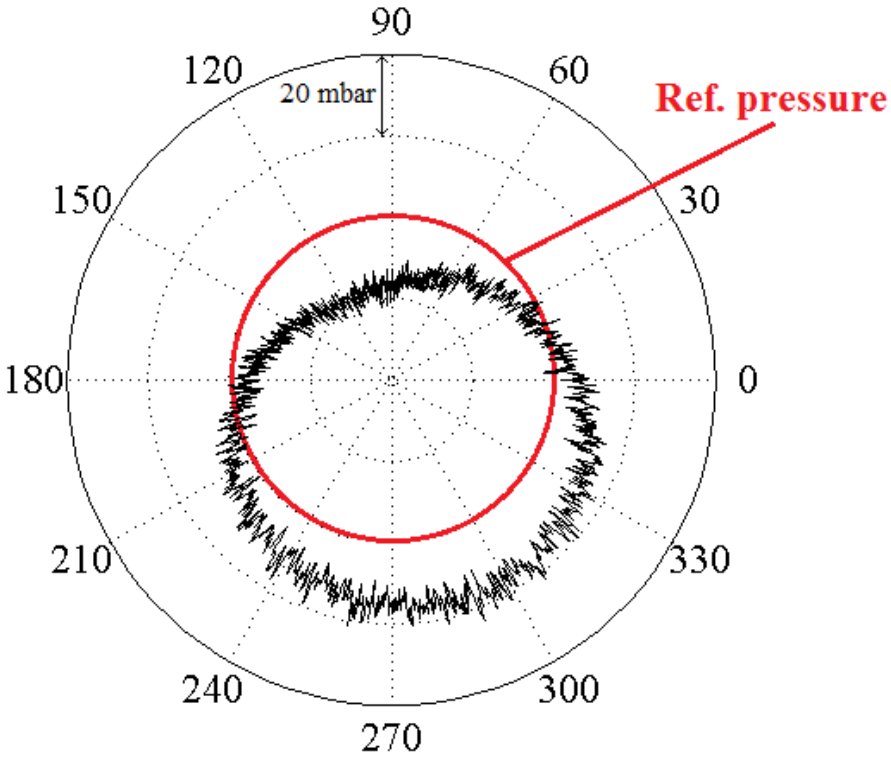

Figure 3-12. Polar plot of the single lobe stall pattern.

The same procedure was also applied to Section 40 (the diffuser outlet) in order to highlight the behavior in the radial direction (see Figure 3-13).

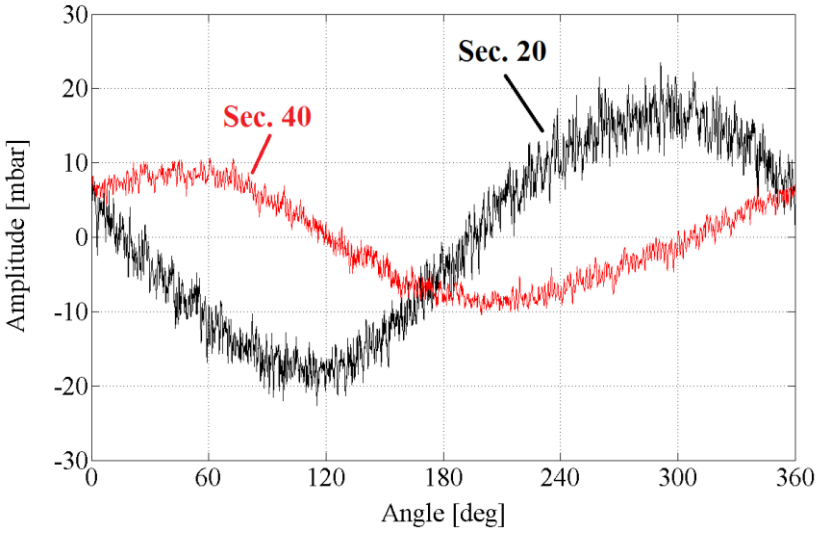

Figure 3-13. Comparison of circumferential pressure distributions at Section 20 and 40.

The analysis confirmed that the stall pattern is still composed by a single rigid lobe rotating at the same frequency and the pressure fluctuation at this section is reduced by almost 50% with respect to the Section 20.
If one neglects as a first approximation the induced distortions of the radial velocity distribution at the impeller exit, the unbalancing force acting radially to the rotor is indeed given by Eq. 3-5, i.e. considering the resultant of the non-axisymmetric pressure pattern around the impeller and integrating the pressure on the area on which it is thought to be applied.

$$F_{stall} = \int_0^{2\pi} p(\alpha) b_{sect} R_{sect} d\alpha \qquad \text{Eq. 3-5}$$

The aspect related to the resulting force of the unbalance pressure field will be however discussed in depth later on in this study.

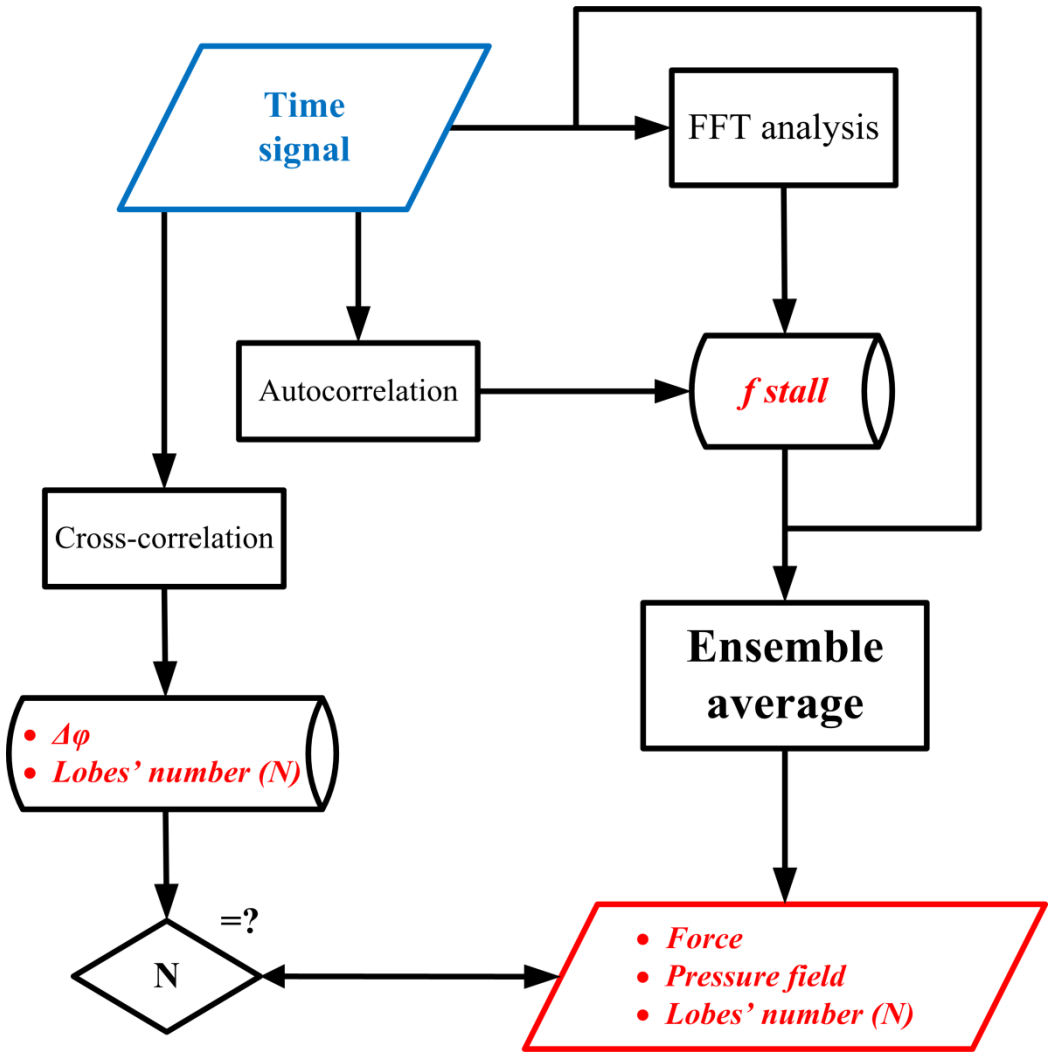

Figure 3-14. Flowchart of the advanced stall procedure.

As a final consideration, it is worth noticing that the proposed procedure is of general validity for a vaneless diffuser stall (see Figure 3-14). It represents a useful tool in evaluating the unbalance of the pressure field even in case of complex stall pattern that show two or more lobes; in these cases the pressure pattern cannot be traced to a simple sinusoid and its harmonics and an accurate analysis with this advanced procedure is needed. In the next chapter the multi-lobes cases will be presented and discussed.

3.5 Real-time analysis

As previously mentioned, in this section prospects and drawbacks of a real-time analysis will be introduced and discussed.

This type of approach is based on the use of a higher number of dynamic pressure sensors than the previous one. In order to perform the real-time analysis, a sufficient number of probes should be installed along the circumference of the diffuser at different radial sections. Then, by acquiring all the sensors simultaneously, a series of "snapshots" of the stall pattern is promptly provided and hence the evolution of the unsteady phenomenon can be reconstructed.

In order to point out the potentiality of this methodology, an example of a single lobe stall (real signal) at a certain time, reconstructed by using six equally spaced pressure probes is given in Figure 3-15.

Before entering into the core of the discussion, two main issues must be taken into account in evaluating this kind of approach. The first one is related to the high costs of installing a high number of probes (not analyzed in this study) while the second regards the number of probes to install in relationship to required accuracy and mechanical problems for the sensors mounting.

By neglecting the mechanical problems for a moment, the probes' number can be defined with respect to the characteristics of the stall.

First of all, the minimum number of sensors required to describe the pressure pattern is however given by Eq. 3-6, according to Nyquist's theorem [48].

$$\#\,\text{probes} > 2N \qquad \text{Eq. 3-6}$$

Starting from this consideration, the probes' number can be increased as a function of the required accuracy in the final reconstruction of the stall pattern.

In particular, in this study, a sensitivity analysis in which the accuracy of the reconstruction has been evaluated by varying the number of probes will be presented.

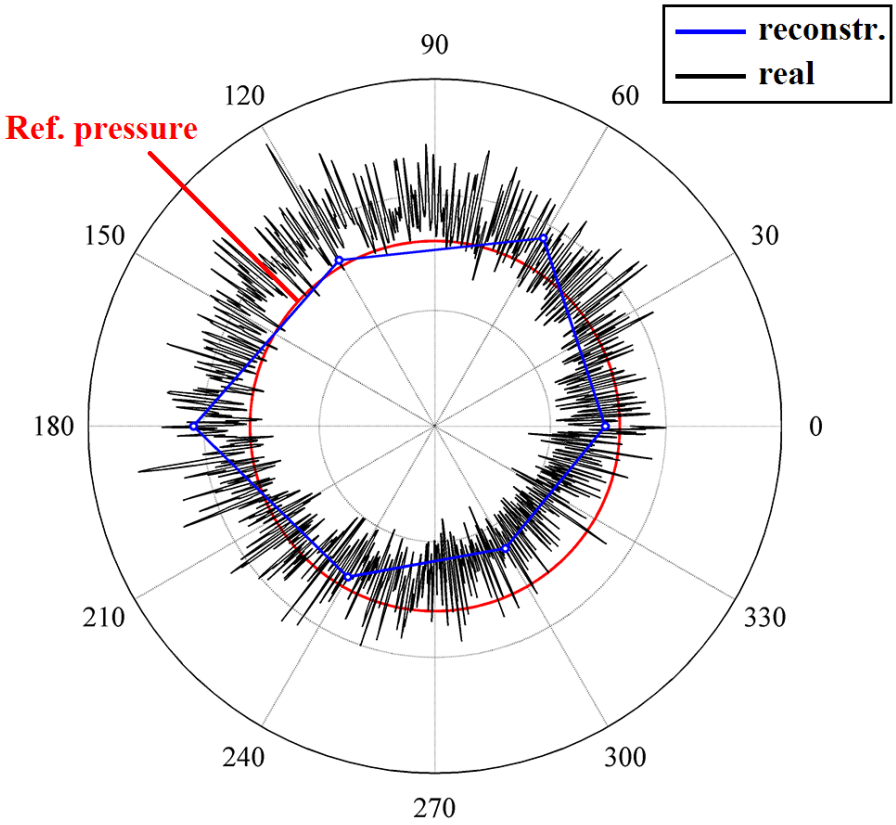

Figure 3-15. Comparison between the real signal of a single-lobed stall and the real-time reconstruction using 6 equally-spaced probes.

By using a discrete number of measure points, the description of the stall pattern, which is not exactly axisymmetric (in this case a single lobe) and presents a high noise level, can be altered depending on the sensors position in the revolution cycle.

In order to investigate this phenomenon, in the present analysis the resulting force value (per unit area of the diffuser inlet, F^*) was calculated (according with Eq. 3-5) for each angular position with a step of only 1° and gathered in the plots in terms of average value superimposed to range bars which represent the minimum and the maximum value of all the calculated values in the whole revolution.

As a first step, in Figure 3-16 the resulting force of two real measured stall with one and two lobes (that will be presented later on in this study) is reported as a function of the (equally spaced) probes' number. In particular, the raw signals directly coming from the dynamic pressure probes have been used in order to

reproduce a real industrial acquisition. In this first case, a linear interpolation was used between the measured values along the circumference.

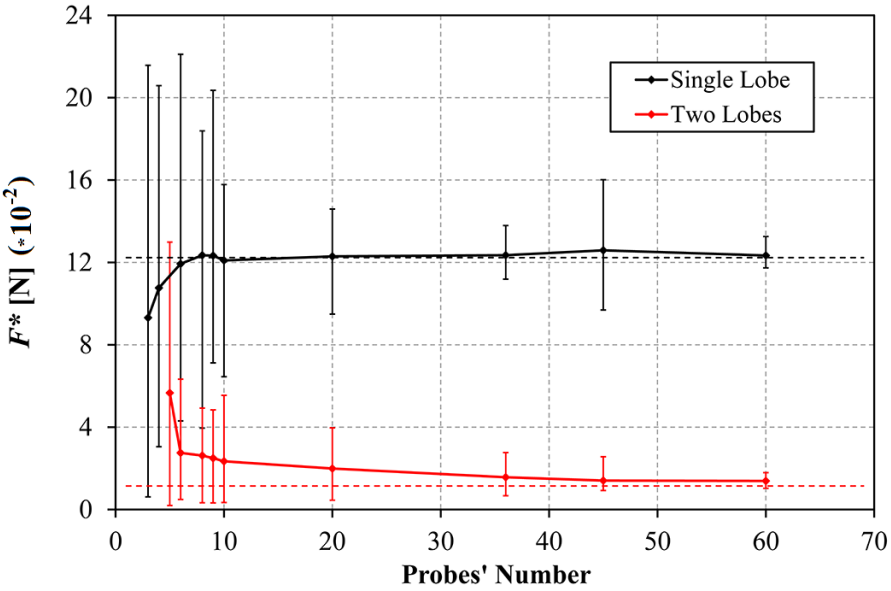

Figure 3-16. Real-time force reconstruction as a function of the probes' number in case of a single and a two lobes stall pattern: unfiltered signals – linear interpolation.

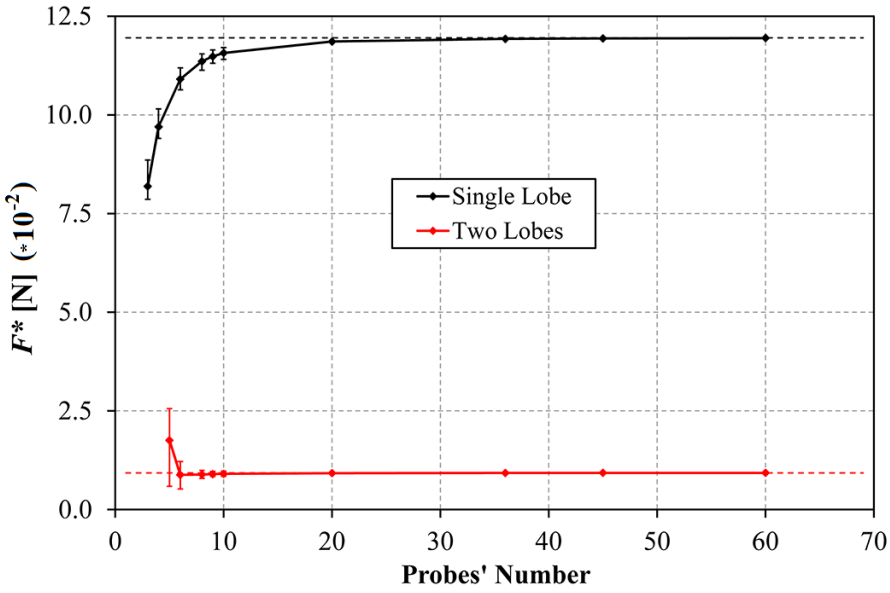

Figure 3-17. Real-time force reconstruction as a function of the probes' number in case of a single and a two lobes stall pattern: filtered signals – linear interpolation.

By examining Figure 3-16, one can readily notice that the average force value is correctly reproduced in case of 20 or more probes are used for a single lobe stall, while the probes' number increases up to 36 for a two lobes stall.

The range of calculated values is however very widespread in case of less than 10 probes, mainly due to the spikes present in the real signals which affected the predicted pressure pattern.

As a second step, the possibility to filter the signal was investigated. In the previous sections the ensemble average process was analyzed and it was highlighted that a filtering of the frequency components higher than the stall phenomenon does not affect the force calculation. Starting from these considerations, a signal filtering based on a low-pass filter locked at the 1xREV frequency was applied to the same signals used in Figure 3-16. After this filtering process (easily obtainable also in an industrial acquisition), a linear interpolation was again performed between the measured values along the circumference, as reported in Figure 3-17.

The results of this second step highlight that the dispersion of the data is clearly reduced with respect to the previous case in which the raw data was used. In this case, for single lobe stall, an almost perfect description of the total force can be reached with 20 probes or more. As regard the two lobes stall, it is worth noticing that to obtain the same accuracy of the single lobe case 20 probes are sufficient; although the very low force connected to this particular pattern can be detected also with ales number of probes.

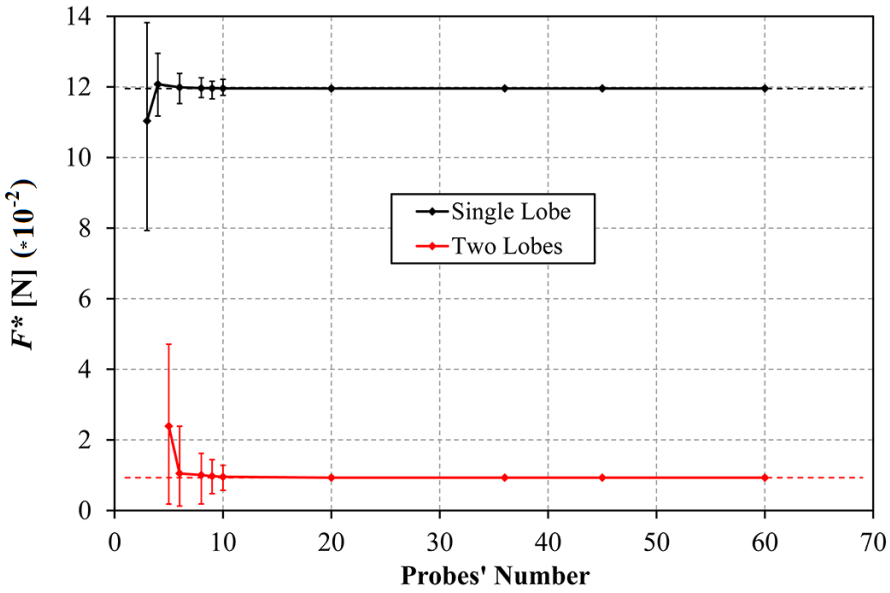

Figure 3-18. Real-time force reconstruction as a function of the probes' number in case of a single and a two lobes stall pattern: filtered signals – spline interpolation.

The analysis was then repeated changing the typology of interpolation: in this case, a spline interpolation was selected (Figure 3-18) since this solution is thought to be easily available in acquisition software even in industrial application.

Upon examination of Figure 3-18, one can notice that the choice of the spline interpolation has reduced the number of probes needed to correct reconstruct the stall pattern and consequently the resulting force; in this case 10 or more probes can be considered sufficient.

As a final consideration, it must be remark that the number of "snapshots" in which the force was not correctly captured sensibly increases for lower probes' number; in this case the spline interpolation can lead to wrong stall shapes.

4. Industrial database analysis

4.1 Introduction

Since this study was led in collaboration with *GE Oil & Gas*, a detailed analysis of a wide industrial model test database was first carried out in order to highlight the stall characteristics in terms of frequencies, force and geometry parameters.

To reach this goal, the advanced procedure of stall analysis presented in the previous chapter was performed to explore the experimental data coming from several model tests which were constituted by a single stage configurations similar to that one presented in Figure 3-4.

The available data set consisted of experimental data coming from 16 different model test campaign having different configurations, peripheral Mach number (*Mu*), working pressure and working fluid. The result of these differences is in a global amount of more than 60 different tests analyzed. All the tests were carried out in a specialized test rig operating in a closed loop with constant pressure and temperature at the inlet as previously discussed.

The tested models reproduced both intermediate and pseudo-axial stages of industrial centrifugal compressors equipped either with a 2D or a 3D impeller and a pre-swirler, an upstream de-swirler, a return channel and a scroll according to the relative configuration. Although geometric details cannot be reported in the study due to a non-disclosure agreement with the industrial partner, it is worth pointing out that the analyzed impellers had b2/R2 and R4/R2 ratios in the ranges 0.05-0.15 and 1.40-

1.65, respectively. The peripheral Mach numbers were in the range between 0.3 and 1.32, whereas the design flow coefficients of the impellers were enclosed between 0.02 and 0.16. In the following sections, some of these tests analyzed will be presented and discussed in detail in order to highlight both the stall characteristics in terms of stall pattern, frequency and force, and the influence of the main parameters on the pressure unbalancing.

4.2 Stall analysis results: stall pattern shape

The results of the wide stall investigation carried out on the industrial data base was first analyzed in term of stall pattern shape in order to highlight both the most common configurations assumed by the pressure pattern due to the stall inception and the main issues related to their detection.

The single lobe stall pattern was already discussed in the previous chapter and it will be not repeated here.

Even if the single lobe stall was the most present pressure pattern found in the industrial database, other shapes were observed; in particular, two and three lobes have been detected and analyzed.

The first case that will be presented is a two lobes stall; this particular configuration highlighted some important aspects that must be taken into account to correctly reconstruct the pressure unbalance. In detail, two different typology of a bi-lobed pattern can be found and some clarifications must be done.

Bi-lobed stall

In Figure 4-1 the FFT analysis of a two lobes stall signal (without any filtering process) is reported. As indicated, the stall frequency (i.e., the frequency linked to the rotation of the generated pressure pattern) is represented by the lowest contribution (in frequency) of relevant amplitude in the spectrum, i.e., the natural frequency of a generic rotating body.

As it is possible to note in the FFT analysis, the revolution stall frequency is not the most intense, while the highest amplitude is connected to the pressure ripple related to each lobe of the pattern (i.e. the peak at double frequency).

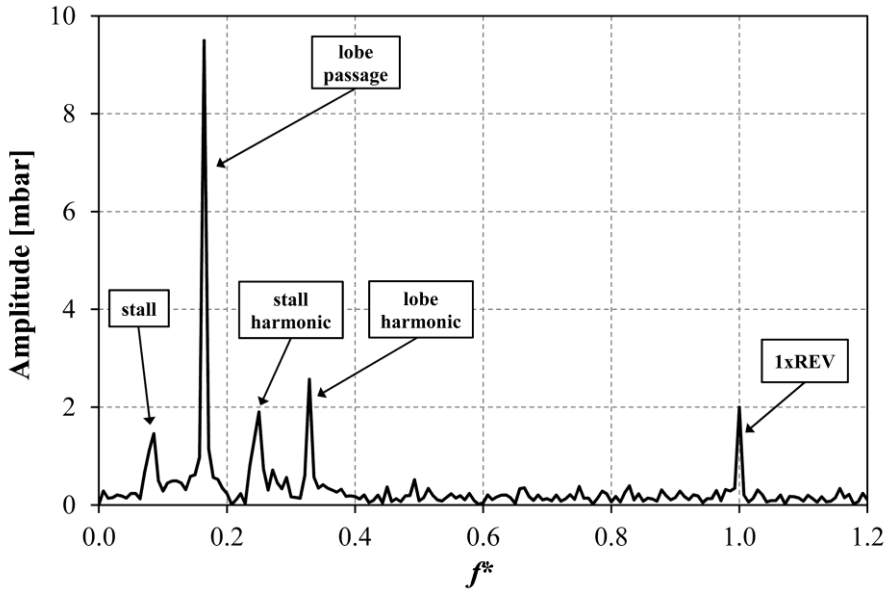

Figure 4-1. FFT analysis of a real two lobes stall: all the frequencies are presented in a dimensionless form, i.e. $f^*=f/f_{1xREV}$.

In this case, the selection of the right stall frequency cannot be simply based on the industrial assumption that the highest subsynchronous frequency is that one connected to the rotating stall; however, the auto-correlation function is indeed able to catch the correct frequency of the unsteady phenomenon by comparing the time raw signal with itself. This will be then confirmed by cross-correlation function by detecting the phase difference between two probes.

In Figure 4-2 the correct stall pattern reconstruction is reported.

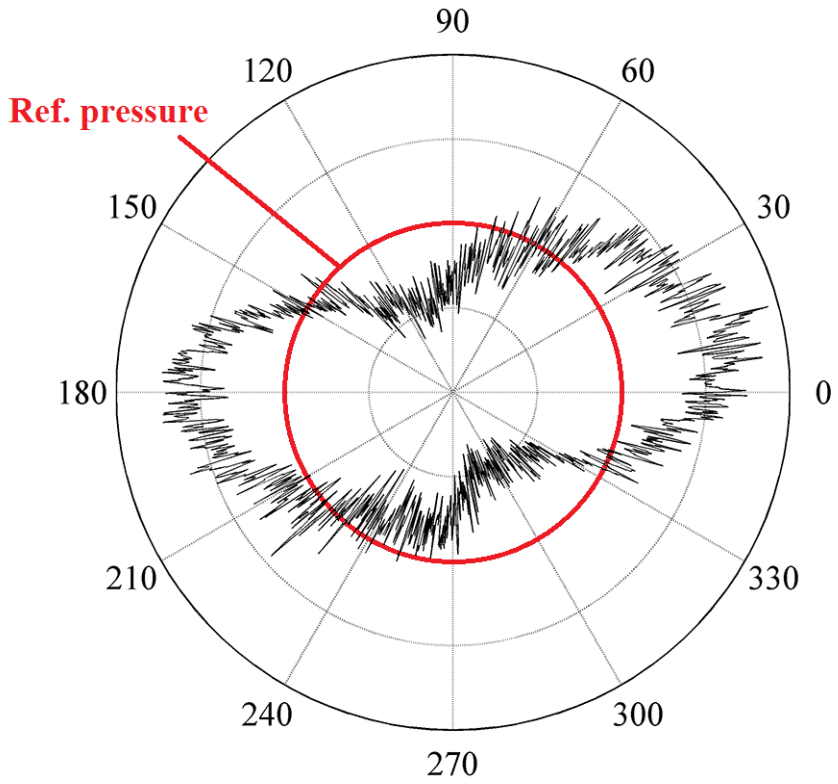

Figure 4-2. Reconstruction of the stall pattern at the inlet section of the diffuser.

Upon examination of these results, a modification of the conventional Eq. 3-1 is proposed in order to extend its validity. In fact, in case the correct stall frequency (i.e. the frequency at which the entire stall pattern – considered as a rigid body – is moving) has been defined, the calculated angular phase shift will be equal to the physical angular distance between the two examined probes $\Delta\alpha$ (Eq. 4-1).

$$\Delta\vartheta = \Delta\alpha \Big|_{f=f_s} \qquad \text{Eq. 4-1}$$

where the subscript *s* indicates the revolution stall frequency.

Now this equation is of general validity in detecting the lobes' number, but on the other hand, if the frequency related to the lobe passage is accidentally selected, the cross-correlation function will be no longer satisfied. In this case, Eq. 3-3 would highlight that the frequency selected is not the right one for the averaging process.

In the time domain, the symmetrical fluctuation is indeed assumed as a signal rotating at a frequency N times higher than the whole stall pattern.

If one uses this frequency, however, the lobes' number can be easily calculated with Eq. 4-2.

$$N = \left. \frac{\Delta \vartheta}{\Delta \alpha} \right|_{f = f_l} \qquad \text{Eq. 4-2}$$

where the subscript *l* indicates the frequency of the lobe passage.

Nearly symmetric bi-lobed stall

This modification of the equation to calculate the lobes' number is of particular relevance because it is of general validity. In particular, it can be used in case of a singular stall configuration that has been sometimes observed in the analyzed industrial database such as a multi-lobed pattern in which the lobes are nearly symmetric.

As it is possible to note in Figure 4-3 and Figure 4-4 in which a real nearly symmetric two lobes stall is reported. In this case, the stall intensity is generally weak and the resulting unbalance is significantly reduced. As a consequence, the pressure pattern is more equilibrated and the force is closer to zero than that one presented in Figure 4-1and Figure 4-2.

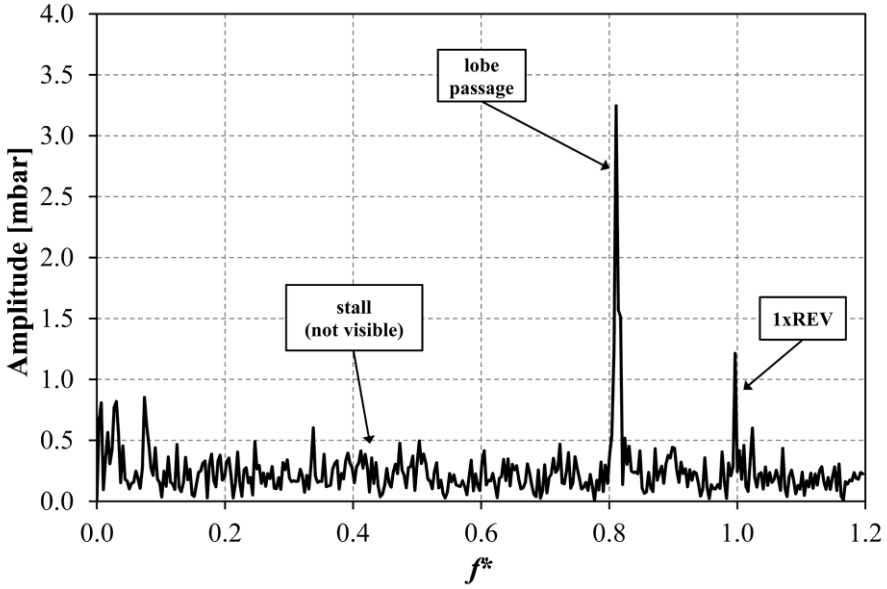

Figure 4-3. FFT analysis of a real nearly symmetric two lobes stall: all the frequencies are presented in a dimensionless form, i.e. $f^*=f/f_{1xREV}$.

Upon examination of Figure 4-3, one can conclude that the only analysis of the power spectrum can lead to a wrong evaluation of the stall shape. The revolution frequency of the stall pattern is not visible while the frequency connected to the lobe's passage is the highest contribution in the spectrum.

In this case the auto-correlation does not allow to identify the right frequency of the stall revolution and a single lobe stall could be still hypothesized. In order to clearly detect the stall nature of this case a further data manipulation is needed.

As aforementioned, by applying Eq. 4-2 to the lobe's frequency is it now possible to reveal the multi-lobed nature of the stall pattern univocally.

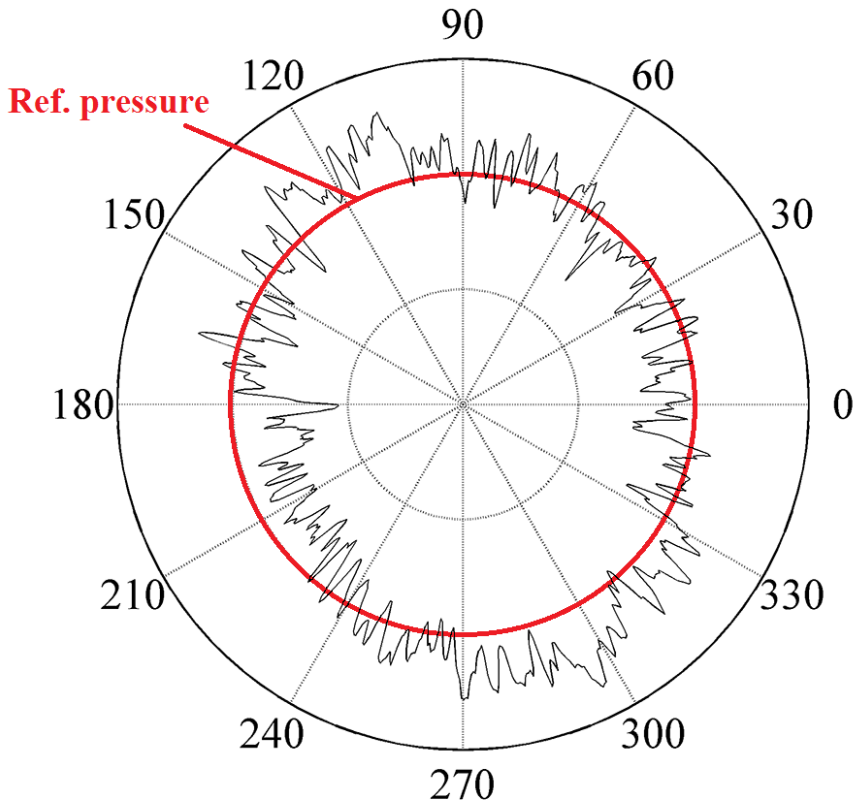

Figure 4-4. Reconstruction of the nearly symmetric two lobes stall pattern at the inlet section of the diffuser.

In order to definitely clarify this aspect related to the identification of the stall shape, a scheme of a two lobes stall is reported in Figure 4-5. The stall is presented as two simple sinusoids of unitary amplitude with a phase shift equal to $\Delta\vartheta = 90°$ which corresponds to a hypothetical geometrical shift between the two probes of $\Delta\alpha = 90°$.

It is worth noticing that if one considers the stall period (*T_stall*) two pressure oscillations corresponding to two lobes are visible and the phase shift is equal to the geometrical one according to Eq. 4-1.

On the other hand, if one wrongly considers the two lobes stall as a single lobe stall (i.e. a frequency two times higher with a period equal to *T_lobe*), the phase shift will no longer satisfy the Eq. 4-2 highlighting a value of $\Delta\vartheta = 180°$ and hence a number of lobes equal to two.

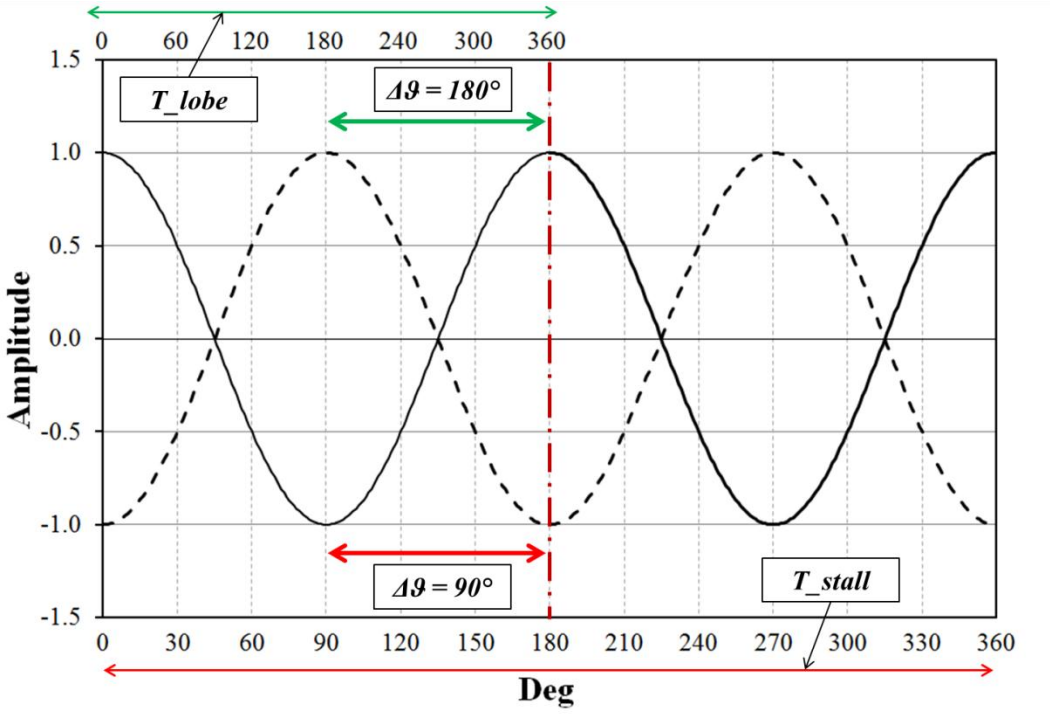

Figure 4-5. Scheme of a two lobes stall recorded by two different probes with $\Delta\alpha = 90°$.

In Figure 4-6 the FFT of a real nearly symmetric three lobes stall is reported; again, due to the slight unbalance of the pressure pattern, the resulting force is very small.

Again, the analysis of the power spectrum can lead to a wrong evaluation of the lobes' number. As shown in Figure 4-6, only a frequency which corresponds to the lobe passage is clearly distinguishable, while the revolution stall frequency is not visible due to the almost perfect equality between the lobes (see Figure 4-7).

As discussed above, the auto-correlation cannot help also in this case to identify the right rotating stall frequency; if one would use this frequency to perform the ensemble average process, a single lobe stall patter would be obtained. The further step of the advanced stall analysis (i.e. the cross-correlation) would reveal a phase shift between two probes that is not in agreement with Eq. 4-1.

So, by applying Eq. 4.2 the real stall pattern can be detected.

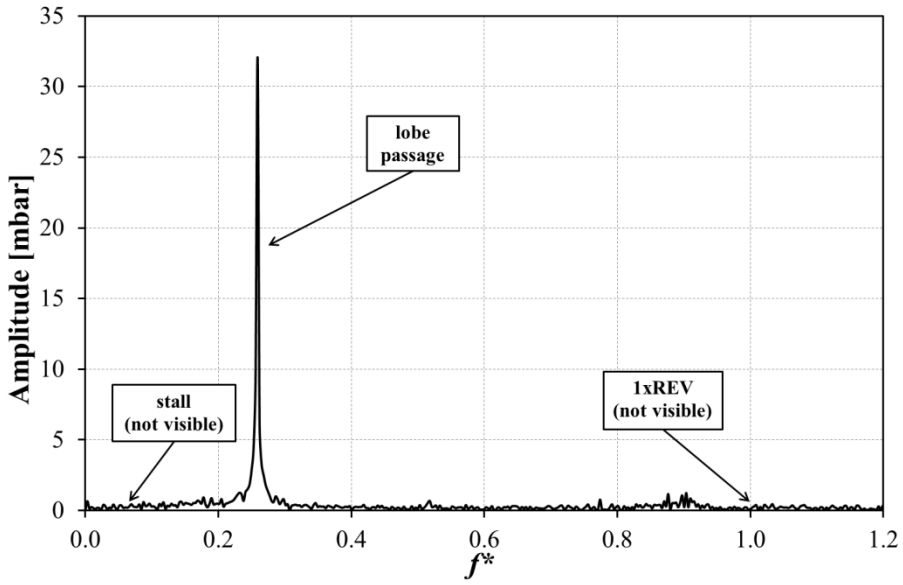

Figure 4-6. FFT analysis of a real nearly symmetric three lobes stall: all the frequencies are presented in a dimensionless form, i.e. $f^*=f/f_{1xREV}$.

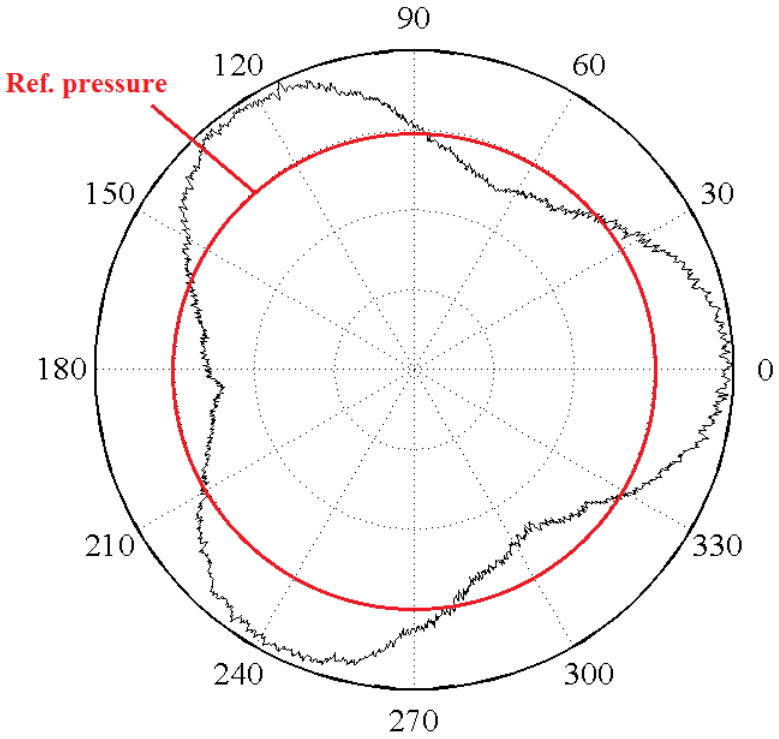

Figure 4-7. Reconstruction of the nearly symmetric three lobes stall pattern at the inlet section of the diffuser.

4.3 Sensors' number and positioning

After this analysis on the stall pattern shape, some considerations on the number of sensors and their relative positioning along the circumferential direction of the diffuser at a certain section can be done.

Based on the systematic procedure described in the previous chapter, a couple of dynamic pressure probes could be sufficient to correctly characterize the stall pattern in the diffuser.

From an industrial point of view, this solution seems to be very attractive both in terms of cost and of limited mechanical problems due to the need to ensure the proper space to the two accesses for the probes. As a result of this consideration, two main aspects have to be discussed. In particular, it is necessary to clarify if:

- Two sensors are sufficient to characterize any typology of rotating stall pattern (basing on the fact that the number of stall cells is not known a priori).
- There is an optimal angular spacing $\Delta\alpha$ between the probes.

In order to answer these questions, one can assume that the pressure oscillation due to the stall can be described as a sinusoidal signal (as shown in Figure 4-5); in other words a purely mathematical approach would definitely ensure that two points of measure are sufficient to describe the pressure pattern shape, despite the uncertainty on possible harmonics.

However, in case of rotating stall reconstruction by using an ensemble average process, an accurate analysis is needed. In particular, if on one hand in case of an unbalanced N lobes stall pattern, two sensors are always sufficient to perform the systematic approach presented in this study, on the other hand, whenever multi-lobed rotating stalls with nearly symmetric lobes occurred, the use of only two sensors could introduce uncertainties in the lobes' number calculation.

In case of symmetric lobes, the sensors' angular spacing must be narrow enough to contain more than one pressure ripple. In other words, two properly positioned probes are anyway able to discriminate between different stall patterns, even if symmetric.

In order to clarify this aspect, some examples are given.

Figure 4-8 shows the time signals theoretically measured by two pressure probes (called A and B) positioned with Δα=90° in case of a single lobe stall rotating at 10 Hz or a symmetric two-lobes stall rotating at 5 Hz, respectively. Upon examination of the Figure 4-8, even if each probe actually senses the same sinusoid in frequency and amplitude in time, the phase difference between the signals is different in the two cases, as the hypothetical patterns are rotating with two different speeds.

In this case, Eq. 4-2 applied at the frequency of the sinusoid will be definitely able to discriminate between the two conditions, even though this specific positioning can anyway produce an uncertainty on the higher harmonics, as will be shown later on in the study.

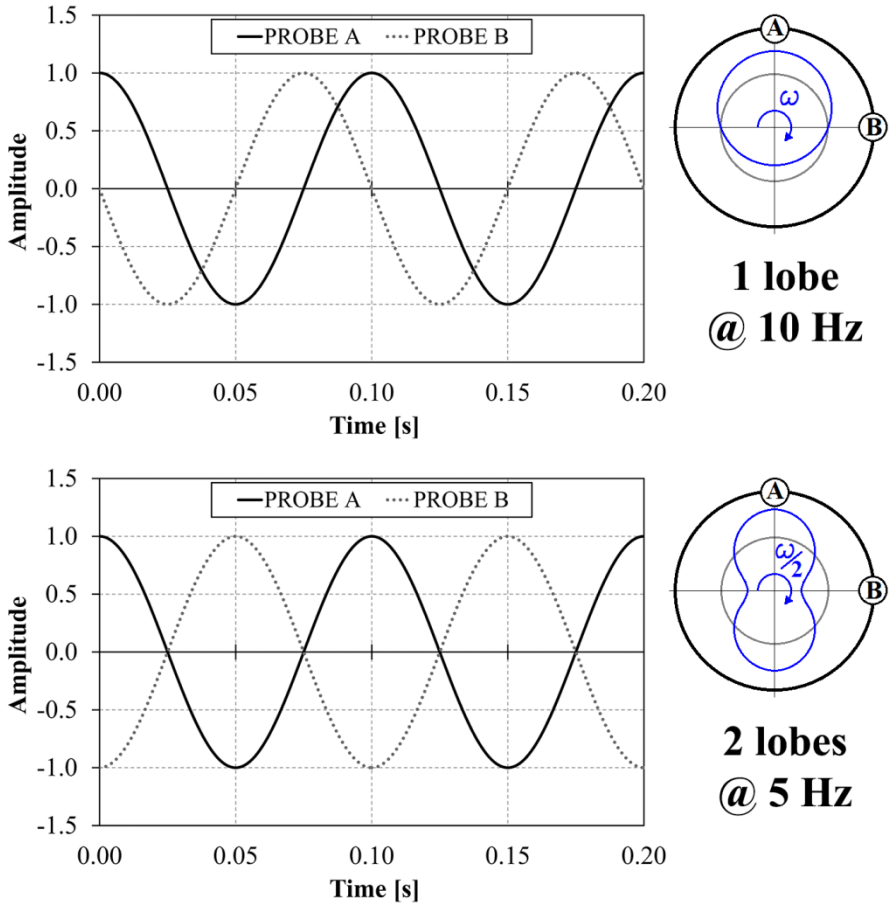

Figure 4-8. Time signals recorded by two probes with Δα=90° in case of a single lobe stall rotating @ 10 Hz or a symmetric two-lobes stall rotating @ 5 Hz.

In particular, the first critical condition is reached if the probes are positioned following Eq.4-3.

$$\Delta\alpha = n\frac{360°}{N} \quad n \in N \qquad \text{Eq. 4-3}$$

Moving from the fact that at least two points must be given within the each period of the sinusoid to ensure a correct reconstruction, this choice would in fact lead to an undefined solution in case of symmetric lobes.

Figure 4-9 shows an example of two time signals recorded by two pressure probes with Δα=180° in case of a two-lobes stall rotating @ 10 Hz or a four-lobes stall rotating @ 5 Hz, respectively.

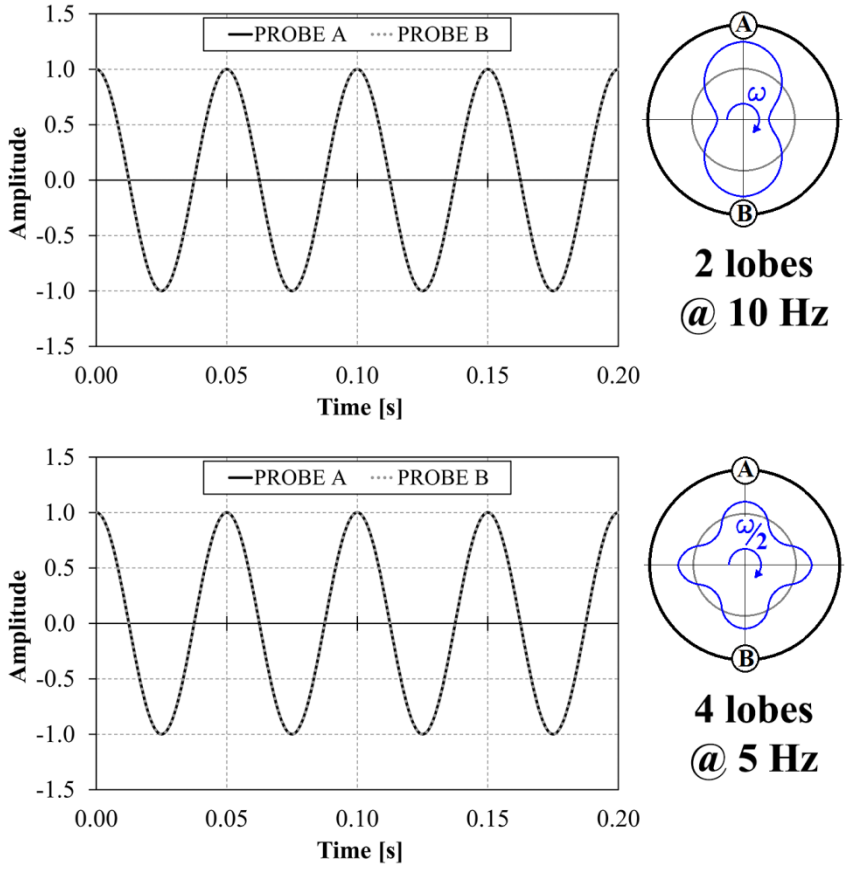

Figure 4-9. Time signals recorded by two probes with Δα=180° in case of a two-lobes stall rotating @ 10 Hz or a four-lobes stall rotating @ 5 Hz.

In this case the cross-correlation function would indicate a null phase, giving no useful information on the lobes' number. The number of stall cells would indeed be indefinitely given by Eq. 4-4.

$$N\big|_{symm\,stall} = n\frac{360°}{\Delta\alpha} \quad n \in \mathrm{N} \qquad \text{Eq. 4-4}$$

Another critical sensors positioning in case of symmetrical lobes is described by Eq. 4-5.

$$\Delta\alpha = n\frac{180°}{N} \quad n \in N \qquad \text{Eq. 4-5}$$

In case the two sensors are positioned following Eq. 4-5, two different scenarios can be attended. If the stall pattern has conventional unsymmetrical lobes, this positioning would indeed allow a very clear identification of the signals by maximizing their phase difference. However, a doubt on the harmonics would again rise as described by Eq. 4-6, if the lobes are symmetric like those presented in Figure 4-10 which reports the time signals recorded of the two pressure probes with $\Delta\alpha=180°$ in case of a single lobe stall rotating @ 10 Hz or a three-lobes stall rotating @ 3.3 Hz, respectively.

$$N\big|_{symm\,stall} = \frac{180°}{\Delta\alpha} + n\frac{360°}{\Delta\alpha} \quad n \in \mathrm{N} \qquad \text{Eq. 4-6}$$

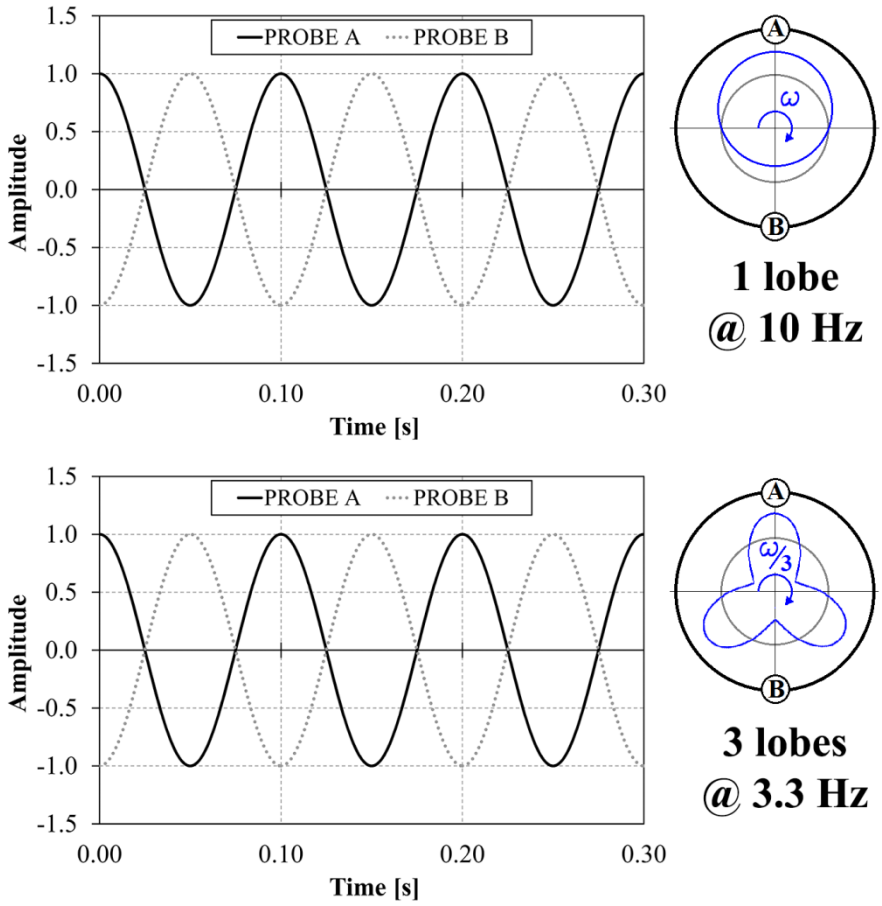

Figure 4-10. Time signals recorded by two probes with Δα=180° in case of a single lobe stall rotating @ 10 Hz or a three-lobes stall rotating @ 3.3 Hz.

It is worth noticing that this positioning would make the two sensors see the same values in time for the two different stall patterns, generating the possibility to detect the wrong frequency of the phenomenon (as the FFT analysis could have hidden the stall frequency).

By summarizing these considerations, one can conclude that even if in the common industrial practice, the symmetrical lobed pressure patterns do not appear frequently, in case only two probes are available, any positioning following Eq. 4-7 would be certainly able to correctly predict a N-lobes stall shape.

$$N < \frac{180°}{\Delta\alpha} \qquad \text{Eq. 4-7}$$

Moreover, an angular spacing between 0° and 60° (if only two sensors are available) could definitely lead to the correct identification of the most usual stall patterns, even if very symmetric. On the other hand, if three (or more) probes are available, the approach can be applied to different couples of sensors ensuring the correct stall reconstruction also in case of many lobes.

4.4 Influence of the working pressure

As discussed in Section 4.1, several experimental data coming from different model test (i.e. single stage configuration) were collected in a dedicated test rig. All these data were hence investigated by using the advanced stall analysis approach; in particular, they were analyzed in order to highlight both the stall characteristics and the influence of some main parameters on the resulting force.

With this goal in mind, several model tests were performed also by varying the pressure at the inlet to investigate on the pressure unbalancing during the rotating stall.

For sake of simplicity, in Figure 4-11 and Figure 4-12 only two model tests analyzed characterized by a single lobe stall were reported; in detail, these stages were tested with several different inlet pressures in order to highlight a possible correlation between the force and the working pressure. In particular, these two model tests were carried out with two different range of working pressure by keeping constant all the other parameters. The test A has been tested with four pressure levels (1, 2, 3, 4 bar), while the test B has only three pressure levels (3, 7, 13 bar).

Upon examination of Figure 4-11, it is worth noticing that the resulting force, calculated by means of the advanced approach presented in Section 3.4, is almost directly proportional to the working pressure. In other words, as the inlet pressure increases (and, consequently, the density increases), the pressure ripple due to the unbalancing of the pressure field during rotating stall increases almost linearly; by doing so, the resulting force calculated with Eq. 3-5 becomes higher while the stall frequency remains constant (see Figure 4-12).

This represents a first important step forward in defining a scaling criterion to predict the resulting force in a multistage compressor operating in on-site conditions (i.e. at higher pressure), as described in the next sections.

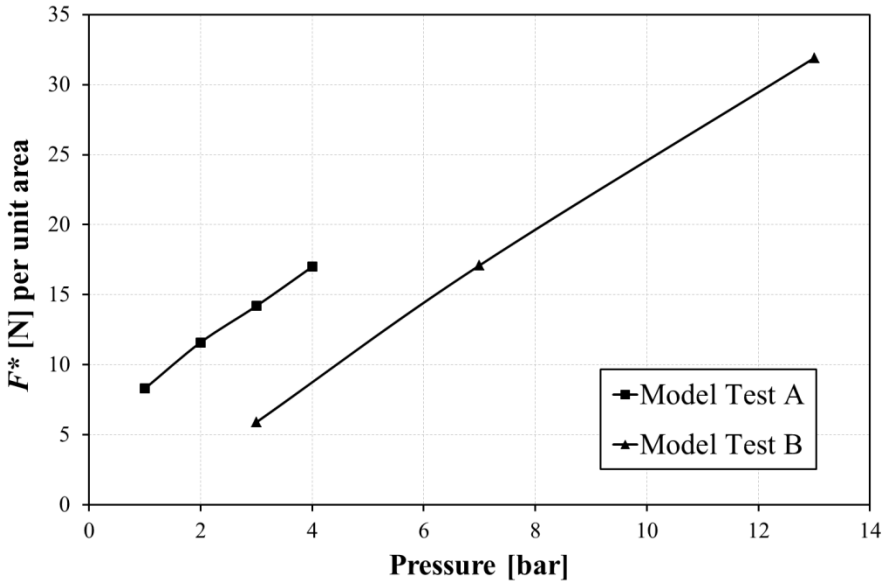

Figure 4-11. Resulting force as a function of the inlet pressure.

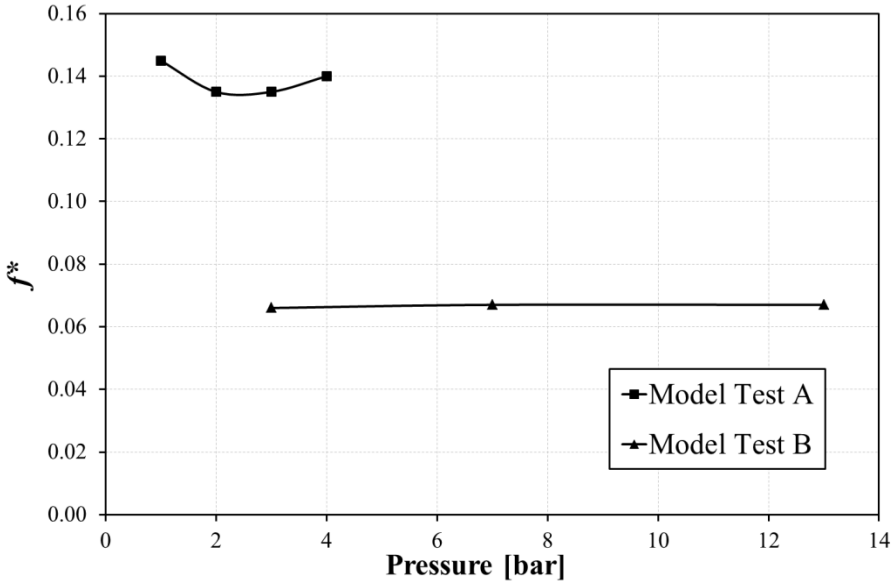

Figure 4-12. Dimensionless stall frequency as a function of the inlet pressure.

4.5 Influence of the Mach number

In order to investigate the influence of the Mach number (*Mu*) on the stall characteristics, several model tests were carried out at different peripheral Mach numbers (i.e. by varying the rotor speed), keeping constant all the other parameters. Generally, all the models were tested at four different speed levels: the design one and three off-design levels.

For sake of clarity, only two model tests characterized by a single lobe stall are again reported in order to gather all the range in term of Mach number. Figure 4-13 and Figure 4-14 show the force (*F**) and the stall frequency (*f**) as a function of the Mach number, respectively.

In Figure 4-13 it is worth noticing that as the Mach number increases, the force value per unit area tends to become higher; obviously, these are only two cases, but a similar behavior was noted in all the tested stages.

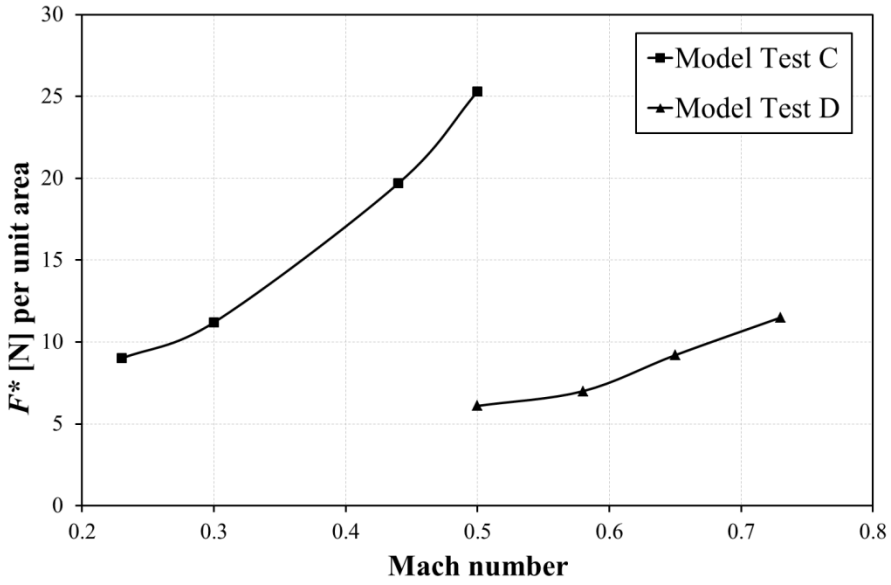

Figure 4-13. Resulting force as a function of the Mach number (*Mu*).

As regards the stall frequency (Figure 4-14), on can readily notice that the ratio of the stall frequency with respect to the 1xREV remains almost constant. On the other

hand, this means that the stall frequency increases its absolute value (i. e. the stall pattern rotates faster).

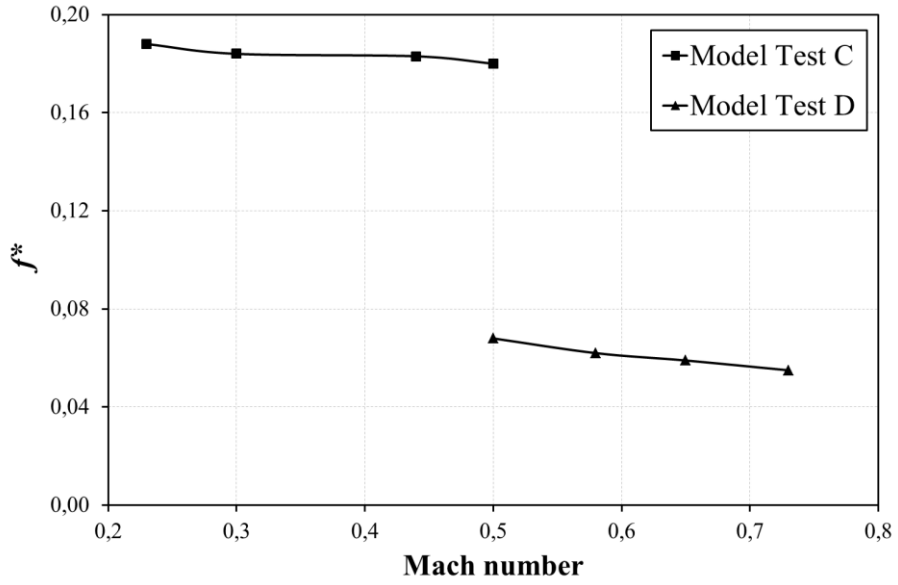

Figure 4-14. Dimensionless stall frequency as a function of the Mach number (*Mu*).

4.6 Database analysis: summary

As discussed in the previous sections, the analysis of the industrial database was carried out by means of the systematic procedure developed during this study, which allowed defining the stall frequency, the rotating force due to the stall and the lobes' number of each available study case for a global amount of more than 60 tests.

The main characteristics of the model tests analyzed are summarized in Table 4.1, highlighting the minimum and the maximum of each parameter, respectively.

Table 4.1 – Main characteristics of the model tests analyzed.

Parameters	Range (min – max)
Mu	0.30 – 1.32
φ	0.0200 – 0.1600
b2/R2	0.05 – 0.15
b2/b4	1.08 – 1.37
R4/R2	1.40 – 1.65
N° blades	15 – 23

In order to obtain a significant result, the procedure was applied in the zone where the stall was clear and completely developed, i.e., the stall frequency was widely the most relevant of the spectrum. By reducing the flow coefficient step by step, the typical behavior of the rotating stall is to quickly increase its intensity up to a final value (the point at which the stall force was calculated) which generally precedes the surge as shown in Figure 4-15. Moreover, it is worth to remark that every point corresponds to a different flow coefficient (i.e., at a different closing step of the throttling valve).

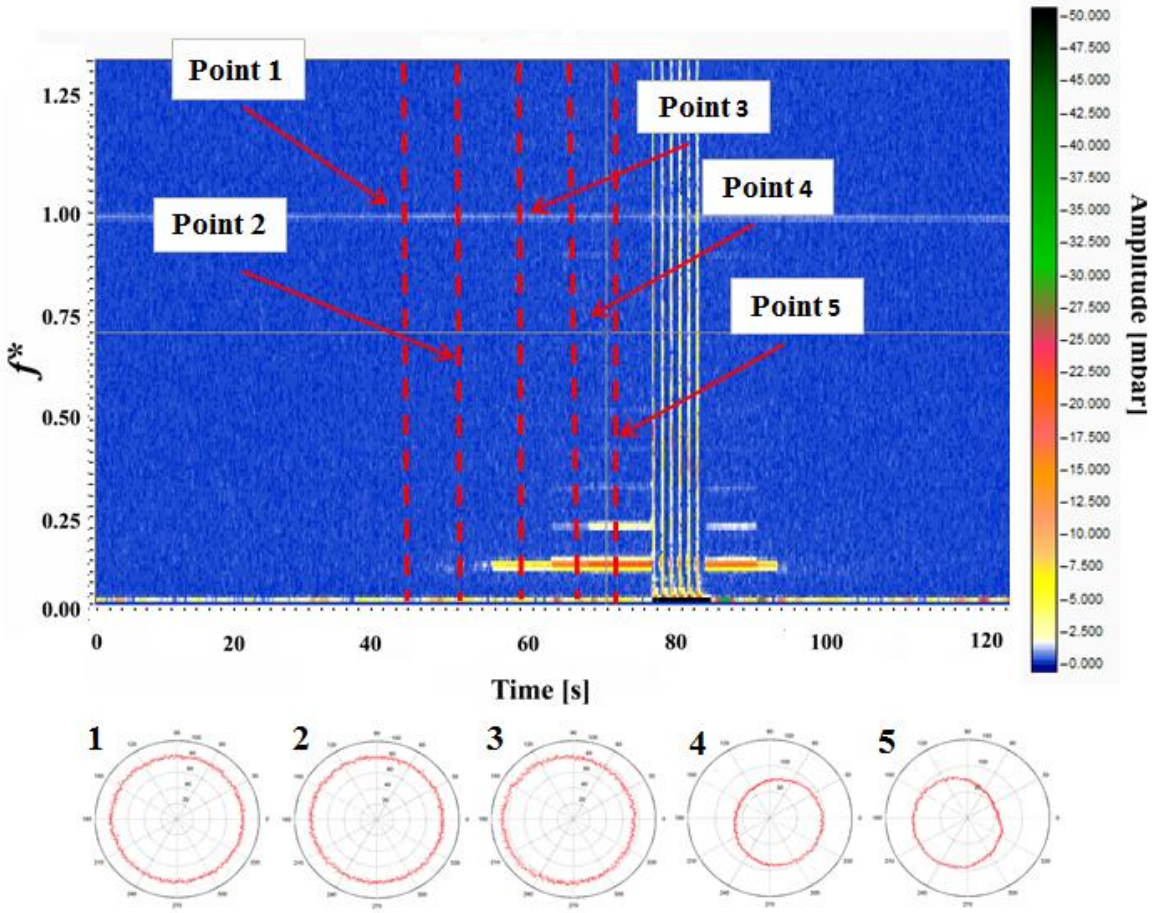

Figure 4-15. Stall force evolution during the closing steps of the throttling valve.

The collected data were categorized by impeller family, geometrical characteristics (i.e. impeller diameter, diffuser width, diffusion ratio) and design performance in order to obtain an exhaustive overview of stall characteristics.

The stall frequency was the first aspect that has been investigated after the analysis was completed. In particular:

- 87% of the model tests analyzed showed a stall frequency in the range 5-20% of the 1xREV.
- Only 13% of the model tests analyzed showed a stall frequency over 20% of the 1xREV up to a maximum of about 80% detected in a specific impeller family with a high flow coefficient.

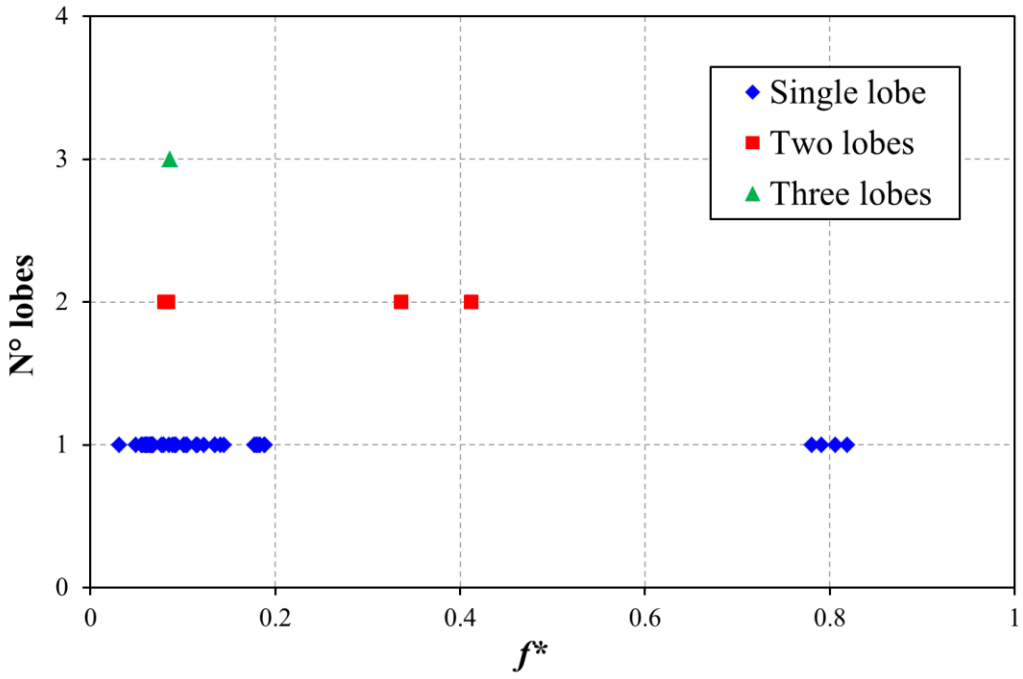

Figure 4-16. Number of lobes as a function of the dimensionless stall frequency.

Moreover, the stall cases were characterized in terms of pressure pattern shape (i.e. lobes' number), which actually represents a key point in the evaluation of the resulting force. Upon examination of the results, it was noticed that:

- The single lobe pattern is by far the most likely configuration, with 89% of the total (see Figure 4-16).
- The multi-lobes stall cases appeared only with a two and three-lobes shape in 9% and 2% of the total tests, respectively. In details, multi-lobes stall cases appeared for higher values of the b2/R2 ratio and low diffusion ratios (R4/R2) than those connected to single lobe stall cases (see Figure 4-17).

Upon examination of these figures, one can conclude that the single lobe configuration is widespread in all the analyzed model tests, while multi-lobes configurations were detected only in so called "wide" diffusers.

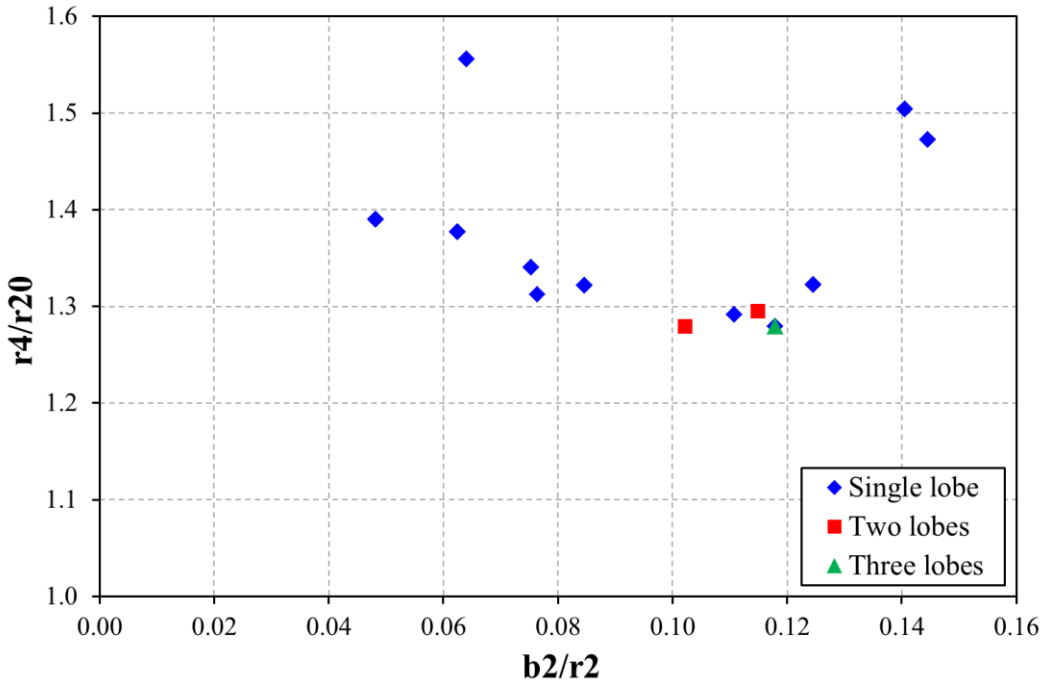

Figure 4-17. Number of lobes as a function of b2/R2 and diffusion ratio (R4/R2).

4.6.1 Dimensionless force coefficient

Furthermore, very relevant information were obtained through the database analysis by referring to the stall force intensity due to the distortion of the pressure field.

In particular, a wide range of force values was measured and no well-marked trend was individuated. Force values cannot be reported due to the non-disclosure agreement with the industrial partner, but, as a general consideration it can be highlighted that for two lobes and three lobes stalls, this force tended to reach very low values due to the partial compensation of the pressure field among each lobe.

In order both to show the results and to compare stages with different geometric characteristics and design points, a dimensionless coefficient was defined, as in Eq. 4-5.

$$\chi = \frac{F_{stall}}{0.5 \cdot \rho_2 \cdot c_2^2 \cdot A_2} \qquad \text{Eq. 4-8}$$

The χ coefficient was defined in order to correlate the stall force with the dynamic pressure and the geometrical characteristics at the exit of the impeller. By doing so, a distribution of measured values of the dimensionless force coefficient can be obtained, as reported in Figure 4-18.

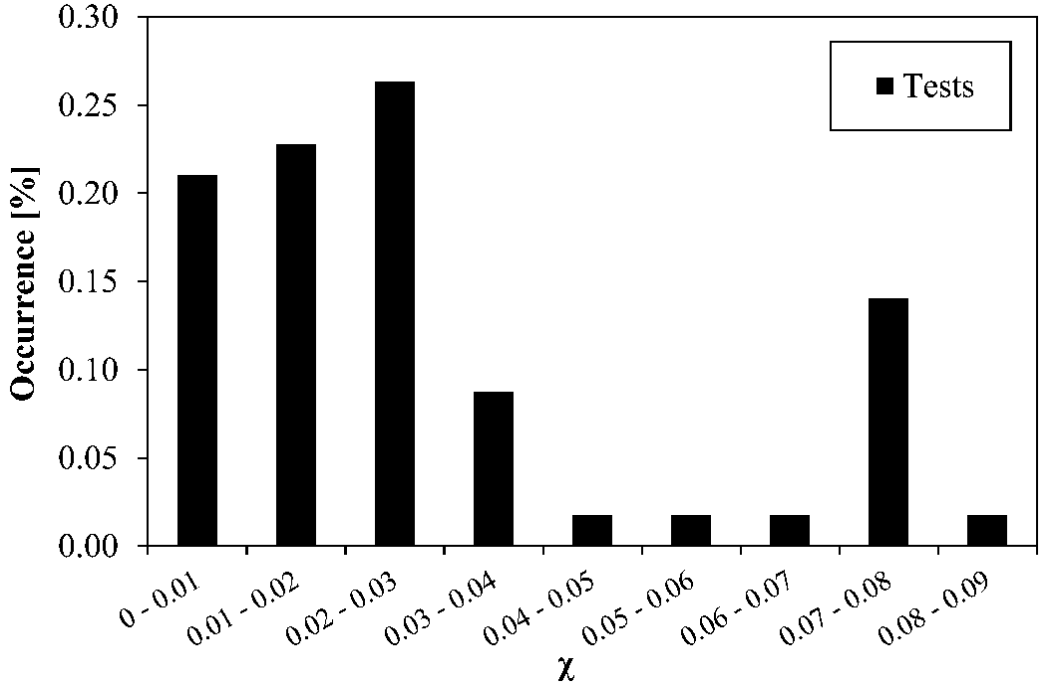

Figure 4-18. Distribution of the dimensionless force coefficient.

By examining Figure 4-18, it is worth pointing out that the largest part of the analyzed model tests (i.e. about 70%) is gathered in the range 0-0.03 and it showed a total average value of 0.029.

In Figure 4-19 is shown the relationship between the χ coefficient of all the model tests analyzed as a function of the stall frequency always reported in a dimensionless form (i.e. $f^* = f/f_{1xREV}$).

The figure clearly highlights that no consistent trend can be identified; however, two distinguishable zones (yellow and red shadowed) can be readily noticed. Some remarks can be done:

- The major part of analyzed stalls is located under the 20% of 1xREV.
- Very intense stalls took place only at low frequencies.

- High frequency stalls were generally characterized by very low exciting forces.
- Multi-lobes stalls showed lower force coefficient.

As a conclusion, both from an industrial and an academic point of view, the analysis of this wide industrial database led to important results in terms of stall characterization and data manipulation. This allowed to obtain an accurate overview on the stall characteristics that currently is not present (or it is limited to some study cases) in open literature. Moreover, as it will be discussed in the next chapter, the characterization of the rotating force due to the pressure unbalancing in the vaneless diffuser allowed also to correlate the unsteady fluid dynamic phenomenon with the rotordynamic behavior of the machine.

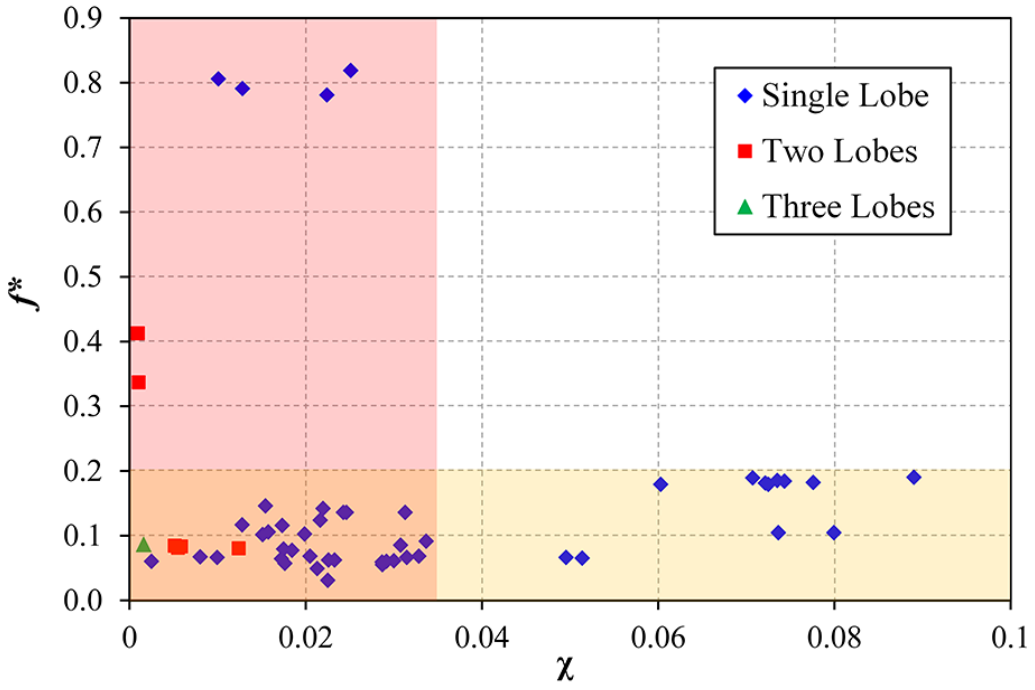

Figure 4-19. Analyzed stall pattern as a function of dimensionless frequency and force coefficient.

Figure 4-20 shows also the behavior of the stall force in terms of dimensionless coefficient as a function of the flow coefficient of the tested models. In particular, due to the non-disclosure agreement with the industrial partner only a flow coefficient range is given:

- LOW range: $\varphi < 0.03$
- MEDIUM range: $0.03 < \varphi < 0.06$
- HIGH range: $\varphi > 0.06$

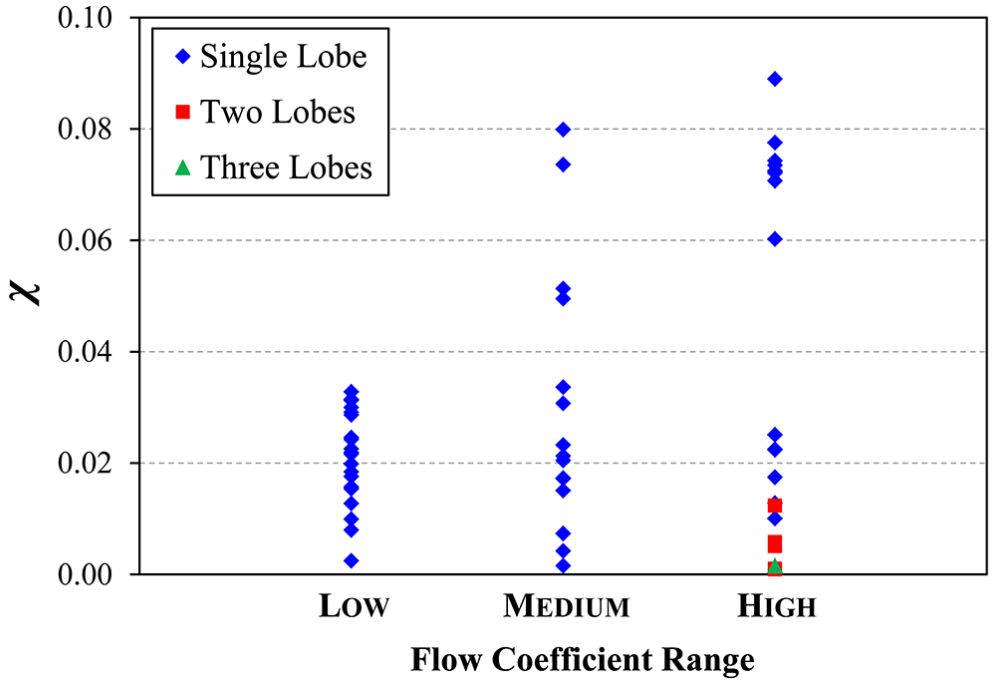

Figure 4-20. Analyzed stall patterns as a function of the flow coefficient range and the force coefficient.

Upon examination of the figure, one can readily notice that well marked trend are not still detected, but, however, it is possible to notice that a general increasing of the force value with the design flow coefficient is present. In addition, the few multi-lobes stall cases are all gathered in the high flow coefficient region.

4.6.2 Scaling criterion

Once the force has been evaluated and characterized in terms of frequency and intensity, a correlation between the model test conditions and the real operating conditions was needed.

In particular, the force intensity was assumed to be dependent on the working pressure of the impeller, the inlet passage section of the vaneless diffuser and the

relative gas velocity fluctuation, as proposed by Colding- Jørgensen [44] [51] and Baldassarre *et al.* [52].

With this goal in mind, moving from the above, a scaling criterion of the stall force was hypothesized. In detail, the scaling criterion was based on the manipulation of the dimensionless coefficient (defined in Eq. 4-5) by introducing different boundary conditions. In other words, once the χ coefficient for a specific impeller family has been evaluated in model test conditions, it is possible to calculate a scaled force value by using the operating conditions (i.e. density, absolute inlet diffuser velocity and passage area) of the multistage compressor (if constituted by impellers coming from the same family).

By doing so, the χ coefficient can be used to scale the resulting force in the model test to the operating conditions.

Once the scaling criterion has been verified, the evaluation of the force in operating condition on a real multistage machine could open a new scenario in which the rotordynamic behavior of the compressor could be predicted a priori in the design phase.

In the next chapter the rotordynamic effects of the rotating stall will be first investigated in model test conditions in order to correlate the aerodynamic stall force with rotor vibrations and then, once the methodology has been definitely assessed, a first attempt at transferring this force into a predicted vibration level of the machine during on-site operating conditions will be presented and discussed.

5. Rotordynamic analysis

5.1 Introduction

The estimation of the rotating stall force could provide a valuable contribution in quantifying the risk of onset of subsynchronous vibrations of significant amplitude in the contractual operating range of the compressor.

With this in mind, an investigation on the impact of the aerodynamic phenomenon to the rotordynamic performance was carried out.

By using the systematic approach developed in this study, it is possible to estimate the resultant of the pressure field distortion during the stall, in terms of amplitude and frequency. Furthermore, the analyzed experimental tests provided also the vibration level on the rotor bearings which allowed one to have a first check on the correlation between the rotating force and the rotordynamic response of the system.

The purpose of this second part of the work was first to verify this correlation by comparing the experimental data with the response obtained by imposing in a rotordynamic model of the rig the calculated force and then to develop a tool able to predict the rotordynamic behavior of a real compressor in unsteady conditions, i.e. in case of rotating stall. In order to develop and to verify this rotordynamic procedure, the first step was to include the calculated force in a rotordynamic model of the model test rig used to obtain all the experimental data of this work. Then, once the

procedure has been assessed, the approach was applied to several real multistage compressors operating both on test and on-site conditions.

Finally, in order to highlight the potential, the prospects of the proposed approach will be discussed by showing some examples.

5.2 Rotordynamic modeling

Several model tests were analyzed from a rotordynamic point of view by means of a specific code commonly used by the industrial partner.

However, for sake of clarity, the procedure to investigate on the rotordynamic behavior of the compressor in stall conditions will be presented by showing only a case study. In particular, the selected case refers to that one used to present the advanced approach to estimate the rotating force due to the stall (see Section (3.4) for further details).

As aforementioned, the first step was to verify if the calculated force in model test conditions could be coherent with the vibrations measured by specific sensors positioned near the rotor bearings; to do this, as a first step, the rotordynamic model of the model test rig was developed with a numerical code based on a finite element approach [53].

The schematization of the model is shown in Figure 5-1, coupled with the mechanical drawing of the rotor chosen as a case study.

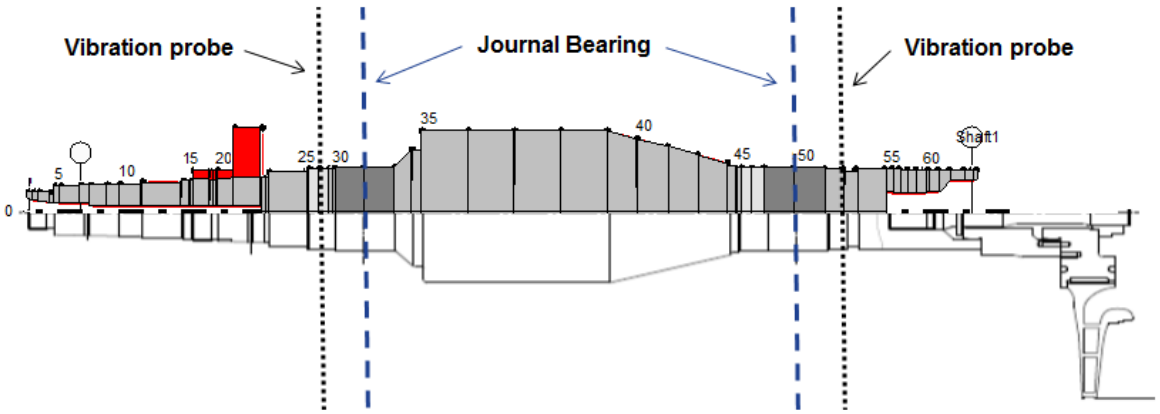

Figure 5-1. Schematization of the rotor model and relative drawing

Upon examination of the figure, some of the main rotor features can be readily noticed:

- Overhung design: the test impeller was installed at the shaft end and modeled as lumped mass and inertia (including the hub and tie-rod contributions).
- Rigid rotor design: the running speed is lower than the first critical speed; the response in terms of vibrations level will be quite constant.
- Journal bearings and axial vibration probe's locations.

After the model has been built, the calculated aerodynamic force was applied to the rotordynamic model (e.g., see Ref. [54]).

Thanks to the asynchronous response module available in the software, it was then possible to model the forced response under the aerodynamic excitation. Differently from the more conventional study case of rotor imbalance, this module allowed one to calculate the behavior of the rotor under an external load which was not synchronized with the rotational speed of the impeller.

A constant force value of 9.8 N rotating at 10.5% of 1xREV was calculated for the selected case; the external excitation was hence modeled as rotating load with a constant amplitude and frequency and applied in correspondence with the bi-dimensional impeller. Moreover, in order to have a sensitivity analysis with respect to the frequency, the range between 0 and 17% of 1xREV was investigated.

The steady state response of the system was computed in correspondence of both the journal bearings at each frequency; however, the journal bearing closer to the impeller was deemed to be the critical one in term of vibrations level. Finally, a frequency response function was defined.

The results obtained by the simulation were then compared to the experimental data of the vibration probe in the same location.

A comparison between the experimental data and the predicted ones is reported in Figure 5-2 for t = 71 s (i.e., the center of the analysis window showed before). The results are presented as a function both of the dimensionless amplitude of the vibration (i.e., the vibration divided by the maximum measured value) and of the dimensionless frequency, in order to preserve the non-disclosure agreement with the industrial partner.

As regard the experimental data, it is worth noticing that in the case analyzed the power spectrum appeared very well defined showing only a low noise level and a clear peak located in correspondence with the stall frequency.

A good agreement can be noted between the experimental value and the predicted one in terms of displacement amplitude. Several checks were performed by using the described procedure to investigate the correlation between rotating stall and the rotordynamic behavior of the system.

However, this represents the first confirmation that the advanced approach to estimate the stall force correctly extrapolates the force value in stall condition. Furthermore, this could represent the basis to define a new acceptability criterion in which it is possible to know a priori if subsynchronous vibrations induced by the rotating stall could be a problem for the machine vibrational response.

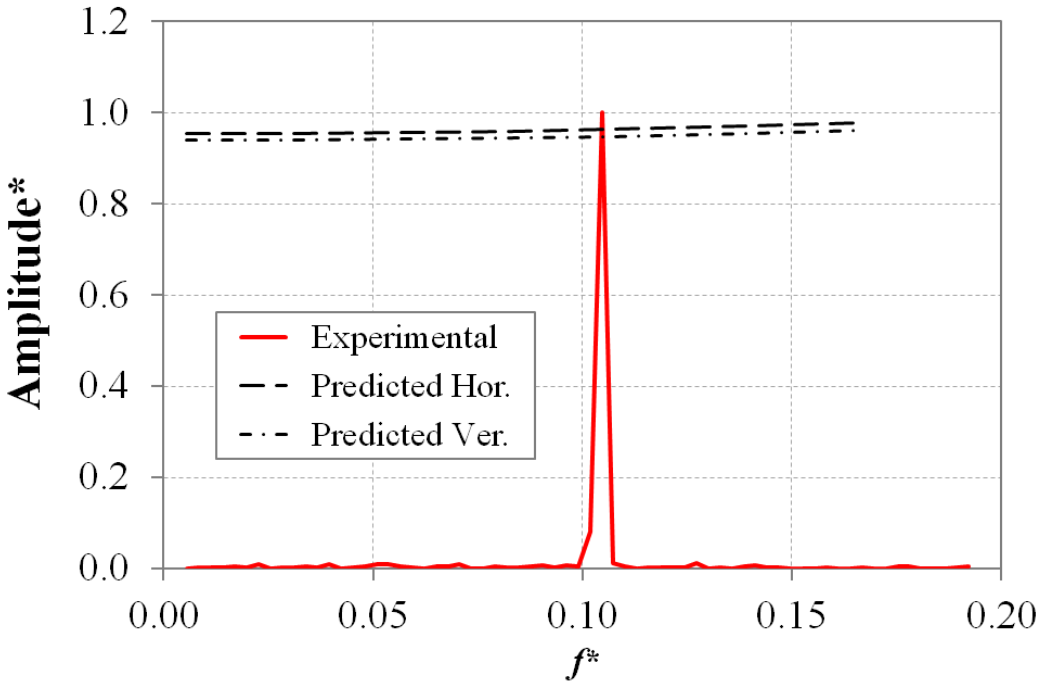

Figure 5-2. Comparison between the power spectrum of the vibration probe near the impeller and the predicted value.

5.3 Rotordynamic analysis on multistage compressors

In order to verify the developed approach by repeating the previous described procedure in the real operating conditions of a compressor, two real multistage centrifugal compressors were selected and tested in a dedicated test-rig of the industrial partner. The test procedure was comparable to that used for the model tests, i.e., starting from the overflow condition to the surge condition by using a regulation throttling valve closed step-by-step. In particular, the rotating stall force was assumed to be dependent on the working pressure of the impeller, the gas velocity and the inlet passage section of the diffuser, and a scaling criterion was hypothesized as described in Section (4.6.2).

Before showing the results of this analysis an important remark must be done: all of the impellers that constituted the two compressor trains belonged to the same family of the one tested at the model test-rig (and used to set up the approach presented in Section (5.2)) and were compatible in terms of geometrical design, outer diameter, peripheral Mach number and flow coefficient. Within this context, a coherent stall mechanism (with respect to that one detected in the model test) was hence hypothesized for the two multistage compressors (i.e., single lobe stall).

Multistage Compressor A

The first multistage compressor had five stages: in particular, the last stage of the train (Figure 5-3) was deemed to be the critical one in the design phase based on the performance simulation tool commonly used by the industrial partner (i.e., the stage which first reaches the stall condition).

Figure 5-3. Cross-section of Multistage Compressor A

As a first step, the attended force in a standard performance test (ASME PTC10 - Type 2 test) was predicted, since this type of test was already part of the standard compressor manufacturing and testing processes: in this case the inlet pressure and the delivery pressure were 3 bar and 10 bar respectively.

Based on these working conditions, a force of approximately 20 N was predicted by using Eq.4-5. As a further confirmation, the test showed a subsynchronous frequency of about 10% of 1xREV which was considered coherent with that one detected in the relative model test (i.e., the model test used to describe the advanced approach; for further details, see Section (3.4.3)).

The compressor's rotordynamic model was realized using the same software applied to the rig modeling [53] and the relevant frequency response was calculated using the same methodology, i.e. by applying a force of 20 N rotating at 10% of 1xREV.

Since the journal bearing stiffness of this compressor was high (around 1×10^8 N/m at the test speed), very low vibrations were predicted despite the increased force value with respect to the model test: in particular, about 0.12 μm peak-to-peak was estimated.

During the experimental test on this first machine the radial vibrations were constantly monitored with the same type of displacement probes; the results showed that the measured vibration levels, obviously in the investigated frequency range, were, again, coherent with the predicted values.

However, due to the base noise introduced by a real functioning multistage compressor, the results of the power spectra did not show a well-defined frequency as obtained for the model test; as a consequence, no conclusive answers on the validity of the approach were found.

Multistage Compressor B

The second multistage compressor had four stages: in particular, the last one of the train was deemed to be the critical for rotating stall by the same industrial simulation tool (Figure 5-4). Again, the impeller of this stage belonged to the same family as that used in the previous model test but it operated at a lower design peripheral Mach number equal to 0.81 and a different flow coefficient.

Figure 5-4. Cross-section of Multistage Compressor B

This stage was however tested also at the model test-rig with the same procedure and instrumentation previously described: in particular, in this case, the model test showed a stall frequency of about 7% of 1xREV and an overall force of 7.8 N.

The multistage compressor was tested in a closed-loop configuration operating with R134a as a working gas. In detail, the inlet pressure and the discharge pressure were 0.7 bar and 7.25 bar respectively.

In Figure 5-5 the results of the test on this multistage compressor are shown: the measured vibrations are reported in the *z* axis as a function of the dimensionless frequency (*x* axis) and time (*y* axis).

From a perusal of the graph, one can readily notice that the 1xREV frequency is clearly distinguishable during the whole test. Moreover, once the instability condition occurred, a well-marked subsynchronous frequency appeared together with some harmonics exactly at the determined critical flow coefficient for the fourth stage and at a frequency coherent with that one detected in the model test.

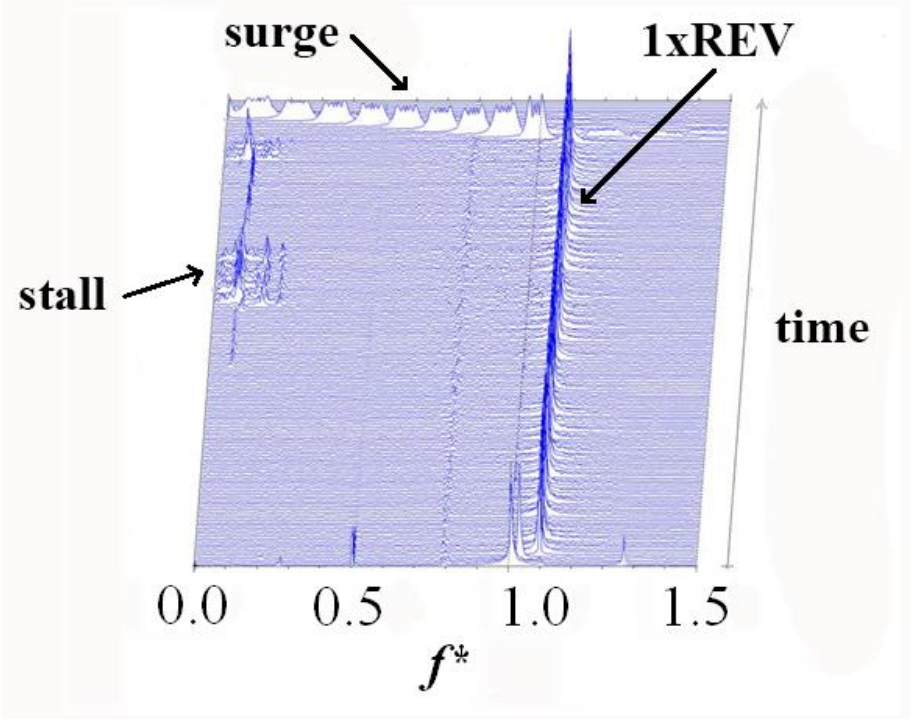

Figure 5-5. Measured vibrations of the multistage compressor during the stall.

At the same time, based on the scaling criterion, a force of 65 N rotating at 7% was hypothesized for the fourth stage of the compressor in case of rotating stall.

In order to compare the experimental vibrations with those predicted, a rotordynamic simulation was carried out by using the estimated stall force (further details on the rotordynamic modeling of a multistage compressor will be presented later on in this chapter).

The vibration level on the fully developed subsynchronous phenomenon was finally compared: in Figure 5-6, the comparison between the experimental and the simulation results is reported in a dimensionless form (i.e., the vibration divided by the maximum measured value) in order to preserve the non-disclosure agreement with the industrial partner.

In this case, a good agreement can be noticed between the results, both in terms of the stall frequency and modulus of the relative vibrations. Based on the previous findings, this can be considered as a first important validation of the proposed rotordynamic approach. However, future works will be devoted to increase the test population and quantifying the reliability of the estimations; in the following sections will be investigated the potential and the sensibility of the approach.

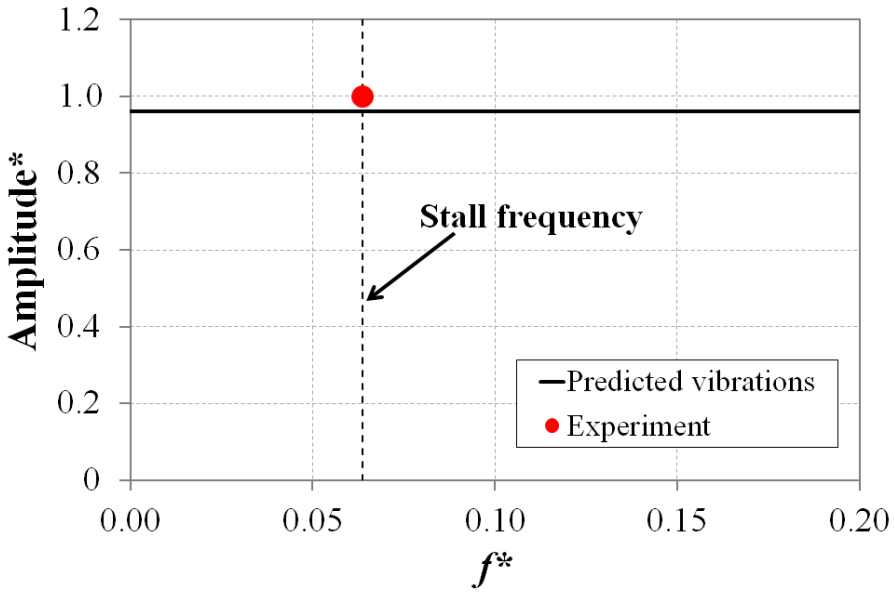

Figure 5-6. Comparison between the predicted and the experimental vibrations.

For sake of clarity, in Table 5.1 are reported the main characteristics of the two multistage compressors.

Table 5.1 –Multistage compressors characteristics.

Multistage compressor	A	B
N° stages	5	4
Inlet-outlet pressure [bar]	3-10	0.7-7.25
Mu	0.5	0.81
φ	0.0300	0.0310
Estimated Stall Force [N]	20	65
Dimensionless Stall frequency [f*]	10%	7%
Bearing Stiffness [N/m]	~1x108	~1x107

5.4 Prospects of the approach

In order to show some possible applications, once the approach has been investigated on its validity with the previous tests and models, a sensitivity analysis on its potential has been started.

To do this, the response both of a real machine in high pressure functioning and of a model test has been investigated by varying some important input parameters; in particular, the two real multistage compressors have been studied with different journal bearings (i.e., variation of the bearing's rigidity), different external excitation (i.e., different rotating stall force in terms of amplitude, frequency and bearings characteristics), respectively.

5.4.1 Bearing's choice in on-site conditions

By using the rotordynamic model of the first multistage compressor presented in the previous Section (5.3), the approach was extended to the real operating conditions of the compressor, which was designed to operate between 30 and 100 bar; in particular, at the inlet of the critical stage (the 5^{th} out of 5) a pressure of 63 bar was expected. In these conditions, a scaled stall force of 1 kN rotating at the same frequency (about 10% of 1xREV) was obtained by applying the developed scaling criterion of Eq. 4-5.

As shown in Figure 5-7, the rotordynamic simulation showed a predicted vibration of about 3 μm peak-to-peak at the stall frequency. Upon examination of the figure, one can readily notice that the response of the system in term of vibration amplitude has an almost linear trend due to position of the first critical frequency of the rotor which is far enough from the external excitation (i.e., the rotating force).

These predicted vibrations would be low enough to allow the compressor to also operate trouble-free in this condition. This vibration entity was however expected since this compressor was designed with a traditional rotordynamic concept, which consisted in two oil journal bearings thought to be stiff enough to contain similar excitations.

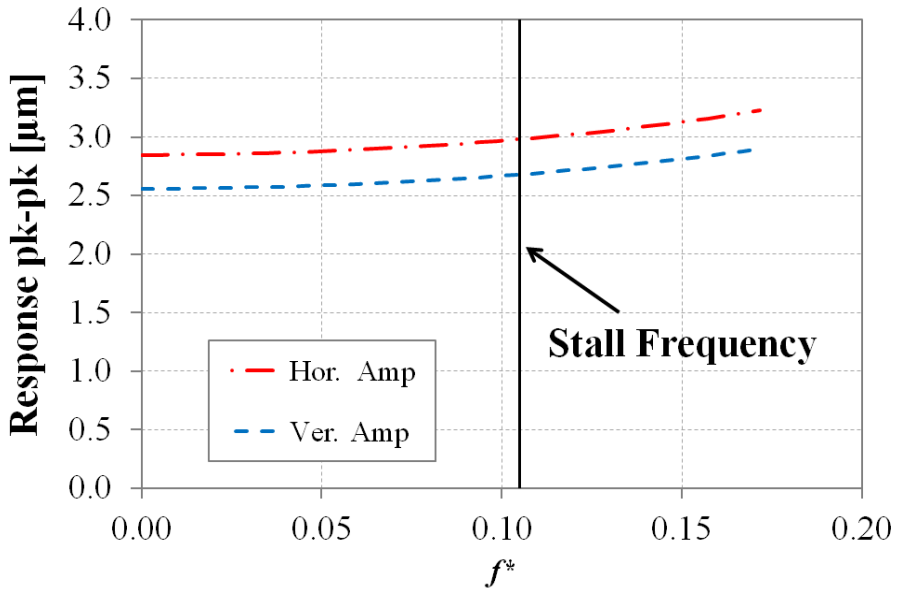

Figure 5-7. Predicted vibrations in the real multistage compressor in on-site operating conditions at the nearest bearing to the stalling impeller with conventional journal bearings.

It is worth noticing that, since centrifugal compressor design is currently moving towards alternative journal solutions having lower stiffness level but higher performance, the proposed tool to evaluate the rotordynamic behavior of a whole machine could provide some useful information in predicting the effects of different rotordynamic solutions when near-stall operating conditions are reached.

In order to investigate on this aspect, the use of squeeze film dampers (SFDs) in the same machine was hypothesized. In particular the SFDs are a powerful device which allows to increase the rotor damping by providing a low stiffness level of the supports to maximize the oil damping effect [55]; as a reference value, the logarithmic decrement of the rotor first mode is increased from 0.28 to 0.99, according to an API617 level 2 stability analysis when SFDs are adopted [56].

Figure 5-8 shows the results of this alternative bearing configuration: they are thought to be a representative example of the prospects of the proposed approach. In particular, it is worth noticing that the estimated stall force of 1 kN produced a significantly higher vibration level, which in this case reached at the stall frequency

an amplitude of approximately 14 μm peak-to-peak, 4.7 times higher than that obtained with conventional journal bearings.

Moreover, in the case where low stiffness supports are selected for the compressors (e.g. in order to improve the damping performance of the whole system near the critical frequencies), higher vibrations will be expected far from the rotor natural frequencies (where the increased damping is really effective), especially in the low-frequency region where aerodynamic unsteady excitations usually occur. On this basis, it is clear that, even further validations are required, the proposed approach could provide a useful tool to the centrifugal compressor designer to predict the potential rotor vibration levels due to the diffuser rotating stall.

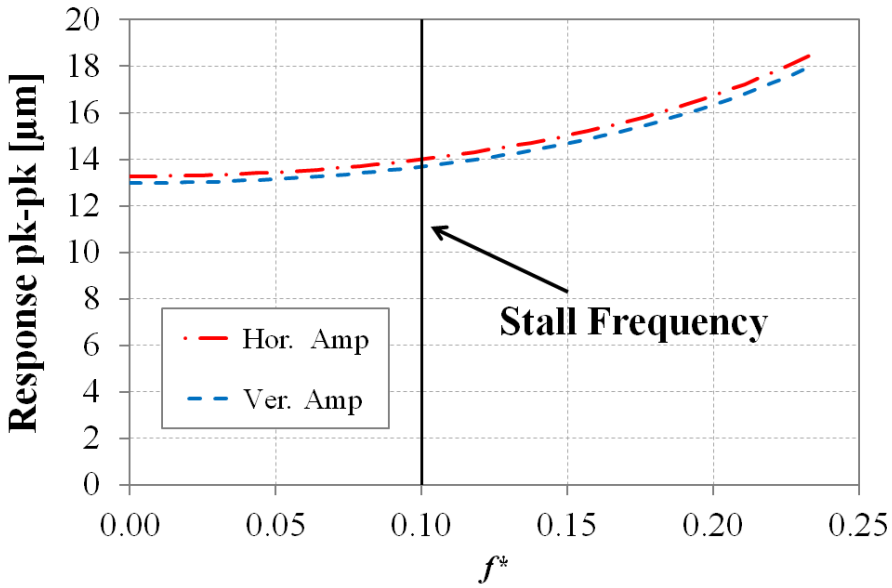

Figure 5-8. Predicted vibrations in the real multistage compressor in on-site operating conditions at the nearest bearing to the stalling impeller with SFDs.

In order to confirm and verify the influence of the journal bearing rigidity on the centrifugal compressor behavior in case of rotating stall functioning, a model test has been analyzed in two different configurations which differed only for the oil bearing temperature (i.e., the rigidity). In particular, the single stage was equipped with standard instrumentations and tested in the intermediate configuration (for further details, please refer to Figure 3-4); the bearing equipment consisted in common oil

journal bearings in which the temperature has been increased to reduce the oil density and consequently the bearing's rigidity.

In Table 5.2 the main characteristics of the model test are summarized.

Table 5.2 –Model test characteristics: oil bearing temperature variation.

Model Test	Values
φ	0.0069
Inlet pressure [bar]	10
Mu	0.73
Low Temp.	58°C
High Temp.	84°C

Figure 5-9 and Figure 5-10 show the vertical and the horizontal vibrations (in a dimensionless form, i.e., divided by the maximum amplitude) recorded by the bearing's sensors from the stall inception to the claimed stall, respectively.

Upon examination of the figures one can readily notice that the bearing's rigidity influences the rotordynamic behavior especially during the stall where an external load acts directly on the rotor at a subsynchronous frequency. By analyzing this aspect in depth, specific control logistics could be developed and consequently the supports' stiffness could be adjusted in order to mitigate the stall effects.

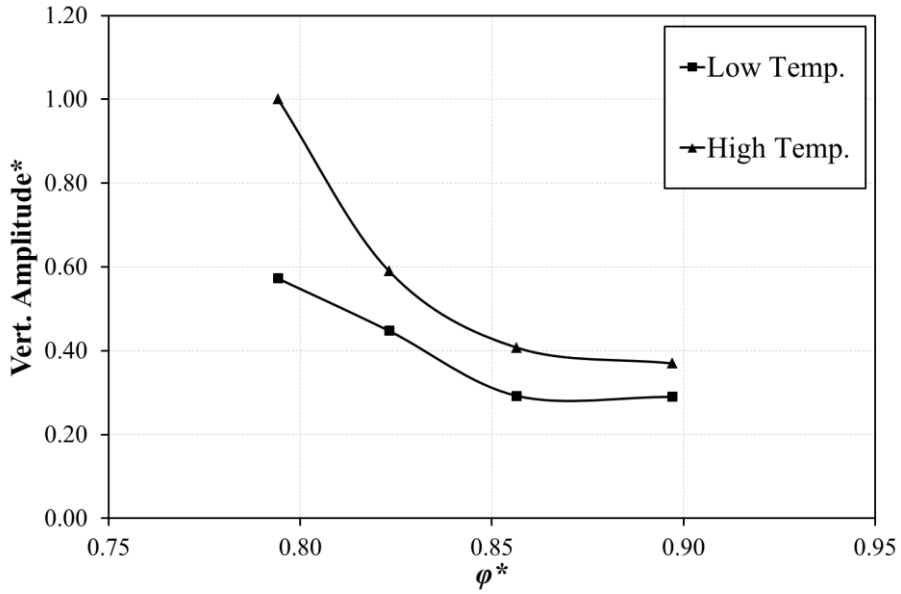

Figure 5-9. Vertical displacements as a function of dimensionless flow coefficient.

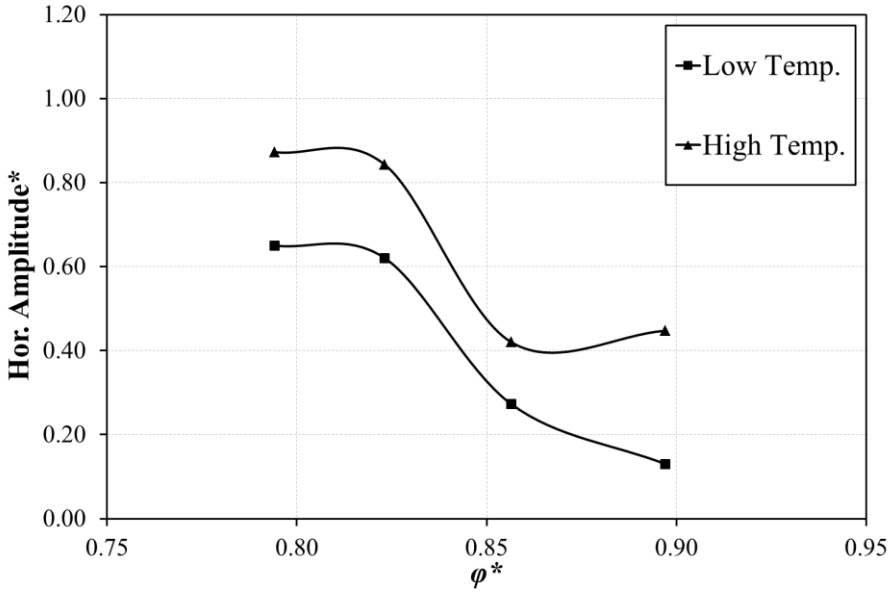

Figure 5-10. Horizontal displacements as a function of dimensionless flow coefficient.

5.4.2 Mechanical limit analysis

In order to introduce the analysis of the effects of the rotating force on the rotordynamic behavior of the compressor, some remarks must be done. This complex

unsteady phenomenon, named rotating stall, as widely discussed, generally precedes the surge and establish the left limit of the operating curve; this produces both a decrease of the stage performance and subsynchronous vibrations to the rotor.

In detail, in common industrial practice, the most restrictive of these two effects defines the last acceptable point of the performance curve.

In particular, the first criterion relates to the slope of the head coefficient ($\eta\tau_p$) curve and it can be considered as a sort of system stability limit; the second one is more connected mechanical issues but in some cases it could not directly translate in a limitation of the operability of the compressor.

Furthermore, the wide experimental database presented in Chapter (4.), highlighted some important aspects; in particular, it is worth remarking that a non-negligible number of the considered model tests pointed out a stall inception according to the mechanical criterion, i.e. in several cases rotating stall appeared before the slope cancellation of the head curve.

As previously discussed, an accurate estimation of the rotating stall force would allow one to identify if rotating stall effects could represent a problem for the rotordynamic response of the compressor.

With this in mind, an investigation of the rotordynamic behavior of the machine by further reducing the flow rate beyond the mechanical limit up to reach the thermodynamic one could be interesting. In other words, a rotordynamic analysis in stall conditions could provide useful information to extend the left margin.

In Figure 5-11, the head coefficient curve of one of the model test analyzed is reported.

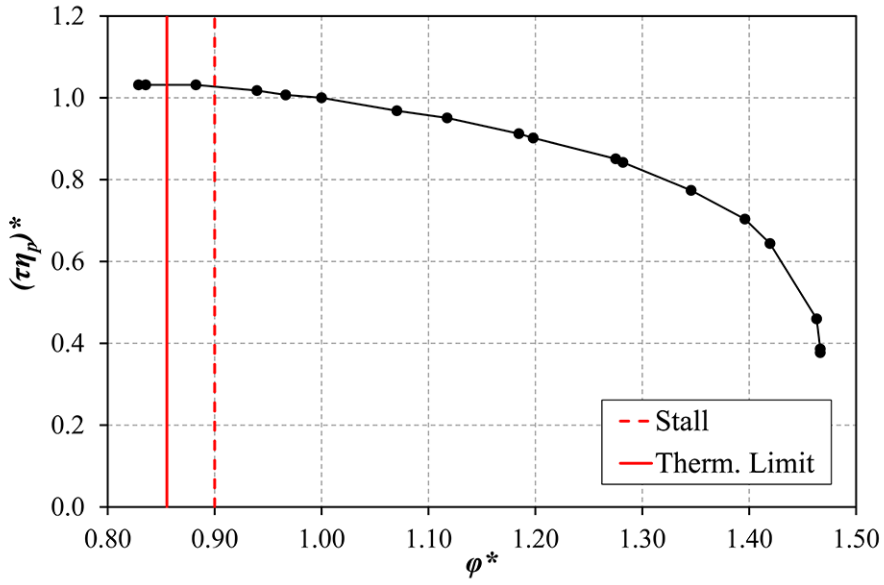

Figure 5-11. Dimensionless head coefficient vs. dimensionless flow coefficient (i.e. $\varphi^*=\varphi/\varphi_{des}$) for a tested stage.

Upon examination of the figure, one can readily notice that the curve definition based on the stall onset would notably limit the curve even if the machine maintains its thermodynamic stability.

After the investigation on the industrial database, a reliable estimation of the expected exciting forces due to rotating stall was obtained.

On these bases, the aim of this part of the rotordynamic analysis was to investigate the effects of similar forces on the rotordynamic behavior of a real compressor operating at on-site conditions (i.e., working pressure and speed) in case the rotating stall occurs before the thermodynamic limit, i.e. where the head coefficient slope becomes negative.

In particular, the main purpose of this analysis was to verify if a left margin extension in the stall zone could represent a feasible solution in case the subsynchronous vibrations due to the rotating stall are below the acceptability limit.

Moving from these considerations, the second real multistage compressor analyzed in Section (5.3) was first selected as a case study. In details, the machine was composed by four stages designed to operate (in on-site conditions) with natural gas between an inlet pressure of 6.6 bar and a discharge pressure of 29.3 bar.

As previously reported, experimental measurements and numerical model assigned to the fourth stage the role of critical one (i.e., the first to reach the rotating stall conditions).

Within this context, this compressor was used to investigate on the rotordynamic effects of a different rotating stall force in terms of intensity and frequency with respect to 1xREV by performing rotordynamic models.

By analyzing the database, it was possible to identify some value of interest for the dimensionless parameters (χ and f^*) that were then properly scaled to the operating conditions of the machine. Moreover, in Table 5.3 the extreme clearance/preload values of the journal bearings together with oil inlet temperature range to be considered in the analysis are also reported; this aspect is of crucial importance for exploring all the tolerance range during the design phase (according to API617 7th ed. [56]) to cover the minimum (MIN) and maximum (MAX) stiffness conditions, which correspond to the opposite levels of both the aforementioned variables.

The combinations of the parameters showed in Table 5.3 provided a set of stall forces that were then applied to the rotordynamic model of the compressor; this allowed to obtain the response in terms of maximum vibrations at the bearings.

In order to investigate on a hypothetical operation during the rotating stall, the results were compared to maximum acceptable values, highlighting the limit conditions.

As a reference, the maximum allowable total vibration level (A_{limit}) was set to 25μm peak to peak and the maximum allowable subsynchronous vibration level (due to the rotating stall) was set to 20% A_{limit}: 5 μm peak to peak according again to API617 7th ed. [56].

Table 5.3 – Sensitivity study parameters.

Parameter	Analyzed values	
Dimensionless Stall Frequency (f^*)	(0.01 - 1.00) f_{1xREV}	
Dimensionless Force Coefficient (χ)	.005 - .020 - .035 - .075	
Stiffness levels	**MIN**	**MAX**
✓ Bearing clearance/preload	max	min
✓ Oil inlet temperature	max	min

5.4.3 Modeling and results

The rotordynamic model of the whole compressor was again assessed by the numerical code used before which is based on a finite elements approach [53].

In Figure 5-12 the schematization of the compressor by means of the code is reported, coupled with the mechanical drawing of the rotor.

Upon examination of the figure, some remarks can be done:

- "Beam Rotor" design: the rotor in object is typical of a multistage compressor where the impellers are located between the journal bearings;
- All the elements re in color have both stiffness and inertia properties while the green in color elements have inertia property only.
- Each impeller is modeled mainly in terms of inertia (the relevant lumped mass placed in the center of gravity);
- As regards the other main items, flexible coupling is modeled as a lumped mass placed in the relevant center of gravity, thrust collar, balance piston and dry gas seals are modeled by means of real geometry as inertial elements.
- Journal bearings position is clearly indicated: they are hydrodynamic tilting pas type bearings and they are modeled through a pair of stiffness and damping matrices. Synchronous reduced coefficients are computed through

a numerical code capable to take into account also pad pivot flexibility and pad thermal-mechanical deformations [57].

- Internal seals locations are identified. The seals effects can be accounted for through the relevant dynamic coefficients. For laby seals the code described in [58] was used, while in case of a honeycomb seal the relevant code of Ref. [59] was adopted. The seals coefficients are usually taken into account when the rotor damping is of primary interest. In this case, in which a forced response analysis id performed at full load condition, they could be important for the stability of the compressor. However, if only labyrinth seals are present, the effects of the rotating force are negligible with respect to the journal bearings contribution in the low frequency region, while near the rotor natural frequency, the seals can reduce the system damping, as will be discuss later on in this study.

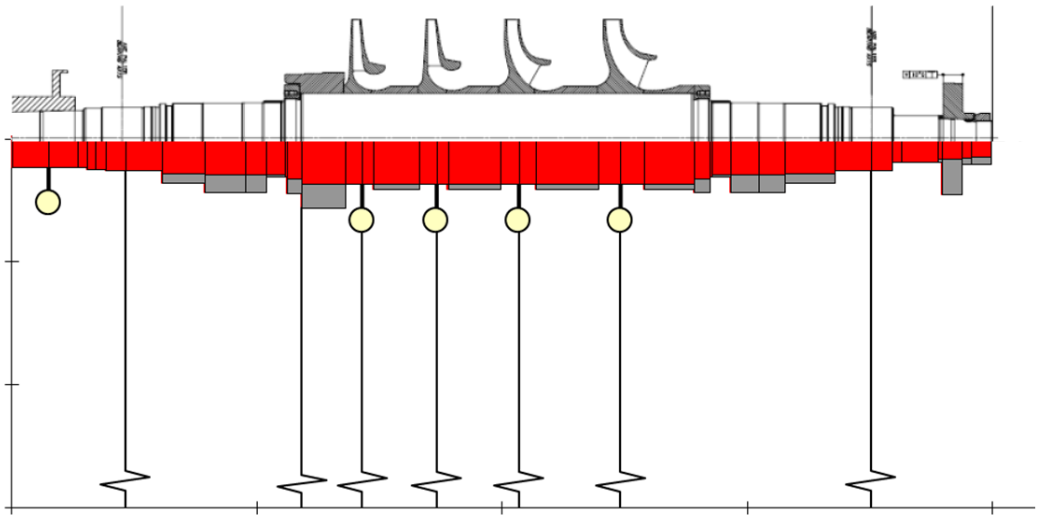

Figure 5-12. Schematization of the rotor model of the multistage compressor.

Once the model was built, the aerodynamic force, calculated in each load case, was applied to the critical impeller center of gravity, i.e., the fourth impeller.

Thanks to the asynchronous response module of the software, the aerodynamic excitation was applied not synchronized with the running speed and the rotordynamic behavior was hence predicted. In details, the rotating force was constant in amplitude

(properly scaled by means of Eq. 4-5) and variable in frequency. In particular, the whole subsynchronous range was investigated with special attention to the range between 10% to 80% of 1xREV; this range was indicated by the database analysis as the most common range for rotating stall frequency.

The rotordynamic response of the system to the aerodynamic excitation due to rotating stall is reported in Figure 5-13. In particular, the maximum expected vibrations on the most critical bearing (the one closer to the stalling impeller) as a function of the stall force in terms of dimensionless χ coefficient and the frequency of the stall itself is shown.

Moreover, the minimum (MIN) and the maximum (MAX) stiffness values provided by the manufacturer were analyzed in order to highlight the range of the response.

The grey-shadowed zone highlights the range of acceptability in terms of subsynchronous vibration of the system according to API617 (7^{th} ed.) [56].

By examining Figure 5-13, it is possible to point out some important aspects:

- As expected, the vibration amplitudes are directly proportional to the force intensity in the analyzed range of frequencies.
- The journal bearings stiffness has a strong impact on the rotordynamic behavior of the machine. In particular:
    - The larger the clearance (coupled with a higher oil inlet temperature), the lower the stiffness; this implies that the maximum vibrations are magnified and the resonance region is extended in frequency
    - The first critical frequency of the system (the peak of each curve) is shifted towards lower frequencies, closer to the typical stall range (i.e., 0÷30% of 1xREV).

The analysis was then repeated, introducing the labyrinth seals in the model. The results are shown in Figure 5-14. As expected, if on one hand the effects on the low region frequency were negligible, on the other hand, in the frequency range near the natural frequency the presence of the laby seals significantly reduced the system damping with a consequent increasing of the predicted vibrations of the compressor.

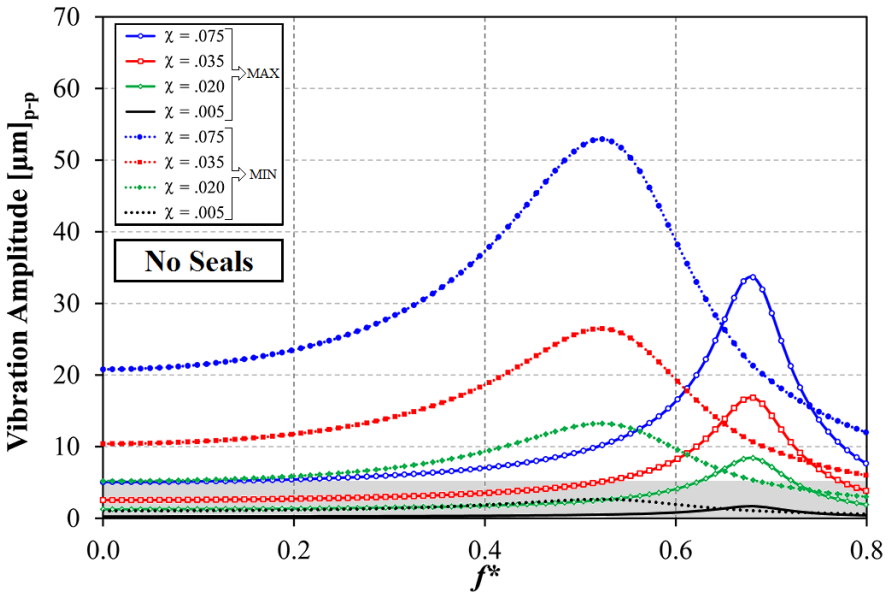

Figure 5-13. Predicted vibrations as a function of the stall force intensity and frequency.

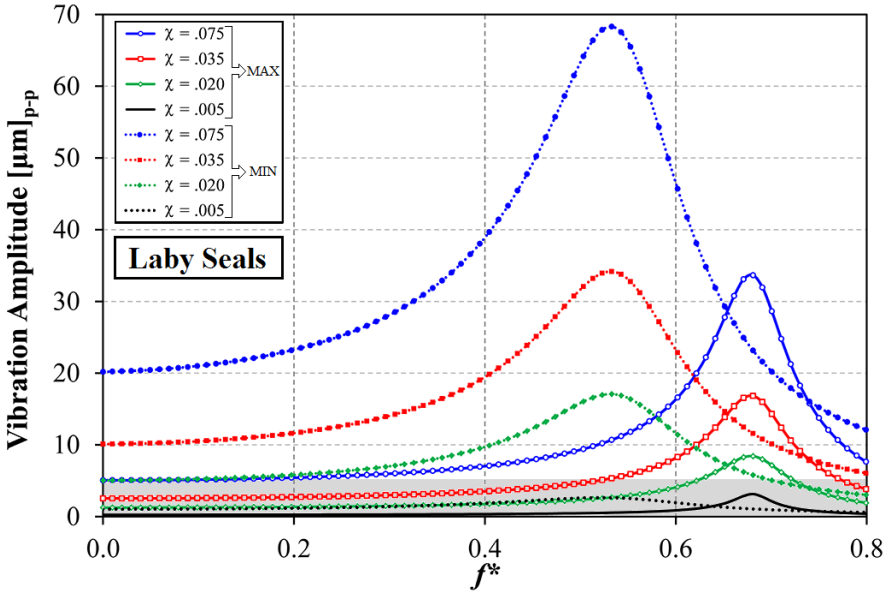

Figure 5-14. Predicted vibrations as a function of the stall force intensity and frequency with the laby seals effect.

A further analysis of these results can be done by combining the acceptable limit indicated by the standard with the presented response curves. By doing so, the

maximum tolerated force intensity can be found in the two bearing stiffness configurations for each value of the rotating stall frequency.

Figure 5-15 shows the results of this analysis.

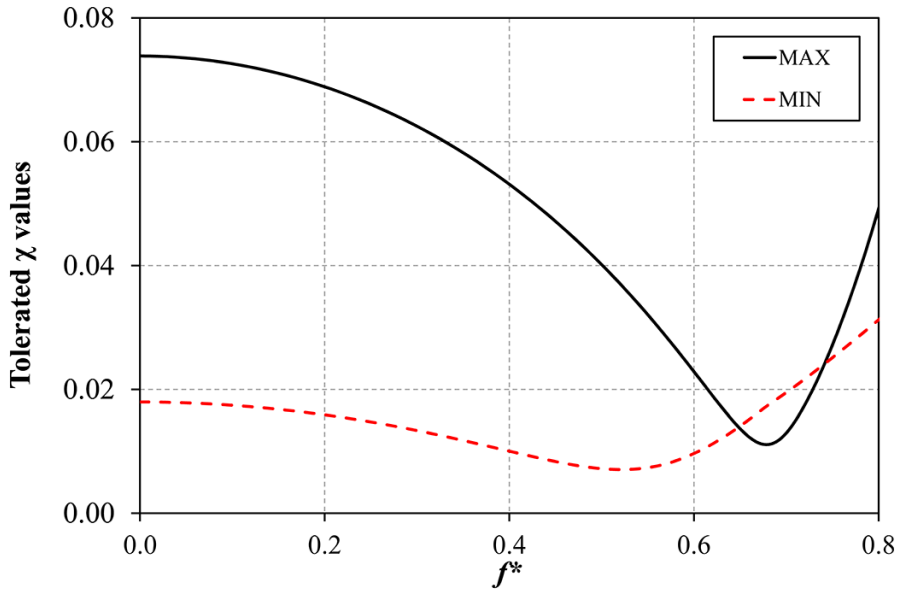

Figure 5-15. Maximum tolerated χ values as a function of the stall frequency.

Upon examination of the figure, one can readily notice that the impact of rotating stall force can be very different depending on the relative distance of the critical frequency of the system from the rotating stall frequency.

The information provided in Figure 5-15 represents the main outcome of this analysis. In particular, when the rotordynamic design of the compressor has been assessed, a specific map similar to that reported in Figure 5-15 could be realized. Then, the test-rig measurements on the most critical stage will provide an estimation of both the attended χ value for the stall force and its rotational frequency f^*.

Combining these two data, a point in the map is promptly definable and can be compared with the maximum tolerated solicitation on the system; in case the limits are not exceeded, a curve extension of the critical stage can be then taken into account. Otherwise, a review of the rotordynamic characteristics, especially in terms of bearings stiffness, might be carried out in order to mitigate the vibrations

connected to the stall. A scheme of the proposed approach developed in this study is reported in Figure 5-16.

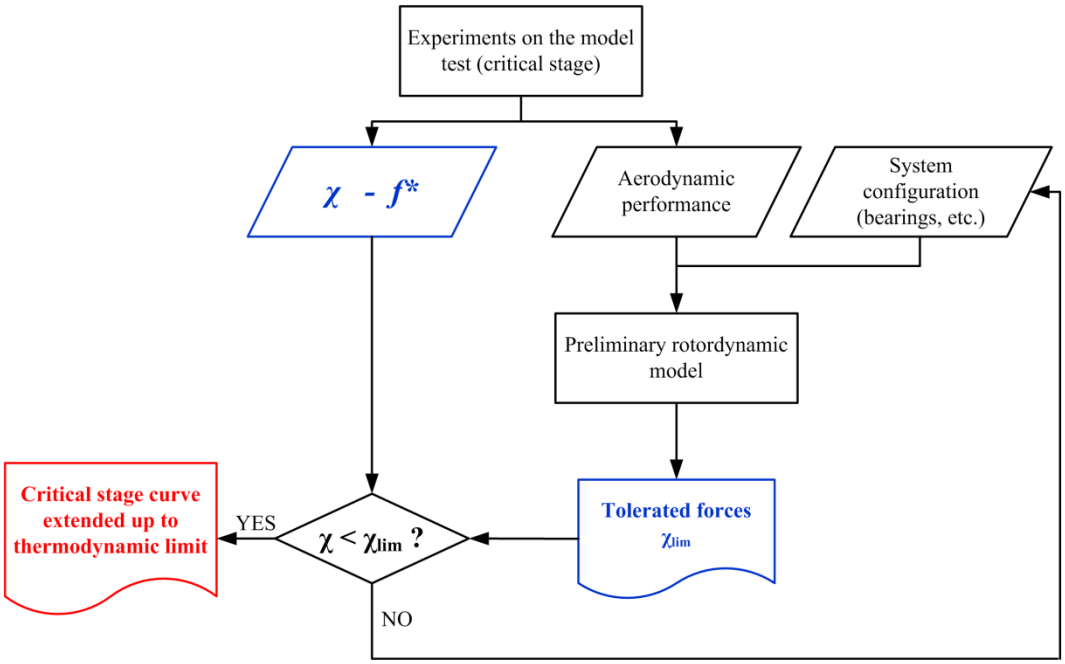

Figure 5-16. Flowchart of the rotordynamic approach.

As an example, the most critical stage of the compressor used in this analysis had a χ value of 0.021 and a dimensionless stall frequency of 7% of 1xREV. According to these values, the expected force in on-site conditions was estimated in the order of 290 N, producing a subsynchronous vibration on the bearing closer to the impeller equal to 1.5 μm peak-to-peak and 6.1 μm peak-to-peak at the maximum and minimum stiffness cases, respectively.

Based on these results, as the expected vibrations at minimum bearing stiffness are higher than the acceptable limit imposed by the standard, if an extension of the curve is hypothesized, the machine should be operated at the maximum bearing stiffness or a different bearings choice should be made.

Conclusions

The research activity presented in this work was focused on the development of a systematic approach to characterize the vaneless diffuser rotating stall in centrifugal compressors with the aim of predicting the behavior of the machine operating in these particular unsteady conditions.

Unlike the available approaches in literature that mainly show methodologies both to analyze the rotating stall and predict its onset, this study focused on the rotordynamic effects on the compressor due to the aerodynamic force generated by the pressure unbalancing during the stall.

The prediction of the actual operating conditions during stall by estimating the resulting aerodynamic force could represent a valuable contribution to identify an adequate control strategy in the design phase.

Within this scenario, three different phases were carried out in this study.

In the first part, after a review of the investigation methodologies, a systematic approach which analyzes the experimental data coming from dynamic pressure sensors properly installed in the diffuser was developed and assessed by using some case studies. In particular, all the tests were carried out in a dedicated single stage test-rig at *GE Oil & Gas – Nuovo Pignone*.

In details, the developed procedure allows one to reconstruct the pressure pattern in the diffuser and hence to evaluate the resulting force by means of an ensemble average process (clocked on the rotating stall frequency) coupled with the main hypothesis of rigid motion of the stall pattern; with this assumption a shift from the time domain into the spatial domain was possible.

On these bases, in the second part, the procedure was applied to the industrial database for a total amount of more than 60 model tests, mainly focusing on the characterization of the stall pattern and its resulting force in terms of frequency, intensity and number of lobes.

The analysis showed interesting results: the largest part of the impellers (87%) highlighted a stall frequency in the range of 5-20% of the 1xREV, while frequencies up to a maximum of about 80% were noticed only for few high flow coefficient tests. Moreover, the single lobe pattern was detected in the 89% of the model tests analyzed. Two-lobes and three-lobes appeared only in the 9% and 2% of the total tests, respectively.

Thanks to this accurate analysis, some issues related to the characterization of vaneless diffuser rotating stall were analyzed with particular reference to an industrial context. By doing so, some guidelines for a correct experimental analysis of rotating stall were proposed.

Based on the developed approach, the optimal positioning and the limitations in using two sensors have been highlighted and discussed. In particular, it has been assessed that in the common industrial practice, if three (or more) sensors are available, a probes positioning between 0° and 60° would offer the best resolution for stall patterns up to three lobes which would allow to easily gather all the tested cases. Alternatively, whenever three (or more) sensors are available, the approach can be applied to different couples of sensors ensuring the correct stall reconstruction also in case of many lobes.

Then, in order to compare impellers with different geometric dimensions and design points, a dimensionless force coefficient was defined dividing the calculated force by the dynamic pressure and the geometrical characteristics at the exit of the impeller. This allowed one to evaluate a rotating stall force in case of multistage compressors operating in real functioning conditions, i.e., at higher pressure.

The third part of the study tried to connect the first two phases by extending the results of the systematic approach to the rotordynamic of the machine using the scaling criterion developed with the industrial database analysis.

In order to verify the correlation and the prediction capability of the approach, some case studies were first selected in the available model tests and then, the

calculated force was applied to the rotordynamic model of the system, whose vibrations were compared to those measured by proper sensors positioned near the journal bearings: very good agreement between the experiments and the predicted values was found in terms of the frequency and vibration amplitude.

Moving from these results, the rotordynamic approach was extended to two multistage compressors tested in a *GE Oil & Gas* dedicated test rig, which were composed by impellers belonging to the same family of those tested in the single stage rig, therefore having similar geometrical characteristics and aero-design conditions. The results showed that the vibrations produced by rotating stall are in notable agreement with those determined with the rotordynamic model. Moreover, the systematic procedure can be assumed to be of general validity.

The methodology represents the first attempt to transfer the aerodynamic stall force calculated by means of dynamic pressure measurements carried out at the test rig into a predicted vibration of the whole compressor operating in on-site conditions.

Then, once the approach has been verified, some prospects of the methodology were evaluated in order to show the actual potential in term of prediction capability.

In particular, the final part of the third phase focused on a procedure to verify if the minimum flow margins in case of rotating stall could be extended by making use of specific bearings for different operating conditions. This could represent a useful tool in the design phase of a machine and a first step towards a practical extension of the left margin of the performance curve.

Bibliography

[1] A. R. Howell, «Fluid dynamics of axial compressors,» *Proceedings of the Institution of Mechanical Engineers* , vol. 153, pp. 441-452, 1945.

[2] D. Japiske, Centrifugal Compressor Design And Performance, Concepts Eti Publishing, 1996.

[3] Kita, M., Iwamoto, S., Kiuchi, I. and Kawashita, R., «Prediction of Subsynchronous Rotor Vibration Amplitude Caused by Rotating Stall,» in *Proceedings of the 37th Turbomachinery Symposium*, Houston, Texas (USA), 2008.

[4] Evans, B.F. and Smalley, A.J., «Subsynchronous Vibrations in a High Pressure Centrifugal Compressor: a case History,» Southwest Research Institute, San Antonio, Texas, NASA Tech. Rep, 1984.

[5] Bently, R. and Goldman, P., «Vibrational Diagnostics of Rotating Stall in Centrifugal Compressors,» Bently Rotor Dynamics Research Corporation, Tech. Rep, 2000.

[6] Bently, R., Goldman, P. and Yuan, J., «Rotor Dynamics of Centrifugal Compressors in Rotating Stall,» Bently Rotor Dynamics Research Corporation, Tech. Rep, 2001.

[7] Frigne, P., Braembussche, R. V. D., «Comparative Study of Subsynchronous Rotating Flow Patterns in Centrifugal Compressors with

Vaneless Diffusers,» *Rotor Dynamic Instability Problems in High-Performance Turbomachinery,* n. NASA Conference Publication 2250, pp. 365-382, 1982.

[8] Abdelhamid, A., N., Colwill, W., H., Barrows, J., F., «Experimental investigation of unsteady phenomena in vaneless radial diffusers,» *Transaction of ASME,* vol. 101, pp. 52-59, January 1979.

[9] Abdelhamid, A. N. and Bertrand, J., «Distinction between two types of self-excited gas oscillations in vaneless radial diffusers,» *Canadian Aeronautics and Space Journal,* vol. 26, n. 2, pp. 105-117, February 1980.

[10] A. N. Abdelhamid, «Analisysis of rotating stall in vaneless diffusers of centrifugal compressors,» in *ASME Paper No 80-GT-184*, New Orleans, USA, 1980.

[11] W. Jansen, «Rotating stall in a radial vaneless diffuser,» *Transactions of the ASME Journal of Basic Engineering,* n. 64-FE-6, pp. 750-758, 1964.

[12] Senoo, Y., Kinoshita, Y., Ishida, M., «Asymmetric flow in vaneless difffusers for centrifugal blowers,» *Trans ASME Journ Fluids Eng,* 1977a.

[13] Senoo, Y., Kinoshita, Y., «Influence of inlet flow conditions and geometries of centrifugal vaneless diffuser on critical flow angle for riverse flow,» *Trans ASME Journ Fluids Eng,* 1977b.

[14] Senoo, Y., Kinoshita, Y., «Limits in rotating stall and stall in vaneless diffuser of centrifugal compressors,» *ASME Paper No. 78-GT-19*, 1978.

[15] Senoo, Y., Kinoshita, Y., «Rotating stall induced in vaneless diffusers of very low specific speed centrifugal blowers,» *Transaction of ASME,* vol. 107 April, pp. 514-521, 1985.

[16] Nishida, H., Kobayashi, H., Takagi, T., and Fukoshima, Y., «A study on the rotating stall of centrifugal compressors (1st Report, Effect of vaneless diffuser width on rotating stall),» *Transactions of the Japan Society of Mechanical Engineers (B Edition),* n. 54(499), p. 589–594, 1988.

[17] Nishida, H., Kobayashi, H., Fukoshima, Y., Kikaigakkai, N., «A study on the rotating stall of centrifugal compressors (3rd Report: Rotating stall

suppression method),» *Transaction Japan society of mechanical engineers (B Edition),* vol. 57(543), pp. 3794-3800, 1991.

[18] Kobayashi, H., Nishida H., Takagi, T., and Fukoshima, Y, «A study on the rotating stall of centrifugal compressors (2nd Report, Effect of vaneless diffuser inlet shape on rotating stall),» *Transactions of the Japan Society of Mechanical Engineers (B Edition),* n. 56(529), pp. 98-103, 1990.

[19] Senoo, Y., Hayami, H., Ueki, H., «Low solidity tandem cascade diffusers for wide flow range centrifugal blowers,» *ASME Paper No. 83-GT-3,* 1983.

[20] A. N. Abdelhamid, «Effects of vaneless diffuser geometry on flow instability in centrifugal compression systems,» *Canadian Aeronautics and Space Journal,* n. 29(3), pp. 259-288, 1983.

[21] Z. S. Spakovszky, «Backward Traveling Rotating Stall Waves in Centrifugal Compressors,» *Journal of Turbomachinery,* vol. Vol. 126, n. January, pp. 1-12, 2004.

[22] Spakovszky, Z. S., Roduner, C. H., «Spike and Modal Stall Inception in an Advanced Turbocharger Centrifugal Compressor,» *Journal of Turbomachinery,* vol. Vol. 131, n. July, pp. 1-9, 2009.

[23] Ferrara, G., Ferrari, L., Mengoni, C. P., De Lucia, M., and Baldassarre, L., «Experimental investigation and characterization of the rotating stall in a high pressure centrifugal compressor: Part I: Influence of diffuser geometry on stall inception,» in *Proc. of the ASME Turbo Expo*, Amsterdam, The Netherlands, 2002.

[24] Ferrara, G., Ferrari, L., Mengoni, C. P., De Lucia, M., and Baldassarre, L., «Experimental investigation and characterization of the rotating stall in a high pressure centrifugal compressor: Part II: Influence of diffuser geometry on stage performance,» in *Proc. of the ASME Turbo Expo*, Amsterdam, The Netherlands, 2002.

[25] Ferrara, G., Ferrari, L. and Baldassarre, L., «Rotating Stall in Centrifugal Compressor Vaneless Diffuser: Experimental Analysis of Geometrical Parameters Influence on Phenomenon Evolution,» *Journal of Rotating Machinery,* n. 10(6), pp. 433-442, 2004.

[26] Ferrara, G., Ferrari, L., Baldassarre, L.;, «Experimental characterization of vaneless diffuser rotating stall part V: influence of diffuser geometry on stall inception and performance (3rd impeller tested),» in *Proceedings of ASME Turbo Expo 2006*, Barcelona, Spain, May 8-11, 2006.

[27] Dazin, A., Coutier-Delgosha, O., Dupont, P., Coudert, S., Caignaert, G. and Bois, G., «Rotating instability in the vaneless diffuser of a radial flow pump,» *Journal of Thermal SCience*, vol. 17, n. 4, pp. 368-374, 2008.

[28] Dazin, A., Cavazzini, G., Pavesi, G., Dupont, P., Coudert, S., Ardizzon, G., Caignaert, G. and Bois, G. , «High-speed stereoscopic PIV study of rotating instabilities in a radial vaneless diffuser,» *Experiments in Fluids*, vol. 51, n. 1, pp. 83-89, 2011.

[29] Toni, L., Ballarini, V., Cioncolini, S., Gaetani, P., and Persico, G., «Unsteady Flow Field Measurements in an Industrial Centrifugal Compressor,» in *Proceedings of the 39th Turbomachinery Symposium*, Houston, Texas (USA), 2010.

[30] Frigne, P. and Van den Braembussche, R., «A Theoretical Model for Rotating Stall in the Vaneless Diffuser of a Centrifugal Compressor,» *Journal of Engineering for Gas Turbines and Power*, vol. 107(2), pp. 507-513, April 1985.

[31] Tsujimoto, Y., Yoshida, Y., Mori, Y., «Study of Vaneless Diffuser Rotating Stall Based on Two-Dimensional Inviscid Flow Analysis,» *Journal of Fluids Engineering*, vol. Vol. 118, n. March, pp. 123-127, 1996.

[32] Dou, H. S., Mizuki, S., «Analysis of the flow in vaneless diffusers with large width-to-radius ratio,» *Journal of Turbomachinery*, vol. 120, pp. 193-201, January 1998.

[33] Gao, C., Gu, C., Wang, T. and Yang, B., «Analysis of geometries' effects on rotating stall in vaneless diffuser with Wavelet Neural Networks,» *International Journal of Rotating Machinery*, pp. 1-10, 2007.

[34] Ljevar, S., de Lange, H. C., and van Steenhoven, A. A., «Rotating Stall Characteristics in a Wide Vaneless Diffuser,» in *ASME Turbo Expo 2005*, Reno-Tahoe, Nevada, USA, 2005.

[35] Ljevar, S., de Lange, H. C., van Steenhoven, A. A., Dupont, P., Caignaert, G. and Bois, G., «Core flow instability in wide vaneless diffusers for the purpose of rotating stall investigation,» in *The 13th International Conference on Fluid Flow Technologies*, Budapest, Hungary, September 6-9, 2006.

[36] Ljevar, S., de Lange, H.C., and van Steenhoven, A. A., «Comparison of Rotating Stall Characteristics Between the Viscid and Inviscid Two-Dimensional Model,» *WSEAS Transaction of Fluid Mechanics,* vol. 5(1), pp. 480-487, 2006.

[37] Ljevar, S., de Lange, H.C., and van Steenhoven, A. A., «Comparison of a two-dimensional viscid and inviscid model for rotating stall analysis,» in *Proceedings of the 4th WSEAS International Conference on Fluid Mechanics and Aerodynamics*, Crete, Greece, August 21-23, 2006.

[38] Ljevar, S., de Lange, H.C., and van Steenhoven, A. A., «Two-Dimensional Rotating Stall Analysis in a Wide Vaneless Diffuser,» *International Journal of Rotating Machinery*, vol. Volume 2006, pp. 1-11, 2006.

[39] Robinson, C., Casey, M., Hutchinson, B. and Steed, R., «Impeller-diffuser interaction in centrifugal compressors,» in *Proc. of the ASME Turbo Expo 2012*, Copenhagen, Denmark, 2012 June 11-15.

[40] Hillewaert, K. and Van den Braembussche, R.A., «Numerical simulation of impeller-volute interaction in centrifugal compressors,» *ASME Journal of Turbomachinery,* vol. 121, p. 603–608, 1999.

[41] Lucius, A. and Brenner, G., «3D time accurate CFD simulations of a centrifugal compressor,» *Parallel Computational Fluid Dynamics 2008 - Lecture Notes in Computational Science and Engineering,* n. 74, pp. 173-180, 2011.

[42] Sorokes, J. M., Vezier, C., Dollinger, M., Pacheco, J. E., «Using unsteady analysis to improve the steady state CFD assessment of minimum flow in a radial compressor stage,» in *Proceedings of ASME Turbo Expo 2013*, San Antonio, Texas, USA, 2013 June 3-7.

[43] Marshall, D.F., and Sorokes, J.M., «A review of aerodynamically induced

forces acting on centrifugal compressors, and resulting vibration characteristics of rotors,» in *Proc. of the 29th Turbomachinery Symposium*, Houston, Texas (USA), 2000.

[44] J. Colding-Jørgensen, «Effect of fluid forces on rotor stability of centrifugal compressors and pumps,» NASA, Lewis Res. Center Rotordyn, 1980.

[45] Smith, D.R. and Wachel, J.C., «Nonsynchronous Forced Vibration in Centrifugal Compressors,» *Turbomachinery International Magazine*, n. January/February, pp. 21-24, 1983.

[46] Kita, M., Iwamoto, S., Kiuchi, D. and Kawashita, R., «Prediction of subsynchronous rotor vibration amplitude caused by rotating stall,» in *Proceedings of the thirty-seventh turbomachinery symposium*, 2008.

[47] N. A. Cumpsty, Compressor Aerodynamics, New York, USA: Krieger Publishing, 1989.

[48] B. Porat, Digital processing of random signals: theory and methods, London (UK): Dover Publications, 2008.

[49] A. Drake, Fundamentals of Applied Probability Theory, New York (USA): McGraw-Hill, 1988.

[50] Perlman, B.S. and Auerbach, V.H., «Phase-Locking Technique for Estimating the Ensemble Average of Time Series Data,» *IEEE Transactions on Acoustics, Speech, and Signal Processing*, n. ASSP-25(4), pp. 295-299, 1977.

[51] J. Colding-Jørgensen, «Prevention of Rotordynamic Problems in High Pressure Centrifugal Compressors,» in *Proc. of the 1st International Conference on Turbomachinery, Rotating Equipment and Condition Monitoring Equipment*, Singapore, July 20-22, 1994.

[52] Ishimoto, L., Silva, R. T., Rangel, J. S., Jr., Miranda, M. A., Audehove, F. N., Marques, B. S., Baldassarre, L. and Paut, C., «Early detection of rotating stall phenomenon in centrifugal compressors by means of ASME PTC 10 type 2 test,» in *Proc. of the Forty-First Turbomachinery Symposium*,

Houston, Texas, USA, September 24-27, 2012.

[53] T. R. Consortium, «XLTRC2 Rotordynamics Software Suite,» Turbomachinery Laboratory, Texas A&M University, 2002.

[54] Yoshida, Y., Tsujimoto, Y., Yokoyama, D., Ohashi, H. and Kano, F., «Rotordynamic Fluid Force Moments on an Open-type Centrifugal Compressor Impeller in Precessing Motion,» *International Journal of Rotating Machinery*, n. 7(4), pp. 237-251.

[55] Gerbet, M., Vannini, G., Catanzaro, M., Alban, T., «Rotordynamic Evaluation of Full Scale Rotor On Tilting Pad Bearings With Integral Squeeze Film Dampers,» in *Proc. of the ASME Turbo Expo 2012*, Copenhagen, Denmark, June 11-15, 2012.

[56] 2. API, «Axial and Centrifugal Compressors and Expander-compressors for Petroleum, Chemical and Gas Service Industry,» API Standard 617, 7th Edition , 2002.

[57] Branagan, L. and Barret, L., «Annex 4 – Tilting pad Dynamic Coefficient Reduction with pivot flexibility,» UVA Report No. UVA/643092/MAE88/376..

[58] Thorat, M. and Childs, D.W., «Predicted rotordynamic behavior of a labyrinth seal as rotor surface velocity approaches Mach 1,» in *Proceedings of ASME Turbo Expo 2009*, Orlando, USA, June 8-12, 2009.

[59] Kleynhans, G. and Childs, D.W., «The acoustic influence of cell depth on the rotordynamic characteristics of smooth-rotor/honeycomb-stator annular gas seals,» *Journal of Engineering for Gas Turbine and Power*, vol. 119, pp. pp. 949-957, 1997.